

Coherent lensless imaging techniques using terahertz radiation

Inauguraldissertation
der Philosophisch-naturwissenschaftlichen Fakultät
der Universität Bern

vorgelegt von

Lorenzo Valzania

von

Cesena, ITALIEN

Leiter der Arbeit:

Prof. Dr. T. Feurer
Institut für Angewandte Physik
Universität Bern

Dr. E. Hack

Laboratory for Transport at Nanoscale Interfaces
Empa, Swiss Federal Laboratories for Materials Science and Technology

**Coherent lensless imaging techniques
using terahertz radiation**

Inauguraldissertation
der Philosophisch-naturwissenschaftlichen Fakultät
der Universität Bern

vorgelegt von

Lorenzo Valzania

von

Cesena, ITALIEN

Leiter der Arbeit:

Prof. Dr. T. Feurer
Institut für Angewandte Physik
Universität Bern

Dr. E. Hack

Laboratory for Transport at Nanoscale Interfaces
Empa, Swiss Federal Laboratories for Materials Science and Technology

Von der Philosophisch-naturwissenschaftlichen Fakultät angenommen.

Bern, 6. Juni 2019

Der Dekan
Prof. Dr. Z. Balogh

Original document saved on the web server of the University Library of Bern



This work is licensed under a Creative Commons Attribution-Non-Commercial-No derivative works 2.5 Switzerland license. To see the license go to <http://creativecommons.org/licenses/by-nc-nd/2.5/ch/> or write to Creative Commons, 171 Second Street, Suite 300, San Francisco, California 94105, USA.

Copyright Notice

This document is licensed under the Creative Commons Attribution-Non-Commercial-No derivative works 2.5 Switzerland. <http://creativecommons.org/licenses/by-nc-nd/2.5/ch/>

You are free:



to copy, distribute, display, and perform the work

Under the following conditions:



Attribution. You must give the original author credit.



Non-Commercial. You may not use this work for commercial purposes.



No derivative works. You may not alter, transform, or build upon this work.

For any reuse or distribution, you must make clear to others the license terms of this work.

Any of these conditions can be waived if you get permission from the copyright holder.

Nothing in this license impairs or restricts the author's moral rights according to Swiss law.

The detailed license agreement can be found at: <http://creativecommons.org/licenses/by-nc-nd/2.5/ch/legalcode.de>

This thesis was typeset with \LaTeX . It is based on the *Clean Thesis* style developed by Ricardo Langner.

Download the *Clean Thesis* style at <http://cleanthesis.der-ric.de/>.

” *As he faced the sun he cast no shadow*
— **Noel Gallagher**
Songwriter, singer and guitarist

Contents

1	Introduction	1
2	Coherent lensless imaging techniques	7
2.1	Principles of the scalar diffraction theory of electromagnetic waves	7
2.1.1	The scalar wave equation	7
2.1.2	The Helmholtz equation	8
2.1.3	The Rayleigh-Sommerfeld diffraction equation	9
2.2	The phase problem	12
2.3	Digital holography	13
2.3.1	Off-axis digital holography	14
2.4	Ptychography	16
2.4.1	The extended Ptychographic Iterative Engine (ePIE) algorithm	17
2.5	Single-Beam Multiple-Intensity Reconstruction (SBMIR) phase retrieval	20
2.6	Conclusions	21
3	Overview of THz radiation	23
3.1	THz radiation	23
3.2	THz imaging techniques	24
3.3	THz sources	24
3.3.1	The THz gas laser system	25
3.4	THz detectors	27
3.5	Conclusions and outlook	27
4	Comparison of thermal cameras for THz off-axis digital holography and real-time THz imaging	35
4.1	Cameras, THz laser source and setups	35
4.2	Methods	37
4.2.1	Beam profiling	38
4.2.2	Camera response	38
4.2.3	Interference fringe contrast	39
4.2.4	Real-time off-axis holography	39
4.3	Results and discussion	39
4.3.1	Beam profiling	39
4.3.2	Camera response	40

4.3.3	Interference fringe contrast	41
4.3.4	Real-time off-axis holography	42
4.4	Conclusions and final remarks	44
5	Synthetic aperture THz off-axis digital holography	47
5.1	Description of the problem	47
5.2	Methods	47
5.3	Experiments	49
5.4	Results and discussion	49
5.5	Conclusions and outlook	51
6	THz ptychography	55
6.1	Experiments	55
6.2	Results and discussion	55
6.3	Conclusions and outlook	59
7	Resolution limits of THz ptychography and THz off-axis digital holography	61
7.1	Simulations	61
7.2	Experiments	63
7.3	Conclusions and final remarks	66
8	Coherent reconstruction of an object hidden behind a THz-transparent material through THz off-axis digital holography	69
8.1	Description of the problem	69
8.2	Method	73
8.3	Experiment	75
8.4	Results	75
8.5	Discussion	78
8.6	Conclusions	78
9	Coherent reconstruction of a textile and a hidden object through a THz phase retrieval technique	81
9.1	Description of the problem	81
9.2	Methods	82
9.2.1	Separation of the transmission functions of the two objects from their relative translations	83
9.3	Experiments	84
9.4	Results	85
9.5	Discussion	87
9.6	Conclusions	90
10	Conclusions and outlook	91

Appendices	95
A Proof of the object update equation in the extended ptychographical iterative engine (ePIE)	97
B Definition of some detector figures of merit used in Chapter 4	101
C Definition of the stitching operator \mathcal{S} used in Chapters 5, 9	103
D Rotational transformation of the complex amplitude of a wavefront	105
E Optimum acquisition parameters and lateral resolution of the SBMIR technique in the THz range	109
Bibliography	119
Acknowledgments	121
Declaration of consent	123
Curriculum vitae & Research output	125

List of Figures

1.1	(a) Imaging the skin-textile interface (central hexagon) and involved tasks and quantities (adjacent hexagons of the honeycomb). (b) The four tasks tackled in this thesis, outlined with different colors, and the corresponding Chapters in which they are considered.	3
2.1	Geometry of the Rayleigh-Sommerfeld diffraction theory.	10
2.2	(a) Typical experimental setup of off-axis digital holography, where the inset shows the wavevector difference $\Delta\mathbf{k}$. Simulated results: (b) Off-axis hologram of a nine-spoked Siemens Star, where the inset highlights the interference fringes caused by the off-axis angle θ and (c) displays the modulus of its Fourier transform in logarithmic scale. (d) Retrieved amplitude and (e) phase of the object beam at the camera plane. (f) Amplitude and (g) phase of the object beam propagated back to a plane parallel to the camera and at the position of the object.	15
2.3	(a) Typical experimental setup of ptychography in transmission. Simulated results: (b) Amplitude and (c) phase of the reconstructed object after using the diffraction pattern highlighted in the top right panel. (d) [(f)] Amplitude and (e) [(g)] phase of the reconstructed object after the 1 st [100 th] iteration.	18
2.4	(a) Typical experimental setup of the SBMIR phase retrieval. (b) Simulated diffraction patterns at 4 distances from the object plane. (c) Amplitude and phase of the reconstructed object after using the diffraction patterns from (b) once (1 st iteration) and 10 times (10 th iteration).	21
3.1	The electromagnetic spectrum hosts the THz band between the infrared and the microwave regions.	23
3.2	Vibrational-rotational emission lines of the CO ₂ molecule and their power, obtained from the specification sheet of the THz gas laser system.	26
4.1	(a) General schematic of the experimental setup. (b) Experiment area for the beam profiling and camera response experiments. (b) Experiment area for the interference fringe contrast and real-time off-axis holography experiments. A: Teflon absorber plate; PD: single-pixel pyroelectric detector; M: Mirror; BS: 10/90 beam splitter; S: shutter;	

	Camn: Camera #n; L_1, L_2 : collimating lenses; BSC: surface reflecting beam splitter cube; θ : off-axis angle. Adapted from [Hack et al., 2016].	37
4.2	Beam profile measurements at $\lambda = 118.8 \mu\text{m}$ measured with the four cameras. (a) Cam1; (b) Cam2; (c) Cam3; (d) Cam4; (e) horizontal cross-section through black lines in (a)-(d) and nominal beam profile (black line). From [Hack et al., 2016].	40
4.3	Camera response across the detection area, as defined in Eq. (4.3), (a)-(d) at $\lambda = 118.8 \mu\text{m}$. (a) Cam1; (b) Cam2; (c) Cam3; (d) Cam4; (e) Cam1 at $\lambda = 96.5 \mu\text{m}$. From [Hack et al., 2016].	41
4.4	Two-beam fringe pattern interfering with the high-frequency diffraction patterns caused by the camera housing, measured at $\lambda = 118.8 \mu\text{m}$, for Cam2 (left) and Cam3 (right). From [Hack et al., 2016].	42
4.5	Central part ($5 \times 5 \text{ mm}^2$) of the two-beam fringe pattern recorded on Cam1 to Cam4 (left to right) at $\lambda = 118.8 \mu\text{m}$. From [Hack et al., 2016].	42
4.6	Fourier spectrum of the two-beam interference pattern recorded at $\lambda = 118.8 \mu\text{m}$ with (a) Cam1; (b) Cam2; (c) Cam3; (d) Cam4. Λ^{-1} denotes the carrier frequency. The spectra (a)-(c) are clipped in the f_y direction. Intensities are plotted on a logarithmic scale. Adapted from [Hack et al., 2016].	43
5.1	(a) Complications arising when reconstructing an object with a size comparable to that of the detector. The wavefront diffracted by the outermost regions of the object is shaded in yellow and is recorded at the top of the detector plane, while the wavefront diffracted from outside the reconstructed region is shaded in purple and is recorded at the bottom of the camera. (b) Schematic of the off-axis digital holography setup with synthetic aperture acquisition in reflection. The object coordinate system $(\hat{x}, \hat{y}, \hat{z})$ is rotated with respect to the camera coordinate system (x, y, z) . The average object-camera distance is indicated with d . The function $\mathbf{1}_j$ restricts the detection area to the region \mathbf{D}_j at each position of the camera.	48
5.2	Comparison between optical images (left-hand side) and THz off-axis digital holography reconstructions (right-hand side) of a fingertip replica. (a) Photograph of the object. (b) Phase from projection moiré profilometry and (c) reconstructed profile of the microscopic ripple structure after filtering the low spatial frequencies in (b). (d) Amplitude and (e) phase from THz off-axis digital holography, and (f) reconstructed ripple profile. The green rectangle in (d) bounds the area shown in Fig. 5.3 (b).	51
5.3	Comparison between the reconstructed amplitude of a region of the fingertip replica obtained from (a) one and (b) 42 partially overlap-	

	ping holograms. Profiles along the red and green line in (a) and (b), respectively, are shown in (c) with the corresponding colors.	52
6.1	Schematic experimental setup for transmission ptychography. Adapted from [Valzania et al., 2018b].	56
6.2	Ptychographic reconstruction of an amplitude object (label 1) and a phase object (label 2). (a) Simulated object transmission function, with three positions of the probe from the scan. Corresponding diffraction patterns obtained from the (b), (d), (f) simulated and (c), (e), (g) real object. (h) Amplitude and (j) phase of the simulated reconstructions. (i) Amplitude and (k) phase of the experimental reconstructions. Insets show the probe (top: amplitude, bottom: phase; left: simulation, right: experiment). All phase distributions share the same phase scale, shown in (a2). Adapted from [Valzania et al., 2018b].	57
7.1	Lateral resolution (normalized to the wavelength) calculated for a simulated amplitude object reconstructed with the “Forth-and-back propagation” (\circ), “FFT holography” (\bullet), and “Ptychography” (\times) methods as a function of the reconstruction distance normalized to the camera size. The intrinsic resolution function from Eq. (7.1) is plotted with a solid black line. The blue filled circle and the red cross indicate the experimental resolution reached by synthetic aperture THz off-axis digital holography and THz ptychography, respectively (section 7.2). The insets show the corresponding reconstructed amplitudes. Scale bar: 2 mm. From [Valzania et al., 2018a].	63
7.2	Schematic experimental setup of (a) synthetic aperture off-axis digital holography and (b) ptychography. Adapted from [Valzania et al., 2018a].	64
7.3	Reconstructed profile of a phase object consisting of 9 squares with increasing depths. Black symbols show the result of a reference measurement using projection moiré profilometry; blue [red] symbols indicate the depths retrieved by synthetic aperture THz off-axis digital holography [THz ptychography], while the corresponding reconstructed wrapped phase is shown in the inset (a) [(b)]. Wrapped phases share the same colorbar, shown at the bottom. The total length of each errorbar is twice the standard deviation of the retrieved depth within the corresponding square. From [Valzania et al., 2018a].	66
8.1	(a) Schematic of an off-axis digital holographic setup in reflection with two samples stacked behind each other. (b) Insight into the three-beam interference arising from diffraction from the object and reflection from the cover. See the main text for an explanation of the symbols. Adapted from [Valzania et al., 2017b].	70

8.2	Simulation results. Amplitude distribution of (a) the hidden object, (b) the reference beam, and (c) the beam $T(\mathbf{x})$. Their interference pattern $I_{ROT}(\mathbf{x})$ is shown in (d), along with the modulus of its Fourier Transform in (e). (f) Interference pattern $I_{OT}(\mathbf{x})$ and (g) modulus of its Fourier Transform. (h) Interference pattern $I_{RT}(\mathbf{x})$ and (i) modulus of its Fourier Transform. (j) Intensity distribution of the subtraction performed to retrieve the hidden object and (k) modulus of its Fourier Transform. All the spectra are displayed on a common logarithmic scale. Adapted from [Valzania et al., 2017b].	71
8.3	Simulation results. (a) Retrieved amplitude and (b) phase distributions of the hidden object at the camera plane. (c) Reconstructed amplitude and (d) phase distributions after back-propagation to the position of the object. Adapted from [Valzania et al., 2017b].	74
8.4	Top row, experimental interference patterns: (a) $I_{ROT}(\mathbf{x})$, (b) $I_{OT}(\mathbf{x})$, (c) $I_{RT}(\mathbf{x})$. Bottom row, corresponding simulated patterns: (d) $I_{ROT}(\mathbf{x})$, (e) $I_{OT}(\mathbf{x})$, (f) $I_{RT}(\mathbf{x})$. Adapted from [Valzania et al., 2017b].	76
8.5	Experimental reconstructions of the object. Amplitudes (a), (d), (g), wrapped phases (b), (e), (h), and profiles (c), (f). (a), (b), (c): the object was not hidden; (d), (e), (f): the object was hidden behind a Teflon plate and the signal separation was applied to eliminate the contribution from the plate; (g), (h): the object was hidden behind the Teflon plate, but a standard Fourier Transform method was applied. In the plots (c) and (f), black symbols represent experimental data along the cross-sections highlighted in (b) and (e), while red lines show a parabolic fit. (i): colorbar for the wrapped phase. Adapted from [Valzania et al., 2017b].	77
9.1	Setup and summary of the implemented reconstruction technique. A collimated laser beam impinges from the left on a hidden object (here a Siemens Star) and a cover object (here a schematic textile) at the distance u and with transmission functions $o(\mathbf{x})$ and $t(\mathbf{x})$, respectively. The intensity of the complex wavefield $\Psi_{jk}(\mathbf{x})$ is recorded with a camera at multiple distances v_k from the cover object. This stack of diffraction patterns allows reconstructing the complex wavefields exiting the cover object $\psi_j(\mathbf{x})$. By shifting the cover object by the amounts \mathbf{x}_j , the two transmission functions are retrieved. From [Valzania et al., 2019].	83
9.2	Experimental reconstructions of the textile and the hidden objects (amplitude object on the left-hand side, label 1; phase object on the right-hand side, label 2). (a) Schematic of the hidden object. Reconstructed hidden object [textile] (b) [(c)] using prior information of the shifts applied to the textile, (d) [(e)] after retrieving the shifts through cross-correlation, and (f) assuming unknown shifts. (g2) Image of the	

	textile taken with a microscope in reflection mode. The lower right panels show the colorbars used for amplitude, phase and complex-valued reconstructions. The reconstructions of the textile share the same colorbar, where the hue encodes ϕ_t and the brightness $\sqrt{ t }$. Scale bars: 1 mm. From [Valzania et al., 2019].	86
9.3	Lateral resolution of the hidden amplitude object reconstructed at multiple (u, v_1) distances (u : distance between the two objects; v_1 : textile-camera distance). The red star indicates the values used for the results on the left-hand side of Fig. 9.2 and in Fig. 9.4. From [Valzania et al., 2019].	87
9.4	Reconstructed hidden amplitude object using $N_{xy} = 22$ (left), 50 (middle), and 100 (right) exit waves selected at random positions. From [Valzania et al., 2019].	87
9.5	Experimental reconstructions of the object and the textile hidden behind it (amplitude object on the left-hand side, label 1; phase object on the right-hand side, label 2). (a) Schematic of the object. Reconstructed textile [object] (b) [(c)] using prior information of the shifts applied to the textile, and (d) assuming unknown shifts. The lower left panels show the colorbars used for amplitude, phase and complex-valued reconstructions. The reconstructions of the textile share the same colorbar, where the hue encodes ϕ_t and the brightness $\sqrt{ t }$. Scale bars: 1 mm. From [Valzania et al., 2019].	89
E.1	Lateral resolution ρ normalized to the wavelength λ of the SBMIR reconstructions simulated with $N_z = 5$ diffraction patterns at relative distances $\Delta z = 1.1\epsilon_0$ (blue) and $\Delta z = 3.4\epsilon_0$ (red), used in 200 iterations. The estimated normalized resolutions are plotted with markers, while the resolution limits $(2NA_{\max})^{-1}$ (in black) and $(2NA_{\min})^{-1}$ (in the color of the corresponding Δz) are plotted with lines. The light-blue square shows the resolution of the experimental reconstruction in Fig. 9.2(b1). Adapted from [Valzania et al., 2019].	110

List of Tables

1.1	Publications obtained from the results described in this thesis.	6
3.1	Period, wavelength, wavenumber and photon energy of THz radiation at a frequency of 1 THz. $c \approx 3.0 \times 10^8$ m/s is the speed of light in vacuum, and $h \approx 6.6 \times 10^{-34}$ J s is Planck's constant.	24
3.2	Specifications of the three THz emission lines used in the experiments reported in this thesis. The polarization is given with respect to that of the pump infrared beam.	26
3.3	Description of the most used THz imaging techniques. The list has been compiled based on [Guerboukha et al., 2018] and the references therein.	29
3.4	Description of the most known sources of THz radiation. The list has been compiled based on [Dhillon et al., 2017; Guerboukha et al., 2018] and the references therein.	31
3.5	Description of the most known detectors of THz radiation. "mod." in the 4 th column stands for "modulation" and refers to the modulation frequency at which the NEP was evaluated. The list has been compiled based on [Dhillon et al., 2017; Guerboukha et al., 2018] and the references therein. † Because an optical beam is recorded, a CCD camera was used in this case.	33
4.1	Specifications according to the data sheets of the THz detectors compared in this work. Figures in parentheses are calculated.	36
4.2	Results of SNR_{ref} for the cameras at a THz power of $P_{\text{ref}} = 10$ mW and an integration time of $\tau_{\text{ref}} = 25$ ms. Numbers in parentheses correspond to values obtained with an IR-filter in front of the camera.	40
4.3	Use of the cameras in real-time holography and limitation on the off-axis angle θ_{max}	42
6.1	Depth and reconstructed phase of the phase object measured with an optical microscope (2 nd and 3 rd columns respectively) and measured with THz ptychography (4 th column). The reconstructed phase of the simulated object is given in the 5 th column. Standard deviations are given in parentheses in units of the least significant digits.	59
7.1	Depth and reconstructed phase of the phase object measured with projection moiré profilometry (2 nd and 3 rd columns respectively) and	

phase reconstructed with THz off-axis digital holography (4th column) and THz ptychography (5th column). Standard deviations are given in parentheses in units of the least significant digits. 67

Description of the problem

During our everyday activities, our skin senses the environment through mechanical contact. The most common example is the enduring interaction between skin and textiles, be them clothing, bedsheets, wound casts, or wearable sensors, to name a few. When skin is pressed and rubbed against them, the friction at the contact area may lead to skin irritations. This issue becomes more relevant with increasing interfacial moisture content, typically present in the form of sweat [Pasumarty et al., 2011]. In a very serious scenario, paraplegic and bedridden patients are likely to develop skin ulcers, owing to their impaired mobility. Therefore a current issue in health care is to understand the interaction of skin with textiles, and consequently prevent the rise of skin injuries. In this context, real-time and *in vivo* images of the skin-textile interface would provide physicians with an easy-to-interpret feedback on the state of the skin.

Choice of the imaging probe

To this end, a suited imaging probe should meet a number of requirements. First, it should reconstruct the skin topography in a harmless way for the human body. Second, it must transmit through the textile, the effect of which must be properly understood, to retrieve the profile of the skin hidden behind it. When skin and textiles are pressed against each other, imaging their contact area is fundamental in order to assess the region on the skin which is most likely to become injured. Finally, the probe should interact strong enough with water, so to image the interfacial humidity distribution with sufficient contrast.

Terahertz (THz) radiation, namely the part of the electromagnetic spectrum with frequency in the range 0.1 – 10 THz, has recently emerged as a suitable probe for this task. THz waves harmlessly interact with the human body. Researches on the safety of THz radiation on biological tissues have discarded the concerns that THz radiation might alter cellular activity and kinetics [Clothier and Bourne, 2003] or damage the DNA, the only induced effects being thermal [Wilmink et al., 2010]. In addition, THz waves can penetrate non-conducting and optically opaque materials, like textiles, deeper than shorter wavelength radiations, like infrared radiation. At the same time, they maintain the major benefit of infrared radiation, in that they are absorbed by polar molecules like water, which therefore can act as an imaging contrast agent. The altered hydration level of injured skin cells indeed motivated the use of THz radiation for monitoring the deterioration stage of skin in diabetic

patients [Hernandez-Cardoso et al., 2017], imaging scars with better contrast than with visible light [Fan et al., 2017], and distinguishing skin cancer cells from their environment of healthy tissue [Joseph et al., 2014]. A more comprehensive state of the art of the biomedical applications of THz radiation has been reported in [Yang et al., 2016].

Choice of the imaging technique

While the strong absorption of THz radiation by water limits the imaging geometry to reflection mode in medical applications, freedom is left on the choice of the imaging technique.

At this stage it is crucial to realize that the microscopic ripple structure of human skin is on the same length scale of the THz wavelength, namely $300\ \mu\text{m}$. This sets the interaction of THz waves with skin in the diffraction regime. Single-point measurements, where the sample is scanned with focused THz pulses and the specularly reflected signal is recorded on a single-pixel detector [Sun et al., 2018; Sun et al., 2019; Wang et al., 2018], result in time-consuming processes. Furthermore, they only reach a spatial resolution around $500\ \mu\text{m}$, set by the minimum spot size to which THz pulses can be focused. In order to obtain diffraction-limited images, they would require the full diffraction pattern to be measured at each position of the focused beam, further increasing the measurement time. Full-field measurements, where the samples are illuminated with wide beams and their diffracted THz wavefronts are recorded with cameras, allow bypassing these complications.

Moreover, a suited imaging technique should reconstruct both the amplitude and the phase of the wavefronts diffracted by skin, the latter being especially important to assess refractive index variations, which may happen at injured sites. Finally, because friction involves movements in the imaged scene, real-time imaging of moving objects should also be allowed.

Based on these requirements, in this thesis we will resort to full-field, *coherent and lensless imaging techniques*. The adjective *lensless* means that we will obviate the need to form images in the classical way, i.e. using a lens, thus making the acquisition setup more compact, simple, flexible and better tailored to real-life applications. Images will be formed in a fully digital way, from the two-dimensional diffraction patterns produced by the object and digitally recorded with a camera. This implies that the phase of the wavefronts is not directly recorded (leading to the so-called *phase problem*), and must be indirectly retrieved either via interferometric or iterative techniques. There is a vast literature on coherent and lensless imaging techniques [Guizar-Sicairos, 2010; Rodenburg, 2008], especially contributed by the X-ray and electron imaging communities, who have been dealing with poor quality optics for several decades. This led to the development of two large families of imaging techniques, namely the *holographic* ones and those belonging to *phase*

retrieval, which will be both extensively described and implemented in the next Chapters.

The quantities and tasks involved in imaging skin-textile interfaces are graphically summarized in Fig. 1.1(a).

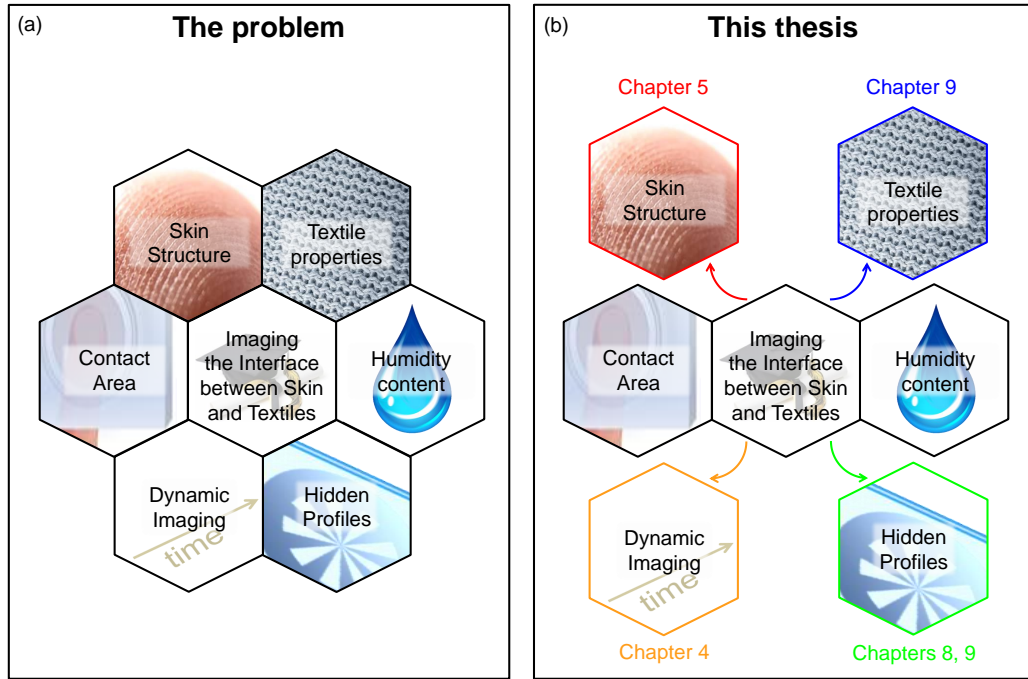


Fig. 1.1.: (a) Imaging the skin-textile interface (central hexagon) and involved tasks and quantities (adjacent hexagons of the honeycomb). (b) The four tasks tackled in this thesis, outlined with different colors, and the corresponding Chapters in which they are considered.

Thesis objective and outline

In this general perspective, the objective of this thesis is to develop and implement new coherent and lensless imaging techniques using THz radiation. The motivation behind them will be taken from their potential application to imaging skin samples hidden behind THz-transparent materials as well as textiles.

The work is organized as follows. **Chapter 2** provides the theoretical background behind coherent and lensless imaging techniques, including (i) the free-space propagation of monochromatic electromagnetic radiation within the scalar approximation and (ii) the phase problem. Three examples of reconstruction techniques solving the phase problem and relevant to the following results are introduced.

Chapter 3 gives a short overview of THz radiation, including the current trends of THz imaging techniques and the sources and detectors used to implement them.

Chapters 4-9 report my personal results. **Chapter 4** features a comparison among four thermal cameras capable of imaging THz radiation. The best camera for

our needs is chosen based on its performance in beam profiling, real-time imaging and resolving sub-mm interference fringe patterns as well as its response across the detector area.

Chapter 5 reports the application of THz digital holography for the reconstruction of a fingertip replica. In order to enhance the spatial resolution, a synthetic aperture approach is developed. The successful reconstruction of the microscopic ripple structure of the fingertip confirms that our holographic method is appropriate for imaging the structure of real human skin.

In **Chapter 6** we provide the first experimental demonstration of ptychography in the THz range. A follow-up study, included in **Chapter 7**, reports a comparison between THz off-axis digital holography and THz ptychography in terms of attainable lateral and depth resolution.

In **Chapter 8** an innovative imaging technique for imaging objects hidden behind THz-transparent materials is implemented. Here, we deal with the reconstruction of an amplitude object hidden behind a weakly diffracting Teflon plate in reflection mode.

In **Chapter 9** an original phase retrieval procedure, similar to ptychography, is developed and implemented, which simultaneously reconstructs a pair of objects stacked one behind the other, regardless of their diffracting behavior, in transmission mode. Its potential for real-world applications is demonstrated by reconstructing a fabric sample and a hidden amplitude or phase object, exploiting relative translations between them which naturally occur during friction.

Finally, **Chapter 10** discusses how the obtained results are crucial to the development of systems for imaging skin-textile interfaces.

Overall, four out of the six tasks shown in Fig. 1.1(a) will be tackled, namely [see Fig. 1.1(b)]: (i) imaging the structure of skin (Chapter 5); (ii) assessing the performance of our equipment for dynamic, real-time imaging (Chapter 4); (iii) reconstructing the profile of hidden objects (Chapters 8 and 9); and (iv) accounting for the optical distortions introduced by textiles (Chapter 9).

Table 1.1 lists the peer-reviewed articles and conference proceedings derived from the results reported in this thesis, along with the authors' contributions and the related Chapters in this work. In addition, the work was highlighted in several other presentations and publications. A complete list of my research output, including contributions outside the scope of this thesis, has been compiled in the section CV & Research output at the end of this manuscript.

Related Chapter	Publication title & reference	Authors	Journal & Issue	Authors' contributions
4	Comparison of thermal detector arrays for off-axis THz holography and real-time THz imaging [Hack et al., 2016]	E. Hack, L. Valzania , G. Gäumann, M. Shalaby, C. P. Hauri, and P. Zolliker	Sensors 16.2, p. 221 (2016)	E. H. devised the work and wrote the paper; L. V. realized the experimental setup, supported the data analysis and the preparation of figures ; G. G. was responsible for the use of the pyroelectric camera, and M. S. performed the measurements with the THz microbolometer, under the supervision of C. P. H.; P. Z. took part in the realization of the experimental setup, led the data analysis and prepared most figures. All authors contributed constructive comments during the preparation of the manuscript.
5	Towards the assessment of biomechanical interfaces: Topography of hidden objects obtained with THz holography [Valzania et al., 2017a]	L. Valzania , P. Zolliker, and E. Hack	Proc. of the 42nd Int. Conf. on Infrared, Millimeter, and Terahertz Waves, pp. 1-2 (2017)	L. V. devised the work, performed the experiments and the data analysis, and wrote the manuscript ; P. Z. was involved in the experiments and supervised the data analysis; E. H. supervised the work. All authors contributed constructive comments during the preparation of the manuscript.
6	Terahertz ptychography [Valzania et al., 2018b]	L. Valzania , T. Feurer, P. Zolliker, and E. Hack	Optics Letters 43.3, pp. 543-546 (2018)	L. V. performed the experiments and the data analysis, and wrote the manuscript ; T. F. devised the work and provided preliminary reconstruction codes; P. Z. supervised the work; E. H. supervised the work and was involved in part of the experiments. All authors contributed constructive comments during the preparation of the manuscript.

7	Resolution limits of terahertz ptychography [Valzania et al., 2018a]	L. Valzania , E. Hack, P. Zolliker, and T. Feurer	Proc. SPIE 10677, p. 1067720 (2018)	L. V. devised the work, performed the experiments and the data analysis, and wrote the manuscript; P. Z. and E. H. supervised the work; T. F. provided preliminary reconstruction codes. All authors contributed constructive comments during the preparation of the manuscript.
8	Topography of hidden objects using THz digital holography with multi-beam interferences [Valzania et al., 2017b]	L. Valzania , P. Zolliker, and E. Hack	Optics Express 25.10, pp. 11038-11047 (2017)	L. V. devised the work, performed the experiments and the data analysis, and wrote the manuscript; P. Z. and E. H. supervised the work. All authors contributed constructive comments during the preparation of the manuscript.
9, Appendix E	Coherent reconstruction of a textile and a hidden object with terahertz radiation [Valzania et al., 2019]	L. Valzania , P. Zolliker, and E. Hack	Optica 6.4, pp. 518-523 (2019)	L. V. devised the work, performed the experiments and the data analysis, and wrote the manuscript; P. Z. and E. H. supervised the work. All authors contributed constructive comments during the preparation of the manuscript.

Tab. 1.1.: Publications obtained from the results described in this thesis.

Coherent lensless imaging techniques

This Chapter introduces three techniques capable of reconstructing amplitude and phase of the wavefield *coherently diffracted* by an unknown object, when illuminated with coherent electromagnetic radiation. Instead of using a *lens* to image the object onto a recording device, these methods only rely on measuring the pattern scattered by the object after it propagated through free space by some distance. In order to understand their working principle, first we will review the fundamentals of the propagation of light when it interacts with objects not much bigger than the radiation wavelength: therefore we will summarize some of the most relevant results of the *diffraction* theory of electromagnetic radiation (section 2.1), following the approach used in [Goodman, 2005]. In section 2.2 we will see why recording a wavefield implies losing part of the information it carries. The following sections will then describe how this missing information can be retrieved, therefore allowing the reconstruction of the diffracted wavefield.

2.1 Principles of the scalar diffraction theory of electromagnetic waves

2.1.1 The scalar wave equation

Diffraction of electromagnetic waves in a medium is described by Maxwell's equations. In a region of space containing no free charges, they read:

$$\nabla \times \mathcal{E} = -\mu \frac{\partial \mathcal{H}}{\partial t} \quad (2.1a)$$

$$\nabla \times \mathcal{H} = \epsilon \frac{\partial \mathcal{E}}{\partial t} \quad (2.1b)$$

$$\nabla \cdot (\epsilon \mathcal{E}) = 0 \quad (2.1c)$$

$$\nabla \cdot (\mu \mathcal{H}) = 0, \quad (2.1d)$$

where $\mathcal{E} \equiv (\mathcal{E}_x; \mathcal{E}_y; \mathcal{E}_z)$ and $\mathcal{H} \equiv (\mathcal{H}_x; \mathcal{H}_y; \mathcal{H}_z)$ are the electric and magnetic field, respectively, expressed in cartesian coordinates and varying with position (x, y, z) and time t . The symbol $\nabla \equiv (\partial/\partial x; \partial/\partial y; \partial/\partial z)$, combined with the cross \times and dot \cdot products, computes the curl and the divergence, respectively. The electric permittivity ϵ and the magnetic permeability μ describe the linear response of the medium to the application of the electric and magnetic fields of the electromagnetic wave, respectively. For the scope of this thesis, we assume the medium to be: (i) non-dispersive, i.e., ϵ and μ do not depend on the frequency of the electromagnetic

wave; (ii) homogeneous, i.e., they do not depend on the position inside the medium; (iii) isotropic, i.e., they do not depend on the directions of \mathcal{E} and \mathcal{H} ; and (iv) non-magnetic, i.e., $\mu = \mu_0$, where $\mu_0 \approx 1.3 \times 10^{-6}$ N/A² is the vacuum permeability. As a result of these simplifications, ϵ and μ can be regarded as constants in Eqs. (2.1). Applying the $(\nabla \times)$ operator to both sides of Eq. (2.1a) and using Eqs. (2.1b), (2.1c) and the identity $\nabla \times (\nabla \times \mathcal{E}) \equiv \nabla(\nabla \cdot \mathcal{E}) - \nabla^2 \mathcal{E}$ yields the vector wave equation for the electric field:

$$\nabla^2 \mathcal{E} - \frac{n^2}{c^2} \frac{\partial^2 \mathcal{E}}{\partial t^2} = 0, \quad (2.2)$$

where the refractive index of the medium $n \equiv \sqrt{\epsilon/\epsilon_0}$ has been defined, $c = 1/\sqrt{\epsilon_0\mu_0}$ is the propagation speed in vacuum and $\epsilon_0 \approx 8.9 \times 10^{-12}$ F/m is the vacuum permittivity.

Owing to the analogy between Eqs. (2.1a) and (2.1b) and between Eqs. (2.1c) and (2.1d), Eq. (2.2) holds for \mathcal{H} , too. Furthermore, the linearity of all the operators in Eq. (2.2) allows us to write an independent scalar wave equation for each component of \mathcal{E} and \mathcal{H} . Denoting any of these components with $f(\mathbf{r}, t)$, with $\mathbf{r} \equiv (x, y, z)$, the scalar wave equation takes the form

$$\nabla^2 f(\mathbf{r}, t) - \frac{n^2}{c^2} \frac{\partial^2 f(\mathbf{r}, t)}{\partial t^2} = 0. \quad (2.3)$$

2.1.2 The Helmholtz equation

For all the methods treated throughout this work, \mathcal{E} and \mathcal{H} can be considered monochromatic, i.e., oscillating at one single frequency ν , such that $f(\mathbf{r}, t)$ can be expressed either as

$$f(\mathbf{r}, t) \equiv A(\mathbf{r}) \cos[2\pi\nu t - \phi(\mathbf{r})], \quad (2.4)$$

where $A(\mathbf{r})$ and $\phi(\mathbf{r})$ are the amplitude and the phase of the wave, respectively, or, equivalently, as

$$f(\mathbf{r}, t) \equiv \text{Re}[\psi(\mathbf{r}) \exp(-i2\pi\nu t)], \quad (2.5)$$

where $i \equiv \sqrt{-1}$ is the imaginary unit, Re computes the real part of a complex number, and the complex function $\psi(\mathbf{r}) \equiv A(\mathbf{r}) \exp[i\phi(\mathbf{r})]$ is often referred to as the *phasor* or *complex amplitude* of $f(\mathbf{r}, t)$. By writing Eq. (2.5), we managed to separate the spatial degrees of freedom of the solution from the temporal one, at the cost of introducing complex functions. After substituting Eq. (2.5) in Eq. (2.3), we find that the real and imaginary parts of $\psi(\mathbf{r})$, i.e. $\text{Re}[\psi(\mathbf{r})]$ and $\text{Im}[\psi(\mathbf{r})]$, respectively, must satisfy

$$\nabla^2 \text{Re}[\psi(\mathbf{r})] + k^2 \text{Re}[\psi(\mathbf{r})] = 0 \quad (2.6a)$$

$$\nabla^2 \text{Im}[\psi(\mathbf{r})] + k^2 \text{Im}[\psi(\mathbf{r})] = 0, \quad (2.6b)$$

where $k \equiv 2\pi\nu n/c \equiv 2\pi/\lambda$ is the wave number and $\lambda \equiv c/(n\nu)$ is the wavelength, namely the distance traveled by the wave within the period ν^{-1} . Equations (2.6) are termed Helmholtz equations, or time-independent wave equations. When combined together, they yield the Helmholtz equation for the complex amplitude $\psi(\mathbf{r})$:

$$\nabla^2 \psi(\mathbf{r}) + k^2 \psi(\mathbf{r}) = 0. \quad (2.7)$$

2.1.3 The Rayleigh-Sommerfeld diffraction equation

The propagation of a monochromatic electromagnetic wave through a homogeneous, isotropic, linear and non-magnetic medium within the scalar approximation is described by a number of theories, pioneered by Gustav Kirchhoff, who set a mathematical framework around Huygens and Fresnel's assumptions that a light wavefront can be regarded as a superposition of spherical waves emitted by point sources lying on a previous wavefront. Although Kirchhoff's theory agrees fairly well with experimental results, it presents a few theoretical inconsistencies, which were solved by Arnold Sommerfeld with the Rayleigh-Sommerfeld formulation of diffraction. Here, we will outline the Rayleigh-Sommerfeld theory, which our following work heavily relies on.

Let us consider a wavefield impinging on a planar screen \mathbf{S} , which is opaque except for an aperture \mathbf{A} (Fig. 2.1), and let the wavefield diverge to the half-plane behind the screen. Let also $\psi(\mathbf{x})$, $\mathbf{x} \in \mathbf{S}$ and $\psi(\mathbf{r})$ represent the complex amplitude of the wavefield on the screen and at the position \mathbf{r} at the distance d from the screen, respectively. We wish to express the wavefield at any position behind the screen, assuming that it is known on the screen. We make use of the following theorem, named after George Green:

Theorem 2.1: Green

If a complex function $\psi(\mathbf{r})$ is continuous and its first and second partial derivatives are single-valued and continuous within a volume \mathbf{V} surrounded by a closed surface Σ , then

$$\iiint_{\mathbf{V}} [\psi(\mathbf{r}) \nabla^2 G(\mathbf{r}) - G(\mathbf{r}) \nabla^2 \psi(\mathbf{r})] d\mathbf{r} = \oiint_{\Sigma} \left[\psi(\mathbf{x}) \frac{\partial G(\mathbf{x})}{\partial \mathbf{n}} - G(\mathbf{x}) \frac{\partial \psi(\mathbf{x})}{\partial \mathbf{n}} \right] d\mathbf{x}, \quad (2.8)$$

where $G(\mathbf{r})$ is known as Green's function and is any other function with the same requirements as $\psi(\mathbf{r})$, and \mathbf{n} is the outward normal unit vector at each point on Σ .

Specifically to our case, $\psi(\mathbf{r})$ is the unknown wavefield, while the Green's function $G(\mathbf{r})$, the surface Σ and the volume \mathbf{V} of integration must be cleverly

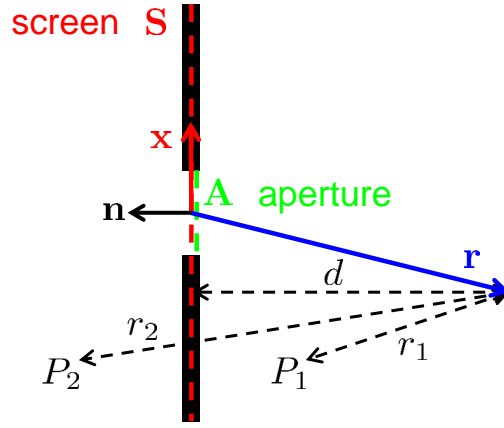


Fig. 2.1.: Geometry of the Rayleigh-Sommerfeld diffraction theory.

chosen in order to simplify the calculations. We begin by choosing a Green's function satisfying the Helmholtz equation along with $\psi(\mathbf{r})$, i.e.

$$\nabla^2 \psi(\mathbf{r}) + k^2 \psi(\mathbf{r}) = 0 \quad (2.9a)$$

$$\nabla^2 G(\mathbf{r}) + k^2 G(\mathbf{r}) = 0. \quad (2.9b)$$

Then, we note that the integrand on the left-hand side of Eq. (2.8) vanishes, thus reducing Green's theorem to the evaluation of $\psi(\mathbf{r})$ and $G(\mathbf{r})$ and their first derivatives along the closed surface Σ . Sommerfeld opted for the following Green's function:

$$G_{\text{Sommm}}(\mathbf{r}) = \frac{\exp(i k r_1)}{r_1} - \frac{\exp(i k r_2)}{r_2}, \quad (2.10)$$

where r_1 and r_2 are the distances of the point \mathbf{r} from two points, respectively P_1 and P_2 , which are the mirror image of each other on the two opposite sides of the screen (see Fig. 2.1 again). Such a choice of $G_{\text{Sommm}}(\mathbf{r})$, along with the assumption that $\psi(\mathbf{x})$ diverges from the aperture [$\psi(\mathbf{r})$ is said to satisfy the Sommerfeld radiation condition], significantly simplifies the right-hand side of Eq. (2.8):

$$\psi(\mathbf{r}) = -\frac{1}{4\pi} \iint_{\mathbf{S}} \psi(\mathbf{x}) \frac{\partial G_{\text{Sommm}}(\mathbf{x})}{\partial \mathbf{n}} d\mathbf{x}. \quad (2.11)$$

Note that this result, known as the integral theorem of Helmholtz and Kirchhoff, allows us to compute $\psi(\mathbf{r})$ from its value on the screen \mathbf{S} only. It is often common to apply the so-called Kirchhoff boundary condition on $\psi(\mathbf{r})$, imposing that both $\psi(\mathbf{r})$ and $\partial\psi(\mathbf{r})/\partial\mathbf{n}$ vanish on $\mathbf{S} \setminus \mathbf{A}$, i.e., on the geometrical shadow of the screen. After substituting Eq. (2.10) in Eq. (2.11) under the Kirchhoff boundary condition on $\psi(\mathbf{r})$, we obtain the Rayleigh-Sommerfeld solution:

$$\psi(\mathbf{r}) = -\frac{1}{2\pi} \iint_{\mathbf{A}} d\psi(\mathbf{x}) (ik - r_0^{-1}) \frac{\exp(ikr_0)}{r_0^2} d\mathbf{x}, \quad (2.12)$$

where $r_0 \equiv |\mathbf{r} - \mathbf{x}|$. Note that the solution at a certain position \mathbf{r} is a linear superposition of infinitesimal contributions, depending only on the relative distance r_0 from each point on the aperture. Therefore the system is linear and space-invariant (or, equivalently, isoplanatic) and Eq. (2.12) can also be written as,

$$\psi(\mathbf{x}, d) = \psi(\mathbf{x}, 0) * h'(\mathbf{x}, d) \quad (2.13a)$$

$$h'(\mathbf{x}, d) \equiv \frac{d}{2\pi} (r^{-1} - ik) \frac{\exp(ikr)}{r^2}, \quad (2.13b)$$

where $*$ denotes the convolution operator and $r \equiv \sqrt{|\mathbf{x}|^2 + d^2}$. If we assume that all the points of interest lie much farther from the screen than the wavelength, i.e. $d^{-1} \ll k$, then $r^{-1} \ll k$ and Eq. (2.13b) can be further simplified, yielding $h'(\mathbf{x}, d) \approx h_d(\mathbf{x})$, with:

$$h_d(\mathbf{x}) \equiv \frac{d}{i\lambda} \frac{\exp(ik\sqrt{|\mathbf{x}|^2 + d^2})}{|\mathbf{x}|^2 + d^2}. \quad (2.14)$$

Equation (2.14) finally represents the convolution kernel associated with the *forward* propagation of an electromagnetic wave of wavelength λ from a planar screen to distances much larger than λ , obtained under the scalar approximation, the Sommerfeld radiation condition and the Kirchhoff boundary conditions. The convolution kernel corresponding to the *backward* propagation, $h_{-d}(\mathbf{x})$, is obtained by applying the convolution theorem to Eq. (2.13a), under the approximation $h'(\mathbf{x}, d) \approx h_d(\mathbf{x})$. Denoting the Fourier transform of $h_d(\mathbf{x})$ with $\mathcal{H}_d(\mathbf{f})$, namely $\mathcal{H}_d(\mathbf{f}) \equiv \mathcal{F}\{h_d(\mathbf{x})\}$, this yields

$$h_{-d}(\mathbf{x}) \equiv \mathcal{F}^{-1}\{\mathcal{H}_d^{-1}(\mathbf{f})\}. \quad (2.15)$$

It can be shown [Goodman, 2005] that, within our approximations, $\mathcal{H}_d^{-1}(\mathbf{f}) \approx \mathcal{H}_d^*(\mathbf{f})$, where the superscript $*$ indicates complex conjugation. The result is known as *time reversal property*: conjugation in the frequency domain corresponds to time reversal in time domain, thus allowing the propagation of a wavefront backwards in time. We will make heavy use of Eqs. (2.14) and (2.15) in the next Chapters, in situations where the assumptions made to derive it always hold true. In particular, propagations between parallel planes will be mostly considered. In this case, the longitudinal distance d is constant and can be regarded as a parameter. For this reason, d is used as a subscript in Eqs. (2.14) and (2.15).

As a last word on the validity of Eqs. (2.14) and (2.15), we would like to specify that we will use them to reconstruct objects which are neither homogeneous, nor isotropic. Nevertheless, this does not make our assumptions in section 2.1.1 inappropriate. Propagations and back-propagations will not be performed through the objects, rather through the medium (air or, almost equivalently, vacuum) surrounding them, which satisfies the assumptions listed in section 2.1.1.

2.2 The phase problem

In imaging experiments, electromagnetic waves are typically measured with digital cameras. As will be seen in the next Chapters, bolometers are the cameras of choice for THz imaging. These convert the absorbed THz radiation into heat, increasing the temperature of their active material, whose electrical resistance varies with temperature changes. Therefore, the energy delivered by THz waves to the active material is the relevant quantity to the measurement process.

The amount of energy crossing a unit area per unit time, along a direction perpendicular to both \mathcal{E} and \mathcal{H} , is the modulus of the Poynting vector [Griffiths, 1962]:

$$\mathcal{S}(\mathbf{r}, t) \equiv \mathcal{E}(\mathbf{r}, t) \times \mathcal{H}(\mathbf{r}, t). \quad (2.16)$$

Because digital cameras are too slow to follow the oscillations of optical electromagnetic fields, the measured quantity in our experiments will be proportional to the modulus of the time-averaged Poynting vector. We define such quantity the *intensity* of the electromagnetic field, and we denote it with the symbol $I(\mathbf{r})$:

$$I(\mathbf{r}) \equiv |\langle \mathcal{S}(\mathbf{r}, t) \rangle_t| \equiv \left| \frac{1}{T_{\text{int}}} \int_0^{T_{\text{int}}} \mathcal{S}(\mathbf{r}, t) dt \right|, \quad (2.17)$$

where T_{int} is the camera integration time, which is always much larger than the period of the electromagnetic fields considered in this work, i.e., $T_{\text{int}} \gg \nu^{-1}$.[†] As previously done when deriving the Helmholtz equation (section 2.1.2), dealing with monochromatic waves allows us to use the complex amplitude representation of the electric and magnetic fields, that is,

$$\mathcal{E}(\mathbf{r}, t) \equiv \text{Re}[\mathbf{E}(\mathbf{r}) \exp(-i2\pi\nu t)] = \frac{1}{2}[\mathbf{E}(\mathbf{r}) \exp(-i2\pi\nu t) + \mathbf{E}^*(\mathbf{r}) \exp(i2\pi\nu t)], \quad (2.18a)$$

$$\mathcal{H}(\mathbf{r}, t) \equiv \text{Re}[\mathbf{H}(\mathbf{r}) \exp(-i2\pi\nu t)] = \frac{1}{2}[\mathbf{H}(\mathbf{r}) \exp(-i2\pi\nu t) + \mathbf{H}^*(\mathbf{r}) \exp(i2\pi\nu t)], \quad (2.18b)$$

where $\mathbf{E}(\mathbf{r})$ and $\mathbf{H}(\mathbf{r})$ are the complex amplitudes of $\mathcal{E}(\mathbf{r}, t)$ and $\mathcal{H}(\mathbf{r}, t)$, respectively. Combining Eqs. (2.16), (2.17) and (2.18) yields:

$$I(\mathbf{r}) = \left| \frac{1}{2} \text{Re}[\mathbf{E}(\mathbf{r}) \times \mathbf{H}^*(\mathbf{r})] + \frac{1}{2T_{\text{int}}} \int_0^{T_{\text{int}}} \text{Re}[\mathbf{E}(\mathbf{r}) \times \mathbf{H}(\mathbf{r}) \exp(-i4\pi\nu t)] dt \right|. \quad (2.19)$$

[†]Nowadays, high-speed cameras for THz radiation have approached the kHz frame rate (see, for example, the TeraFAST-256 camera by Terasense Group Inc., achieving a maximum frame rate of 5 kHz [Terasense imaging products]), which is 9 orders of magnitude lower than the oscillation frequency of the THz electromagnetic fields used in this work.

The second term on the right-hand side of Eq. (2.19) oscillates at frequency $2\nu \gg T_{\text{int}}^{-1}$, therefore it can be neglected when compared to the first term. In conclusion, the intensity can be expressed by the following approximation:

$$I(\mathbf{r}) \approx \frac{1}{2} |\text{Re}[\mathbf{E}(\mathbf{r}) \times \mathbf{H}^*(\mathbf{r})]| . \quad (2.20)$$

In other words, cameras are sensitive to the modulus of a quantity proportional to the product of orthogonal electric and magnetic field components. For example, in the specific case of a plane wave, one has $\mathbf{E}(\mathbf{r}) = \mathbf{E}_0$, $\mathbf{H}(\mathbf{r}) = \mathbf{H}_0 = \sqrt{\epsilon/\mu} \mathbf{E}_0$ and $I(\mathbf{r}) \propto |\mathbf{E}_0|^2$. In analogy to this case, throughout this whole work we are going to express the measurable quantity from a camera as the square modulus of a complex scalar function, associated with the electric and magnetic fields of the incident wave. Note, that the phase of such function is lost during the measurement. This loss is known as *phase problem*, and several approaches have been conceived in order to retrieve the missing information. Three of them, which are relevant to this thesis, will be outlined in the next sections.

2.3 Digital holography

The term *holography* comes from the Greek words *holo*, meaning “whole”, and *graphein*, meaning “to write”, which refer to its capability of retrieving the entire information of a wavefront, namely its amplitude and phase. Holography solves the phase problem by superimposing a coherent wave (the *reference beam*) to the wavefield diffracted from the unknown object (the *object beam*). The missing phase is encoded in their interference pattern, called *hologram*, from which it can be extracted through optical or digital processes. The holographic principle was suggested in 1948 by Dennis Gabor, an invention that earned him the Nobel prize in Physics in 1971. In the late 1940s, he was aiming at improving image formation in electron microscopy, strongly affected by the aberrations introduced by the electron optics of that time. Instead of forming an image of the object with lenses, he proposed to record the diffraction pattern of the object, superimposed with the reference wave, onto a photographic plate, and subsequently reproduce the imaging process optically, by illuminating the record with the same reference wave [Gabor, 1948]. The poor coherence of the radiation sources available at that time delayed the scientific impact of his idea, until the discovery of the laser in 1960. Furthermore, the knowledge of the principles of diffraction and interference of waves, combined with the increased performance of computers and development of opto-electronic devices witnessed during the last 80 years, made it possible to carry out the imaging procedure numerically, after recording the holograms with CCD or CMOS cameras. Such achievements established *digital holography* as a reference technique for strain, deformation and shape measurements, imaging fluid flows and cells, and full-field vibration measurements. Extensive reviews on the topic, including applications

going beyond the scope of this thesis, can be found in [Schnars and Jueptner, 2005; Kreis, 2006; Picart, 2015; Ferraro et al., 2011; Rastogi and Hack, 2012].

2.3.1 Off-axis digital holography

The setup of off-axis digital holography is sketched in Fig. 2.2(a). The coherent radiation emitted by a laser is split by a beam splitter in two beams, namely the reference beam,

$$R(\mathbf{x}) \equiv A_R(\mathbf{x}) \exp\{i[\mathbf{k}_R \cdot \mathbf{x} + \phi_R(\mathbf{x})]\}, \quad (2.21)$$

traveling undisturbed to the camera along the direction set by its average wavevector \mathbf{k}_R , and the object beam

$$O(\mathbf{x}) \equiv A_O(\mathbf{x}) \exp\{i[\mathbf{k}_O \cdot \mathbf{x} + \phi_O(\mathbf{x})]\}, \quad (2.22)$$

interacting with the object and traveling along the direction set by its average wavevector \mathbf{k}_O , which makes an angle θ with \mathbf{k}_R [see the inset of Fig. 2.2(a)]. For this reason, the configuration is referred to as *off-axis* digital holography. We have indicated with $\mathbf{x} \equiv (x, y)$ the coordinates on the camera plane; $A_U(\mathbf{x})$, $U \in \{R, O\}$, are the real amplitudes of the beams, and $\phi_U(\mathbf{x})$ are their phases, when observed on a plane perpendicular to their average wavevector.

The camera records the intensity of the interference pattern $\Psi(\mathbf{x}) \equiv R(\mathbf{x}) + O(\mathbf{x})$ obtained from the superposition of the object beam and the reference beam, known as *hologram*, reading:

$$\begin{aligned} I(\mathbf{x}) &\equiv |\Psi(\mathbf{x})|^2 \equiv |R(\mathbf{x}) + O(\mathbf{x})|^2 \\ &= A_R^2(\mathbf{x}) + A_O^2(\mathbf{x}) + 2 A_R(\mathbf{x}) A_O(\mathbf{x}) \cos\{\mathbf{k}_R \cdot \mathbf{x} + [\phi_R(\mathbf{x}) - \phi_O(\mathbf{x})]\}. \end{aligned} \quad (2.23)$$

Figure 2.2(b) shows the simulated hologram of a nine-spoked Siemens Star. As can be seen in the zoomed part of Fig. 2.2(b), it features a periodic pattern of bright and dark fringes, in the regions of constructive and destructive interference, respectively. The fringe spacing depends on the wavevector difference $\Delta\mathbf{k} \equiv \mathbf{k}_R - \mathbf{k}_O$ [see again the inset of Fig. 2.2(a)]. If we consider the setup shown in Fig. 2.2(a), the object beam impinges normally with the plane of the camera, which therefore makes an angle $\theta/2$ with $\Delta\mathbf{k}$. The fringe pattern is thus observed along x , with a period Λ given by

$$\Lambda = \frac{2\pi}{|\Delta\mathbf{k}| \cos(\theta/2)} = \frac{\pi}{(2\pi/\lambda) \sin(\theta/2) \cos(\theta/2)} = \frac{\lambda}{\sin(\theta)}. \quad (2.24)$$

Such fringes are essential in order to extract the phase of the object beam from the hologram of Eq. (2.23). The most common method to retrieve it is known as Fourier Transform method.

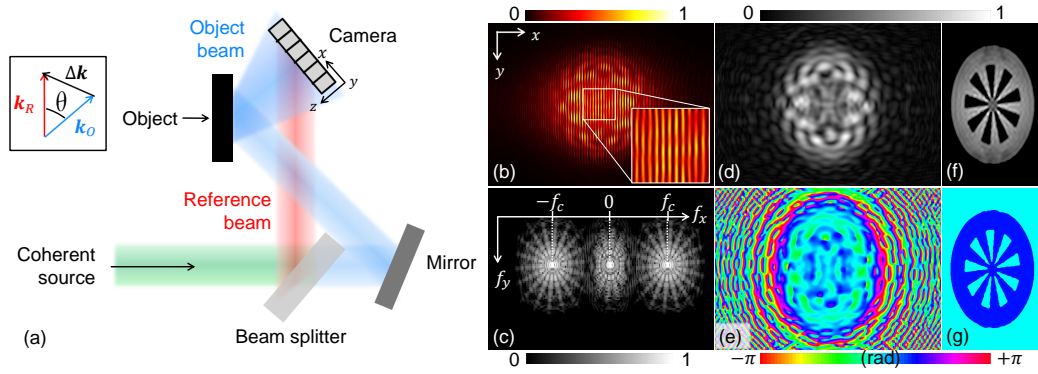


Fig. 2.2.: (a) Typical experimental setup of off-axis digital holography, where the inset shows the wavevector difference $\Delta\mathbf{k}$. Simulated results: (b) Off-axis hologram of a nine-spoked Siemens Star, where the inset highlights the interference fringes caused by the off-axis angle θ and (c) displays the modulus of its Fourier transform in logarithmic scale. (d) Retrieved amplitude and (e) phase of the object beam at the camera plane. (f) Amplitude and (g) phase of the object beam propagated back to a plane parallel to the camera and at the position of the object.

Fourier Transform Method

We can rewrite the hologram of Eq. (2.23) as follows,

$$I(\mathbf{x}) = a(\mathbf{x}) + b(\mathbf{x}) \cos[2\pi f_c x + \Delta\phi(\mathbf{x})], \quad (2.25)$$

which is obtained with the following substitutions:

$$a(\mathbf{x}) \equiv A_R^2(\mathbf{x}) + A_O^2(\mathbf{x}) \quad (2.26a)$$

$$b(\mathbf{x}) \equiv 2A_R(\mathbf{x})A_O(\mathbf{x}) \quad (2.26b)$$

$$2\pi f_c x \equiv (\mathbf{k}_R - \mathbf{k}_O) \cdot \mathbf{x} \quad (2.26c)$$

$$\Delta\phi(\mathbf{x}) \equiv \phi_R(\mathbf{x}) - \phi_O(\mathbf{x}) \quad (2.26d)$$

and where the sinusoidal fringe pattern is assumed to vary along x with the *carrier frequency* $f_c \equiv \Lambda^{-1}$. After expressing the cosine function as weighted sum of exponential functions, i.e., $\cos \alpha \equiv (\exp(i\alpha) + \exp(-i\alpha))/2$, Eq. (2.25) becomes:

$$I(\mathbf{x}) = a(\mathbf{x}) + c(\mathbf{x}) \exp(i2\pi f_c x) + c^*(\mathbf{x}) \exp(-i2\pi f_c x) \quad (2.27a)$$

$$c(\mathbf{x}) \equiv \frac{1}{2}b(\mathbf{x}) \exp[i\Delta\phi(\mathbf{x})]. \quad (2.27b)$$

Fourier transformation of the above intensity distribution yields the spectrum

$$\mathcal{I}(f_x, f_y) = \mathcal{A}(f_x, f_y) + \mathcal{C}(f_x - f_c, f_y) + \mathcal{C}^*(f_x + f_c, f_y), \quad (2.28)$$

where capital calligraph letters indicate the Fourier transforms of their italic lower-case counterparts and (f_x, f_y) are the frequency coordinates corresponding to (x, y) .

A representative spectrum, obtained upon Fourier transforming the distribution in Fig. 2.2(b), is shown in Fig. 2.2(c) on a logarithmic scale (only its modulus is shown). Equation (2.28) indicates that, provided that f_c and consequently θ are large enough, the spectra $\mathcal{A}(f_x, f_y)$, $\mathcal{C}(f_x, f_y)$ and $\mathcal{C}^*(f_x, f_y)$ are separated in the frequency domain. A bandpass filter is then applied to $\mathcal{I}(f_x, f_y)$, so that $\mathcal{C}(f_x - f_c, f_y)$ is the only left contribution. A shift of $\mathcal{C}(f_x - f_c, f_y)$ towards the origin by f_c and subsequent inverse Fourier transform yield $c(x, y)$. Finally, the phase difference $\Delta\phi(\mathbf{x})$ is obtained by taking the argument of $c(x, y)$, as follows

$$\Delta\phi(\mathbf{x}) \bmod 2\pi = \arctan2\{\text{Im}[c(\mathbf{x})], \text{Re}[c(\mathbf{x})]\}. \quad (2.29)$$

Because a plane wave is typically used as the reference beam, $\phi_R(\mathbf{x})$ varies much slower than $\phi_O(\mathbf{x})$, and the phase difference $\Delta\phi(\mathbf{x})$ is essentially $-\phi_O(\mathbf{x})$. The amplitude of the object beam $A_O(\mathbf{x})$ is obtained from the diffraction pattern of the object only, by blocking the reference beam, i.e., $|A_O(\mathbf{x})|^2$.

At this stage, both the amplitude [Fig. 2.2(d)] and the phase [Fig. 2.2(e)] of the object beam have been retrieved at the camera plane. Because in the setup shown in Fig. 2.2(a) the camera plane is perpendicular to \mathbf{k}_O , the complex amplitude of Eq. (2.22) can be simplified to $A_O(\mathbf{x}) \exp[i\phi_O(\mathbf{x})]$. This quantity is finally propagated back to the object plane via the back-propagation operator of Eq. (2.15), yielding the holographic reconstruction of the object [Figs. 2.2(f)-(g)].

Lateral resolution

The lateral resolution ρ of off-axis digital holographic reconstructions has been shown to be [Picart and Leval, 2008]

$$\rho = \frac{\lambda d}{D} \quad (2.30)$$

where d is the distance from the object to the detection plane, and D is the size of the detection plane along the direction where the resolution is evaluated. A glance at Eq. (2.30) reveals that it can only be an approximate estimate, as it predicts vanishing values of ρ with vanishing d , thus contradicting the ultimate resolution limit for diffraction limited imaging given by Abbe, i.e., $\rho \geq \lambda/2$ [Born and Wolf, 2013]. Indeed such expression has been obtained in the so-called *Fresnel diffraction regime*, i.e., for distances $d \gg D$. In Chapter 7 we are going to obtain an expression for ρ consistent with Abbe's limit and therefore valid for any value of d .

2.4 Ptychography

Ptychography is another lensless solution to the phase problem. Unlike holography, it does not rely on the interference with a reference wave. Therefore, it is usually referred to as a *non-holographic* approach. Its first concept was developed by

Walter Hoppe for imaging periodic (crystalline) objects with electrons [Hoppe, 1969], but only its extension to non-periodic objects had an impact so far, such that nowadays ptychography is mostly applied to biological samples, exhibiting no periodicity whatsoever. Ptychography relies on collecting multiple diffraction patterns by scanning an object across a coherent beam to overlapping positions [Fig. 2.3(a)]. If the object is illuminated under varying incident angles instead, the technique is called Fourier ptychography [Zheng et al., 2013], as it can be regarded as the reciprocal space counterpart of ptychography. The marriage of the ptychographic approach with efficient iterative algorithms, pioneered by John Rodenburg and Helen Faulkner [Rodenburg and Faulkner, 2004; Rodenburg, 2008], started a widespread scientific interest in ptychography. Ptychographic algorithms have been developed for more than ten years [Maiden et al., 2017], for example, dealing with the reconstruction of both the object transmission function and the wavefront impinging on it [Thibault et al., 2008; Thibault et al., 2009; Maiden and Rodenburg, 2009], improving the knowledge of the relative shifts between the object and the beam [Maiden et al., 2012a], optimizing the scan parameters [Edo et al., 2013; Silva and Menzel, 2015], accounting for partial coherence of the radiation source [Thibault and Menzel, 2013], and overcoming its depth-of-field limitations with multi-slice approaches [Maiden et al., 2012b; Tsai et al., 2016]. Being a lensless technique, ptychography mostly benefited to the X-ray community [Pfeiffer, 2018], however it was also realized in the extreme-ultraviolet [Gardner et al., 2017] and optical [Maiden and Rodenburg, 2009] regimes. Experimental variants, other than transmission, include the combination with computed tomography [Holler et al., 2017] or Fresnel diffractive imaging [Vine et al., 2009], the implementation in reflection [Seaberg et al., 2014] and scattering [Godard et al., 2011; Mastropietro et al., 2017] mode, and in the time domain for the reconstruction of ultrafast pulses [Spangenberg et al., 2015; Lucchini et al., 2015]. A review on the state of the art of ptychographic imaging, especially using X-rays, has been recently contributed by Franz Pfeiffer [Pfeiffer, 2018].

In the next section, the “extended ptychographical iterative engine” (ePIE) algorithm will be described, through which both the object and the wavefront incident on it can be reconstructed [Maiden and Rodenburg, 2009]. If the latter is already known from preliminary calibrations, the ePIE algorithm easily reduces to the “ptychographical iterative engine” (PIE), reconstructing the object only [Rodenburg and Faulkner, 2004]. Owing to its flexibility, this algorithm will be employed in the ptychographic reconstructions performed in the next Chapters.

2.4.1 The extended Ptychographic Iterative Engine (ePIE) algorithm

A schematic of a ptychographic setup in transmission is shown in Fig. 2.3(a). A coherent beam, also known as “probe”, is defined by an aperture and impinges

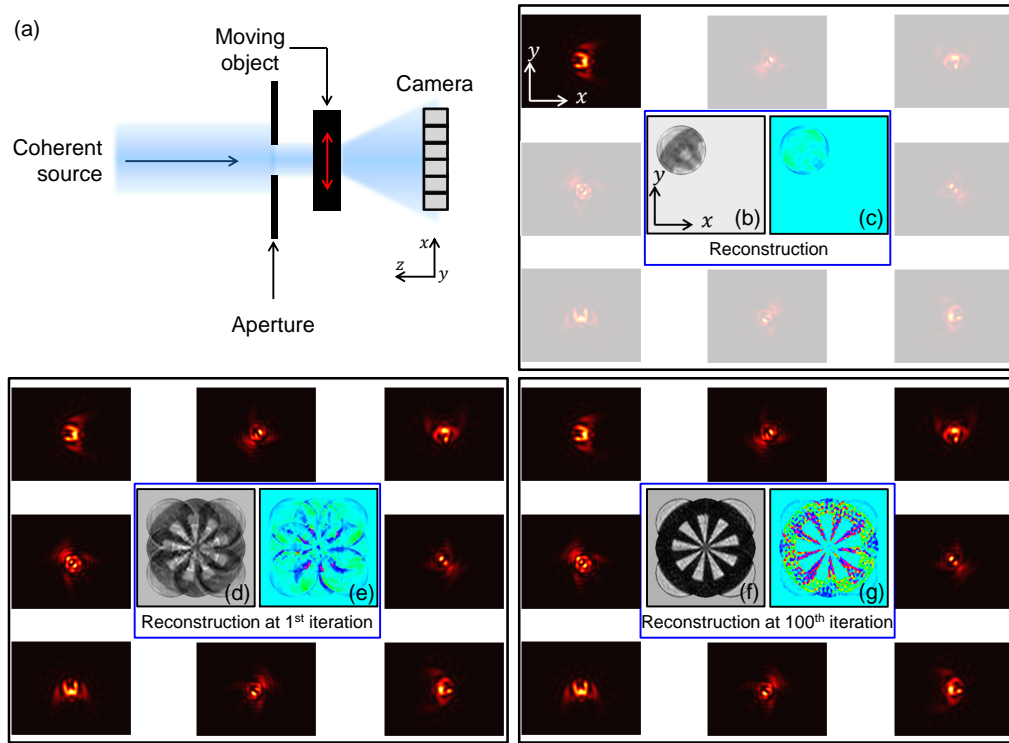


Fig. 2.3.: (a) Typical experimental setup of ptychography in transmission. Simulated results: (b) Amplitude and (c) phase of the reconstructed object after using the diffraction pattern highlighted in the top right panel. (d) [(f)] Amplitude and (e) [(g)] phase of the reconstructed object after the 1st [100th] iteration.

on the object. A set of K diffraction patterns, referred to as “ptychograms”, $I_k(\mathbf{x})$, $k = 1, \dots, K$, is recorded by a camera, while scanning the object across the object plane by shifts \mathbf{x}_k with respect to the probe. Provided that the illuminated regions of the object partially overlap at neighboring scan positions [Bunk et al., 2008], both the probe $p(\mathbf{x})$ and the object transmission function $o(\mathbf{x})$ at the object plane can be iteratively reconstructed from the measured $I_k(\mathbf{x})$ and the shifts \mathbf{x}_k . An algorithm which can solve this task is the ePIE algorithm. At the start, the algorithm is fed with estimates of the probe and the object transmission function. If the object thickness t satisfies [Tsai et al., 2016]

$$t \lesssim 5.2\rho^2/\lambda, \quad (2.31)$$

where ρ is the desired lateral resolution, the interaction between the probe and the object can be written according to the following “multiplicative approximation”:

$$\psi_k(\mathbf{x}) = p_k(\mathbf{x}) o_k(\mathbf{x} - \mathbf{x}_k). \quad (2.32)$$

Here $p_k(\mathbf{x})$, $o_k(\mathbf{x})$ and $\psi_k(\mathbf{x})$ are, respectively, the k th estimates of the probe, the object transmission function and the “exit wave”, namely the wavefront exiting the object plane. Note, that Eq. (2.31) appears a reasonable estimate of the maximum

object thickness if one recalls that the depth of field of an imaging system is indeed on the order of ρ^2/λ [Goodman, 2005]. A numerical propagation of the estimated exit wave to the camera plane is then performed through the convolution kernel $h_d(\mathbf{x})$ of Eq. (2.14), where d indicates the distance from the object plane to the camera plane:

$$\Psi_k(\mathbf{x}) = \psi_k(\mathbf{x}) * h_d(\mathbf{x}). \quad (2.33)$$

The choice of the propagator $h_d(\mathbf{x})$ is motivated by the Fresnel number N_F at which the experiments are carried out. Considering an example relevant to the scope of this thesis, one can conduct a THz ptychography experiment with a probe as large as $w = 3$ mm, $\lambda = 0.1$ mm and $d = 10$ mm, yielding $N_F \equiv w^2/(\lambda d) = 9$ and making the far-field or Fraunhofer approximation, commonly used in the X-ray regime, unacceptable. As a next step the ‘‘intensity constraint’’ is applied, consisting of replacing the calculated modulus of the propagated exit wave with the measured one, and leading to the corrected k th estimate of the exit wave at the camera plane and at the object plane, as in Eqs. (2.34) and (2.35), respectively:

$$\Psi'_k(\mathbf{x}) = \sqrt{I_k(\mathbf{x})} \frac{\Psi_k(\mathbf{x})}{|\Psi_k(\mathbf{x})|}; \quad (2.34)$$

$$\psi'_k(\mathbf{x}) = \Psi'_k(\mathbf{x}) * h_{-d}(\mathbf{x}). \quad (2.35)$$

Finally, the updated object transmission function and probe are created according to the following equations (derived and discussed in Appendix A):

$$o_{k+1}(\mathbf{x}) = o_k(\mathbf{x}) + \alpha^{(o)} \frac{p_k^*(\mathbf{x} + \mathbf{x}_k)}{\max |p_k(\mathbf{x} + \mathbf{x}_k)|^2} [\psi'_k(\mathbf{x} + \mathbf{x}_k) - \psi_k(\mathbf{x} + \mathbf{x}_k)]; \quad (2.36a)$$

$$p_{k+1}(\mathbf{x}) = p_k(\mathbf{x}) + \alpha^{(p)} \frac{o_k^*(\mathbf{x} - \mathbf{x}_k)}{\max |o_k(\mathbf{x} - \mathbf{x}_k)|^2} [\psi'_k(\mathbf{x}) - \psi_k(\mathbf{x})], \quad (2.36b)$$

where $\alpha^{(o)}$ and $\alpha^{(p)}$ are scalar and positive feedback parameters ≤ 1 weighting the updates of the object and probe functions, respectively. If $p(\mathbf{x})$ is known *a priori*, its update can be avoided upon setting $\alpha^{(p)} = 0$, thus leading to the PIE algorithm. The convergence of the solutions can be monitored through the following normalized error:

$$E \equiv \frac{\sum_{k=1}^K \sum_{\mathbf{x}} \left| \sqrt{I_k(\mathbf{x})} - |\Psi_k(\mathbf{x})| \right|^2}{\sum_{k=1}^K \sum_{\mathbf{x}} I_k(\mathbf{x})}. \quad (2.37)$$

Equations (2.36) represent the new estimates of the object and probe functions, which will be used again in Eq. (2.32), where another shift from the set of \mathbf{x}_k will be considered. This procedure is repeated, each time using the ptychograms in a randomly shuffled order, for a predefined number of iterations, or until the error E has decreased below a chosen threshold. The panels in Fig. 2.3 summarize

the procedure for the reconstruction of a nine-spoked Siemens Star, using the ptychograms shown in each panel. Figures 2.3(b)-(c) show the amplitude and the phase of the reconstructed object using the highlighted top left ptychogram, whereas Figs. 2.3(d)-(g) show the same results after using all the ptychograms once (end of 1st iteration) and 100 times (end of 100th iteration).

2.5 Single-Beam Multiple-Intensity Reconstruction (SBMIR) phase retrieval

The Single-Beam Multiple-Intensity Reconstruction (SBMIR) phase retrieval algorithm is another non-holographic solution to the phase problem [Pedrini et al., 2005]. Like ptychography (section 2.4), it relies on iteratively reconstructing the object transmission function using a set of diffraction patterns I_k , $k = 1, \dots, K$, acquired in different configurations. However, here they are recorded while stepping the camera along the optical axis and without moving the object, as shown in Fig. 2.4(a). Examples of diffraction patterns are given in Fig. 2.4(b), where a nine-spoked Siemens Star was used as object. Therefore, denoting with $o(\mathbf{x})$ the unknown object transmission function, a SBMIR dataset can be written as,

$$I_k(\mathbf{x}) = |\Psi_k(\mathbf{x})|^2 \equiv |o(\mathbf{x}) * h_{d_k}(\mathbf{x})|^2, \quad (2.38)$$

where d_k are the distances from the object plane to the detector plane at each stepping position. At the start, the algorithm is fed with an initial guess of $o(\mathbf{x})$ and then it proceeds according to the following steps:

1. The estimate is numerically propagated by the distance d_1 , where the first recording plane is located;
2. The obtained diffraction pattern is corrected according to the same “intensity constraint” used in ptychography [Eq. (2.34)], by using the measured diffraction pattern at the first recording plane $I_1(\mathbf{x})$;
3. The corrected wavefield is then propagated to the second recording plane at the distance d_2 from the object plane, and the “intensity constraint” is applied again using $I_2(\mathbf{x})$;
4. The above step is repeated for the remaining recording planes at d_k using $I_k(\mathbf{x})$;
5. After the diffraction patterns have been used once, the corrected wavefield at the plane d_k and back-propagated to the object plane is the current estimate of $o(\mathbf{x})$, which can be used again in step 1.

Also in this case, the procedure is repeated a predefined number of iterations, or until a suitable error metric becomes lower than a chosen threshold. Figure 2.4(c) shows the reconstructed amplitude and phase after using the diffraction patterns from Fig. 2.4(b) once (end of 1st iteration) and 10 times (end of 10th iteration).

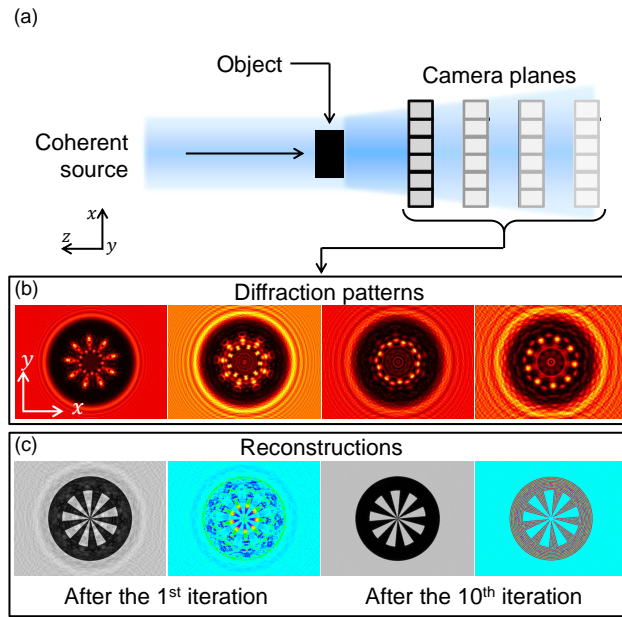


Fig. 2.4.: (a) Typical experimental setup of the SBMIR phase retrieval. (b) Simulated diffraction patterns at 4 distances from the object plane. (c) Amplitude and phase of the reconstructed object after using the diffraction patterns from (b) once (1st iteration) and 10 times (10th iteration).

2.6 Conclusions

In this Chapter, the two key points of coherent lensless imaging have been discussed, namely the propagation of electromagnetic waves in free space, which was treated within the scalar diffraction theory, and the phase problem. We have detailed three imaging techniques, capable of reconstructing the complex wavefront diffracted by an object and which will be used and compared in the next Chapters.

All the methods outlined in this Chapter are valid irrespective of the wavelength of the electromagnetic waves. In this work, we are going to use THz radiation, which has been already introduced in Chapter 1 and whose generation and detection processes as well as applications will be described in the next Chapter.

Overview of THz radiation

Here a short overview of THz radiation will be provided, discussing the major THz imaging techniques reported so far, as well as the THz sources and detectors used to implement them. Although this Chapter serves as a means to place our later results in the context of THz imaging, we would like to stress that THz research is tremendously active and spans so many fields that only an outline can be given here. The interested reader may find the recent reviews [Dhillon et al., 2017; Mittleman, 2018; Guerboukha et al., 2018] more exhaustive.

3.1 THz radiation

THz radiation denotes the portion of the electromagnetic spectrum whose frequency lies around 1 THz. The limits of the THz band are only loosely defined however, quoting the International Telecommunication Union, “[The term] Terahertz waves [...] usually refers to the frequency band between 0.1 THz-10 THz with the corresponding wavelength of 0.03 mm-3 mm.” [*Report of the International Telecommunication Union*], and therefore it locates between the infrared and the microwave regions of the electromagnetic spectrum, as shown in Fig. 3.1.

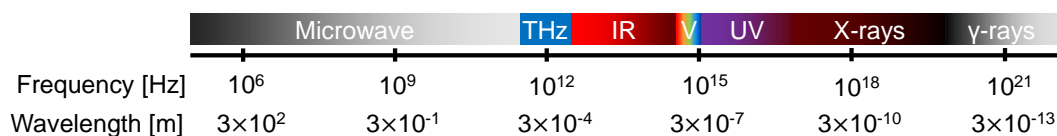


Fig. 3.1.: The electromagnetic spectrum hosts the THz band between the infrared and the microwave regions.

Although the first application of THz radiation dates back to the 1970s, when the development of THz gas lasers allowed imaging with THz waves [Hartwick et al., 1976], the lack of efficient THz sources and detectors prevented the establishment of THz analytical techniques for 10 more years, justifying the term “THz gap” used to refer to this frequency region. The use of THz radiation underwent its major boost in the late 1980s, when the advancements in ultrafast lasers triggered the development of broadband THz sources and coherent detectors [Fattinger and Grischkowsky, 1988].

Table 3.1, reporting the most common units used to describe THz radiation at the representative frequency of 1 THz, gives a hint on why THz radiation is a suitable tool in a wide variety of applications. Because of its period and photon energy, THz radiation has been used to investigate, on a ps time scale, the dynamics of systems exhibiting transitions in the meV range, such as two-dimensional electron gases

[Chatterjee et al., 2009], excitons [Leinß et al., 2008], and aqueous systems [He et al., 2008], to name only a few. Because water strongly absorbs radiation in the THz range, THz waves can provide effective contrast to image, e.g., cancer tissues [Yu et al., 2012] and the water content in plants [Gente and Koch, 2015]. Furthermore the low energy of THz photons, combined with their shallow penetration depth in living tissues, makes THz waves a harmless probe for skin diagnosis [Fan et al., 2017; Hernandez-Cardoso et al., 2017]. Owing to its negligible interaction with several non-conducting materials, including polymers, dielectrics and intrinsic semiconductors, THz radiation can penetrate through them and reveal inner defects or even allow thickness measurements in industrial processes [May et al., 2011].

Frequency ν [THz]	Period $T \equiv \nu^{-1}$ [ps]	Wavelength $\lambda \equiv c/\nu$ [μm]	Wavenumber $\bar{k} \equiv \lambda^{-1}$ [cm^{-1}]	Photon energy $E \equiv h\nu$ [meV]
1	1	300	33.3	4.14

Tab. 3.1.: Period, wavelength, wavenumber and photon energy of THz radiation at a frequency of 1 THz. $c \approx 3.0 \times 10^8$ m/s is the speed of light in vacuum, and $h \approx 6.6 \times 10^{-34}$ J s is Planck's constant.

3.2 THz imaging techniques

The investigation of materials with THz radiation goes hand in hand with the development and implementation of THz imaging techniques, which must be chosen according to the requirements set by the problem. Table 3.3 includes a representative list of the THz imaging techniques which are current research trends, along with their advantages, drawbacks and successful application cases. The entries corresponding to the technique of choice for the studies reported in this thesis are written in bold. In what follows, an overview of the most common sources and detectors of THz radiation for THz imaging will be given. Particular emphasis will be put on the equipment used in the experiments of this work.

3.3 THz sources

Numerous sources of THz radiation are currently available for THz imaging. In particular, the rapid advancement of semiconductor technology enabled the development of several solid-state THz sources. Table 3.4 provides a summary of THz sources, including natural ones. For those which are commercialized, the name of one representative company has been indicated. As in Table 3.3, the THz source employed in our experiments corresponds to the entry written in bold, and it is described in more detail in the next subsection.

3.3.1 The THz gas laser system

The THz source used in the experiments reported in the next Chapters is the FIRL 100 Far-Infrared (FIR) laser system produced by Edinburgh Instruments Ltd (Edinburgh, Scotland, United Kingdom) [*Edinburgh Instruments FIRL 100 system*]. The system provides around 50 coherent, monochromatic and linearly-polarized discrete emission lines in the wavelength range $41 - 1890 \mu\text{m}$, corresponding to frequencies ranging from 0.16 to 7.3 THz, with a maximum output power of 150 mW at the wavelengths of $118.8 \mu\text{m}$ and $184.3 \mu\text{m}$. It consists of a CO₂ section, including the CO₂ laser for pumping the THz active medium, and a THz section, including the THz laser cavity.

CO₂ section

Optical pumping is achieved with a CO₂ laser providing 83 emission lines in the wavelength range $9.174 - 10.885 \mu\text{m}$, arising from transitions between the vibrational-rotational levels of the CO₂ molecule [Witteman, 2013]. Figure 3.2 shows the emission lines and their power, according to the specification sheet of the manufacturing company. They are grouped in two rotational branches, according to the change in the rotational quantum number Δj . The P-branch includes the lines originating from $\Delta j = -1$, whereas the R-branch denotes the transitions with $\Delta j = 1$. Within each branch, the power of the lines follows the well-known Boltzmann distribution for the rotational line probabilities [Atkins and De Paula, 1998]. Both branches are replicated in two vibrational bands, centered around the wavelengths $9.4 \mu\text{m}$ and $10.4 \mu\text{m}$. The lines are identified with the notation VBJ , where $V \in \{9, 10\}$ denotes the vibrational band (9 for the band at $9.4 \mu\text{m}$ and 10 for the band at $10.4 \mu\text{m}$), $B \in \{P, R\}$ indicates the rotational branch, and J is the rotational quantum number of the lower level involved in the transition. In this notation, the three pump lines used in our experiments are 9R18, 9R10 and 9P36. The laser active medium is a gas mixture, composed of 7% CO₂ (99.995% purity), 18% N₂ (99.999%) and 75% He (99.999%) at a total pressure in the range 20 – 30 mbar, which undergoes electric discharge and laser emission after being supplied with high voltage. The cavity is equipped with a pair of ZnSe Brewster windows, setting the polarization to the linear vertical direction and a Au-coated diffraction grating for line selection. Steering mirrors and a ZnSe output lens couple the beam into the cavity of the THz laser.

THz section

The emission of THz radiation is caused by rotational transitions of organic and polar molecules in gas phase [Douglas, 2013]. Several chemical compounds undergoing such emission scheme have been identified. These include, among others, CH₃OH, HCOOH, CH₃F and some of their isotopomers [Moruzzi, 2018; Gallagher et al., 1977; Douglas, 2013], used at pressures around 10^{-1} mbar. For the experiments

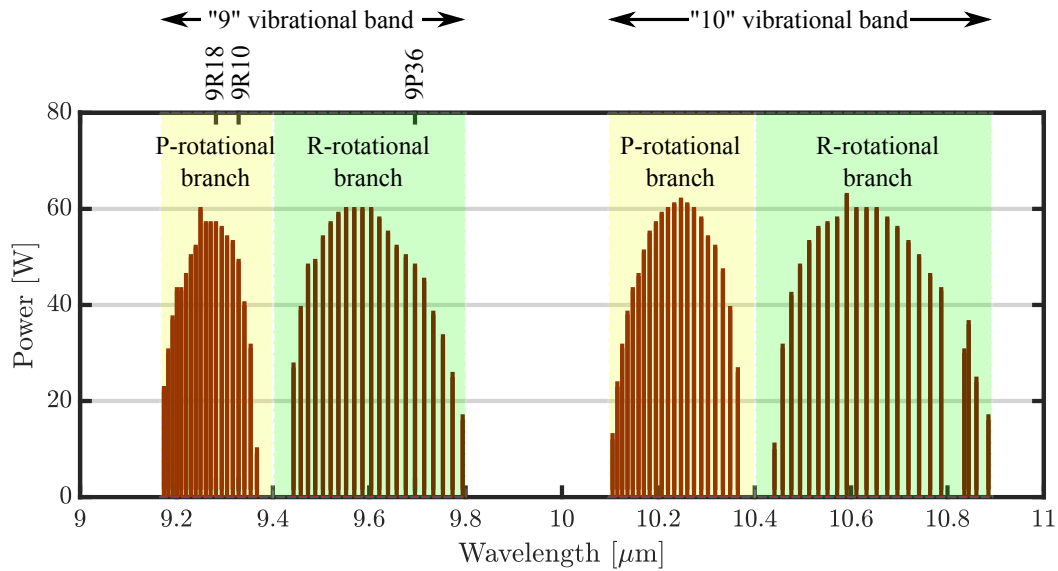


Fig. 3.2.: Vibrational-rotational emission lines of the CO₂ molecule and their power, obtained from the specification sheet of the THz gas laser system.

performed in this work, three emission lines of CH₃OH will be employed, which are listed in Table 3.2 together with their wavelength, exciting line from the CO₂ laser, polarization relative to that of the pump, and power. THz radiation is coupled out of the THz section through a dichroic window, which blocks the infrared pump beam. This can be translated by the user, allowing the length of the THz cavity to be optimized for the desired THz wavelength.

Lasing molecule	Wavelength [μm]	CO ₂ pump line	Relative polarization	Power [mW]
CH ₃ OH	96.522	9R10		90
CH ₃ OH	118.834	9P36	\perp	150
CH ₃ OH	393.631	9R18		40

Tab. 3.2.: Specifications of the three THz emission lines used in the experiments reported in this thesis. The polarization is given with respect to that of the pump infrared beam.

The thermal stability of the whole system is ensured through water-cooling and five invar rods, which also guarantee mechanical stability. After several years of use of the system, we identified the following flaws:

1. Although the position of the outcoupling window in the THz section can be finely adjusted, its value cannot be read by the user. Furthermore, its control is subject to a considerable backlash, making the optimization of the length of the THz cavity a hardly reproducible task;
2. The alignment of the ZnSe optics coupling the infrared beam into the THz cavity can only be adjusted by redirecting the powerful infrared beam out

of the system, which poses a danger to the user. In such a situation, the micrometer screws used for the alignment are difficult to access;

3. The THz power can only be considered stable (namely, subject to variations of less than 10%) within time windows of around 20 minutes.

It is noteworthy that some of these issues have also been encountered by R. Tesař, who modified the system in order to solve problem 1. in the above list as reported in his PhD thesis [Tesař, 2018].

3.4 THz detectors

The most common types of THz detectors are listed in Table 3.5, in a similar way as done for the THz sources in Table 3.4. The detectors written in bold will be used in a comparative study in Chapter 4, together with two other microbolometer cameras, which are not included in Table 3.5 because specifically designed to operate in the infrared region of the spectrum.

3.5 Conclusions and outlook

In this Chapter we have outlined the current state of the research on THz radiation, in terms of imaging techniques and sources and detectors used in their implementations. Although this summary cannot be considered an exhaustive review of the whole research on THz radiation, we hopefully made it clear that THz radiation is a tool holding great promise in such diverse fields, as the investigation of materials, biomedical imaging and non-destructive industrial inspection.

In this broad context, the work reported in the next Chapters will focus on continuous-wave THz imaging, performed with the THz gas laser of section 3.3.1 and a camera. The choice of the latter will be the topic of the next Chapter.

Technique	Working principle, ✓ advantages and × drawbacks	Applications	Sample reference
Pulsed imaging with THz time-domain spectroscopy	Broadband THz pulses interact in transmission or in reflection with the sample. The pulses after the interaction are measured in the time domain.	Non-invasive mapping of the electrical properties of graphene.	[Mackenzie et al., 2018; Bøggild et al., 2017]
	✓ Amplitude and phase of the THz electric field are measured in the time domain owing to the ultrafast coherent acquisition.	Quality control of coatings of, e.g., pharmaceutical tablets.	[May et al., 2011]
	× The THz pulse incident on the sample must be synchronized, through an optical delay line, with an optical pulse triggering the acquisition, in order to record the time evolution of the THz electric field. This makes the setup more complicated than in continuous-wave THz imaging.	Non-invasive spectral imaging of layered structures, e.g. paintings and books.	[Koch-Dandolo et al., 2015; Redo-Sanchez et al., 2016]
Continuous-wave THz imaging	× Single-pixel detectors are usually employed, so an image can only be obtained by scanning the sample across the THz pulse.		
	Continuous-wave THz beams interact in transmission or in reflection with the sample. Their intensity after the interaction is measured with a camera.	Non-invasive imaging through non-conductive materials, e.g. plastics.	[Locatelli et al., 2015]
	✓ No synchronous detection is required, making the setup easy and flexible.	Three-dimensional imaging of dried biological specimens.	[Bessou et al., 2012]
	✓ Availability of THz cameras, obviating the need for point-by-point scanning of the sample.		
	× The phase of the THz beam is not measured by the camera, but it has to be computationally retrieved.		
	× Temporal resolution is not available.		

THz near-field imaging	<p>THz beams transmit through a sub-wavelength aperture or are scattered by a sub-wavelength tip before they interact with the sample, placed at a distance comparable to the THz wavelength (near-field). The recording of the THz beams after interaction is also performed in the near-field, to collect the evanescent waves scattered by the sample.</p> <ul style="list-style-type: none"> ✓ The THz spot size is set by the diameter of the aperture or of the tip, thus allowing imaging with a spatial resolution orders of magnitude lower than the THz wavelength. × The sensitivity decreases with smaller apertures or tips. 	<p>Mapping of carrier concentration in single semiconductor nanodevices.</p> <p>Imaging the ultrafast electron capture in a semiconductor nanodot.</p>	<p>[Huber et al., 2008]</p> <p>[Cocker et al., 2013]</p>
THz single-pixel imaging via compressive sensing	<p>The intensity of the THz beams after interaction with the sample and after transmitting through a pixelated mask, featuring opaque and transparent pixels, is recorded with a single-pixel detector.</p> <ul style="list-style-type: none"> ✓ Two-dimensional array detectors are not required. ✓ If the object is sparse in a given representation, it can be reconstructed from a number of intensity patterns, recorded with different masks, lower than the number of object pixels. × Careful choice of the pixelated masks is needed. × The object must be sparse. 	<p>Three-dimensional imaging of cm-sized objects with mm resolution.</p>	<p>[Jin et al., 2009]</p>

Tab. 3.3.: Description of the most used THz imaging techniques. The list has been compiled based on [Guerboukha et al., 2018] and the references therein.

Source	Working principle	Typical operation frequency [THz]	Operation temperature	Output power	Selling companies (if commercialized)	Sample reference
Mercury lamp	Electric discharge in vaporized mercury	0.12-6 besides several discrete UV emission lines	Room	Tens of μW		
Cosmic background	Blackbody thermal emission	Broadband	Room	$\sim \mu\text{W}$		
Backward-wave oscillator	Backward emission from a traveling electron beam interacting with a RF signal	Several sub-THz bands, e.g. 0.19-0.20	Room	20 W peak		[He et al., 2015]
Free electron laser	Coherent emission from a bunched electron beam interacting with a sinusoidal magnetic field	Several THz bands, e.g. 1.3-2.5	Room	400 W average, 1 MW peak		[Gavrilov et al., 2007]
Gunn diodes	Electrical oscillations in a two-terminal negative resistance solid-state device	0.3	Room	$28 \mu\text{W}$ average		[Khalid et al., 2014]
Frequency multipliers of microwave sources	Frequency multiplication in solid-state devices	0.3	Room	5.4 mW average		[Yao et al., 2014]
Gas laser	Rotational transitions of organic polar molecules	Several discrete lines in the band 0.5-5	Room	150– 500 mW average	Edinburgh Instruments	[<i>Edinburgh Instruments Far Infrared / THz lasers</i>]
Quantum cascade laser (QCL)	Coherent emission from electrons relaxing through the subbands of a quantum well heterostructure	3-4	Several temperatures in the range 8 K - room	<5 mW peak pulsed at room temperature		[Belkin and Capasso, 2015]

Difference frequency generation using two mid-infrared QCLs	Nonlinear interaction between two beams pumped in a second-order nonlinear crystal	3.5	Room	1.9 mW peak		[Razeghi et al., 2015]
Photomixer	Frequency difference between two optical beams in a semiconductor structure	1	Room	$1 \mu\text{W}$ average		[Ishibashi et al., 2014]
Parametric amplification	Frequency conversion of a pump pulse into two pulses with lower frequencies in a second-order nonlinear crystal	Tunable in the band 0.7-2.9	Room	50 kW peak		[Minamide et al., 2014]
Optical rectification	Quasi-DC polarization proportional to the envelope of a pump pulse transmitting through a second-order nonlinear crystal	Several bands, e.g. 0.1-4	Room	0.6 mW peak		[Vicario et al., 2015]
Photoconductive antenna	Relaxation of charge carriers in a biased semiconductor gap after ultrafast photoexcitation	0.1-5	Room	$>60 \mu\text{W}$ average	Toptica Photonics	[<i>Photoconductive antennas, Toptica Photonics</i>]

Tab. 3.4.: Description of the most known sources of THz radiation. The list has been compiled based on [Dhillon et al., 2017; Guerboukha et al., 2018] and the references therein.

Detector	Working principle	Typical operation frequency [THz]	NEP [$\text{pW}/\sqrt{\text{Hz}}$]	Available array size	Selling companies (if commercialized)	Sample reference
Microbolometer	Thermal. Resistance of the active material sensitive to changes of temperature	1-7	$<10^2$ @ 4 THz mod.	320×240	NEC	[Hack et al., 2016]
Pyroelectric detector	Thermal. Spontaneous electrical polarization of the active material sensitive to changes of temperature	0.1-300	10^4 @ 1 THz mod.	160×160	Ophir Photonics	[Spiricon Pyrocam IIIHR, Ophir Photonics]
Golay cell	Thermal. Thermal expansion of a gas upon absorption of radiation	0.2-20	10^4 @ 12.5 THz mod.	1×1	Microtech	[Golay cell, Microtech Instruments]
Schottky-barrier diode	Electronic. Fast switching speed in a semiconductor/metal junction	0.11-0.17	10^2	1×1	Virginia Diodes	[Schottky diodes, VDI]
		0.2	10^2	1×240		[Han et al., 2014]
Plasmonic field-effect transistor	Electronic. Electron density oscillations in a transistor channel	0.8-1	10^2 @ 5 kHz mod.	32×32		[Al Hadi et al., 2012]
Photoconductive antenna	Optically induced. Excitation of charge carriers in a biased semiconductor gap through an ultrafast optical pulse and subsequent acceleration through a THz pulse	0.1-5		1×1	Toptica Photonics	[Photoconductive antennas, Toptica Photonics]
		1		1×15		[Brahm et al., 2014]

Electro-optic sampling	Birefringence induced by a THz pulse and probed by an ultrafast optical pulse in a second-order nonlinear crystal	Several THz bands, e.g. 7-30 with a GaSe crystal	1×1	[Liu et al., 2004]
			384×288 †	[Wu et al., 1996]
Air-biased-coherent-detection	Optically induced. Four-wave mixing in air generating the second harmonic of an optical pump beam	0.2-30	1×1	[Dai et al., 2011]

Tab. 3.5.: Description of the most known detectors of THz radiation. “mod.” in the 4th column stands for “modulation” and refers to the modulation frequency at which the NEP was evaluated. The list has been compiled based on [Dhillon et al., 2017; Guerboukha et al., 2018] and the references therein.
 † Because an optical beam is recorded, a CCD camera was used in this case.

Comparison of thermal cameras for THz off-axis digital holography and real-time THz imaging

In a first study, we will compare the performance of four thermal cameras for their application to THz off-axis digital holography and real-time THz imaging. Their capability to image beam profiles and resolve sub-mm interference fringe patterns as well as their response across the detection plane will be assessed. The obtained results will allow us to make an educated choice of the camera that best suits our needs.

4.1 Cameras, THz laser source and setups

The following thermal cameras, capable of directly recording THz radiation via different operating principles, were considered:

1. A Long-Wave Infrared (LWIR) micro-bolometer whose resistive material is vanadium oxide (VOx), designed to operate in the wavelength range $[8, 14] \mu\text{m}$ (product name: Devitech IR-032);
2. A LWIR micro-bolometer whose resistive material is amorphous silicon (a-Si), designed to operate in the wavelength range $[8, 14] \mu\text{m}$ (Xenics Gobi-640-GigE);
3. A THz micro-bolometer whose resistive material is silicon nitride (SiN), designed to operate in the wavelength range $[43, 300] \mu\text{m}$ (NEC IRV-T0831);
4. A THz pyroelectric camera whose active material is lithium tantalate (LiTaO_3), designed to operate in the wavelength range $[1.06, 3000] \mu\text{m}$ (Spiricon Pyrocam III HR);

Further specifications are summarized in Table 4.1. For the definition of NEP , $NETD'$ and D^* , the reader is referred to Appendix B.

The FIRL 100 gas laser presented in section 3.3.1 was used as a tunable THz source. Methanol (CH_3OH) was evaporated into its cavity as the lasing medium to achieve emission at the wavelengths $\lambda = 118.8 \mu\text{m}$ (2.5 THz) and $\lambda = 96.5 \mu\text{m}$ (3.1 THz), while formic acid (HCOOH) was used as a lasing medium to assess the performance of the cameras at $\lambda = 393.6 \mu\text{m}$ (0.76 THz).

In order to realize reproducible measurement conditions, all four cameras were mounted onto a common rail and aligned in such a way that their detection planes lied on a single plane perpendicular to the THz beam, as shown in Fig. 4.1(a). The power of the THz beam was monitored with a single-pixel pyroelectric detector placed in the low power arm of a beam splitter plate made of fused quartz. A shutter

Specification	LWIR-Bolometer	LWIR-Bolometer	THz Bolometer	Pyroelectric Camera
Product name	Devitech IR-032	Xenics Gobi-640-GigE	NEC IRV-T0831	Spiricon Pyrocam III HR
Short name	Cam1	Cam2	Cam3	Cam4
Active material	VOx	a-Si	SiN	LiTaO ₃
Designated λ - [μm] and ν - [THz] range	8-14 (22-37)	8-14 (22-37)	(43-300) 1-7	1.06-3000 0.1-300
Pixel size [μm]	NA	NA	NA	75
Pixel pitch [μm]	25	17	23.5	80
Number of pixels	640×480	640×480	320×240	160×160
Detection area [mm^2]	16.0×12.0	10.9×8.2	7.5×5.6	12.8×12.8
$NEP@B = 1 \text{ Hz}$ [nW]	(0.08)	(0.04)	<0.1	13
$NETD'$ [mK]	50	50	NA	NA
D^* [$\text{cm}\sqrt{\text{Hz/W}}$]	(3.1×10^7)	(4.3×10^7)	($>2.4 \times 10^7$)	(5.8×10^5)
ADC [bit]	14	16	14	16
Frame rate [fps]	50	50	30	50

Tab. 4.1.: Specifications according to the data sheets of the THz detectors compared in this work. Figures in parentheses are calculated.

was inserted into the beam to suppress the infrared background radiation. Each image used in our analysis was the result of the subtraction of an image taken with the shutter closed, measuring the incoherent infrared emission from the scene at room temperature (dark frame), from an image taken with the shutter open, featuring the coherent THz beam on top of the incoherent infrared background. In cases where the THz power exceeded the saturation power of a camera, the THz beam was attenuated by inserting Teflon (PTFE) plates of appropriate thickness at the laser exit port. Depending on the experiment performed, different setups were implemented in the “Experiment area” of Fig. 4.1(a). In all cases, the beam size at the entrance of the “Experiment area” was $\approx 10 \text{ mm}$ (calculated at the $1/e^2$ point of a fitted Gaussian). For the measurements of the beam profile and the camera response, the beam size was reduced by a factor of 2 with a pair of Tsurupica lenses with 100 mm and 50 mm focal lengths in a Keplerian telescope arrangement [Fig. 4.1(b)]. The interference fringe contrast as well as the potential for real-time off-axis holography was assessed with the setup of Fig. 4.1(c). The incoming beam was split, with a polished steel cube, in two beams with equal amplitude, whose interference pattern at an off-axis angle $\theta \approx 10^\circ$ was recorded at the detection plane. This arrangement, where a pin was placed in the beam overlap area, also allowed us to align the detection planes of the cameras. The pin cast two diffraction patterns upon illumination from the two beams. We displaced each camera along the z -axis until these two diffraction patterns are symmetric with respect to the pin position and their distance is the same for all cameras. This ensured that all the detection planes lie on a single plane perpendicular to the propagation direction of the THz beam.

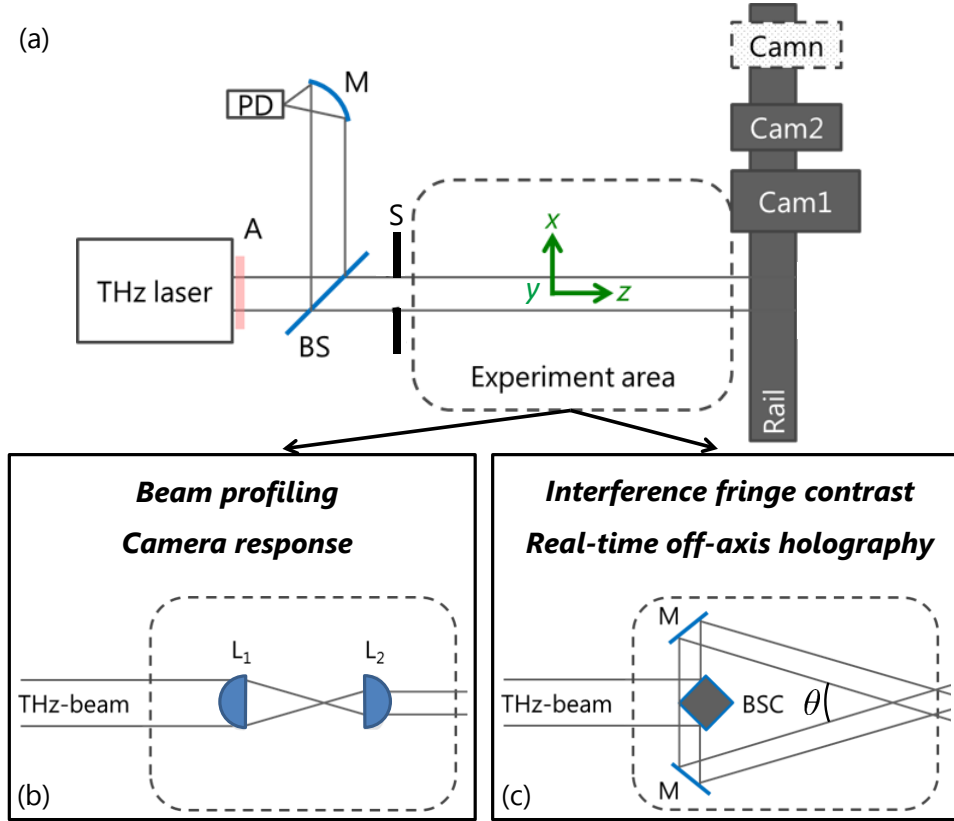


Fig. 4.1.: (a) General schematic of the experimental setup. (b) Experiment area for the beam profiling and camera response experiments. (c) Experiment area for the interference fringe contrast and real-time off-axis holography experiments. A: Teflon absorber plate; PD: single-pixel pyroelectric detector; M: Mirror; BS: 10/90 beam splitter; S: shutter; Camn: Camera #n; L₁, L₂: collimating lenses; BSC: surface reflecting beam splitter cube; θ : off-axis angle. Adapted from [Hack et al., 2016].

4.2 Methods

The performance of the cameras in the beam profiling (sections 4.2.1 and 4.3.1) and interference fringe contrast (sections 4.2.3 and 4.3.3) experiments was quantified with a properly defined signal-to-noise ratio SNR . Given two nominally equal images $I_1(\mathbf{x})$, $I_2(\mathbf{x})$, with $\mathbf{x} \equiv (x, y)$ in Fig. 4.1, taken in the same experimental conditions, the noise N was calculated as follows:

$$N \equiv \sqrt{\langle [I_1(\mathbf{x}) - I_2(\mathbf{x})]^2 \rangle_{\mathbf{x}}}, \quad (4.1)$$

where $\langle \rangle_{\mathbf{x}}$ stands for average over the camera pixels. The signal was defined depending on the experiment, as further detailed in the next sections. In order to account for drifts of the laser power during the experiments as well as different integration times of the cameras, the measured SNR , denoted as SNR_{exp} , was rescaled to a reference value SNR_{ref} using a reference power P_{ref} and a reference integration

time τ_{ref} as well as the corresponding experimental quantities P_{exp} , τ_{exp} according to

$$SNR_{\text{ref}} \equiv SNR_{\text{exp}} \frac{P_{\text{ref}}}{P_{\text{exp}}} \sqrt{\frac{\tau_{\text{ref}}}{\tau_{\text{exp}}}}. \quad (4.2)$$

Equation (4.2) reflects the fact that the signal is proportional to the beam power while the noise, according to the statistics of random uncorrelated variables, is inversely proportional to the square root of the number of averaged images. [†] Assuming a constant frame rate, the number of averaged images is proportional to the acquisition time, thus yielding Eq. (4.2). Note that in this study the SNR is always given in linear units, unlike in other fields of science and engineering, where logarithmic units are preferred.

4.2.1 Beam profiling

The detector plane of the camera was centered on the collimated THz laser beam [Fig. 4.1(b)]. The signal level used to estimate SNR_{exp} was the intensity measured at the beam center.

4.2.2 Camera response

In order to assess the performance of the cameras for full-field imaging, where the full detection plane is used, the variation of their response across the detection plane should be estimated. Note that, when imaging with coherent radiation, the quality of an image does not only depend on the figures of merit listed in Table 4.1, but also on other camera components, like its cover window and its housing, introducing interference and diffraction effects on the recorded image. To assess their response, the same collimated beam used for beam profiling was scanned across the detection plane at regular intervals and an image was recorded at each position. Denoting with \mathbf{x}_i the positions of the beam, with intensity $I_{\text{beam}}(\mathbf{x})$, the intensity of each recorded image $I_i(\mathbf{x})$ was modeled as

$$I_i(\mathbf{x}) = \mathcal{R}(\mathbf{x}) I_{\text{beam}}(\mathbf{x} - \mathbf{x}_i), \quad (4.3)$$

where $\mathcal{R}(\mathbf{x})$ is the camera response function. Equation (4.3) is analogous to the multiplicative interaction assumed at the object plane in ptychography [Eq. (2.32)], so both $\mathcal{R}(\mathbf{x})$ and $I_{\text{beam}}(\mathbf{x})$ can be estimated iteratively using update equations, like the ones given in Eqs. (2.36). Note, however, that both solutions are real in this case, as we limit ourselves to assessing the effect of the camera on the intensity of the beam. A flat and unitary distribution is usually a good first estimate of $\mathcal{R}(\mathbf{x})$, whereas the distribution $\langle I_i(\mathbf{x} + \mathbf{x}_i) \rangle_i$, obtained by averaging the measured intensities after compensating for their shifts, can be used as a starting guess of $I_{\text{beam}}(\mathbf{x})$.

[†]This result is also known as Bienaymé formula and, under the stronger assumption of independent random variables, as central limit theorem.

4.2.3 Interference fringe contrast

The two-beam interference setup of Fig. 4.1(c) was used to generate an interference pattern with a fringe spacing of $\Lambda = 0.7$ mm along the x -axis at $\lambda = 118.8$ μm , corresponding to $\theta \approx 10^\circ$. This value of Λ ensured that all cameras had a sufficient number of pixels across one fringe to reliably sample it. After removing the low-frequency thermal background and the high-frequency contributions caused by edge diffraction at the camera housing, the measured fringe pattern takes the form of Eq. (2.25) and can be written as

$$I(x) = I_0 + I_M \cos(2\pi x/\Lambda + \phi), \quad (4.4)$$

where I_0 is the average THz intensity, I_M is the modulation amplitude of the fringe pattern, and ϕ is a phase shift. The signal was identified with the peak-to-peak modulation amplitude $2I_M$.

4.2.4 Real-time off-axis holography

The capability of the cameras for real-time off-axis holography were evaluated at the reference integration time $\tau_{\text{ref}} = \tau_{\text{real-time}} = 40$ ms, corresponding to a typical video frame rate of 25 fps. The reference SNR , SNR_{ref} , was obtained from the experimental SNR_{exp} with $\tau_{\text{ref}} = \tau_{\text{real-time}}$ and a reference power $P_{\text{ref}} = 10$ mW. Alternatively, if we set the limit for useful experiments at $SNR_{\text{ref}} > SNR_{\text{min}}$, we can determine the minimum THz power P_{min} to surpass SNR_{min} . Conversely, fixing P_{ref} , one can estimate the minimum integration time $\tau_{\text{ref, min}}$ to surpass SNR_{min} .

Besides the SNR , the success of an off-axis holographic reconstruction depends on the capability to separate the satellite peaks at the carrier frequency in the Fourier plane from the background contribution at the origin. Because in the setup of Fig. 4.1(c) the carrier frequency is $\Lambda^{-1} = 2 \sin(\theta/2)/\lambda$, one should devise an experiment maximizing $\sin(\theta/2)$. On the other hand, Λ should be large enough to be sampled by the camera pixels. Assuming that the minimum resolvable Λ is sampled with 2 pixels, the upper limit $\sin(\theta_{\text{max}}/2) \equiv \lambda/(4\delta_x)$ is set to the allowed off-axis angle, where δ_x is the pixel pitch or, almost equivalently, the pixel size, along the direction of the interference fringes. Based on δ_x , the capability of the cameras to sample high spatial frequencies will be discussed.

4.3 Results and discussion

4.3.1 Beam profiling

Figure 4.2 shows a beam profile measured with the four cameras at $\lambda = 118.8$ μm . The image areas are scaled identically to represent the relative detector areas, such that the measured beam should have the same width. The asymmetric apparent shape of the beam is caused by the inhomogeneous response across the detector

area of some cameras and will be discussed in section 4.3.2 below. Reference values for the SNR of the beam profiles are compiled in the first two rows of Table 4.2 at $\lambda = 118.8 \mu\text{m}$ and $\lambda = 393.6 \mu\text{m}$.

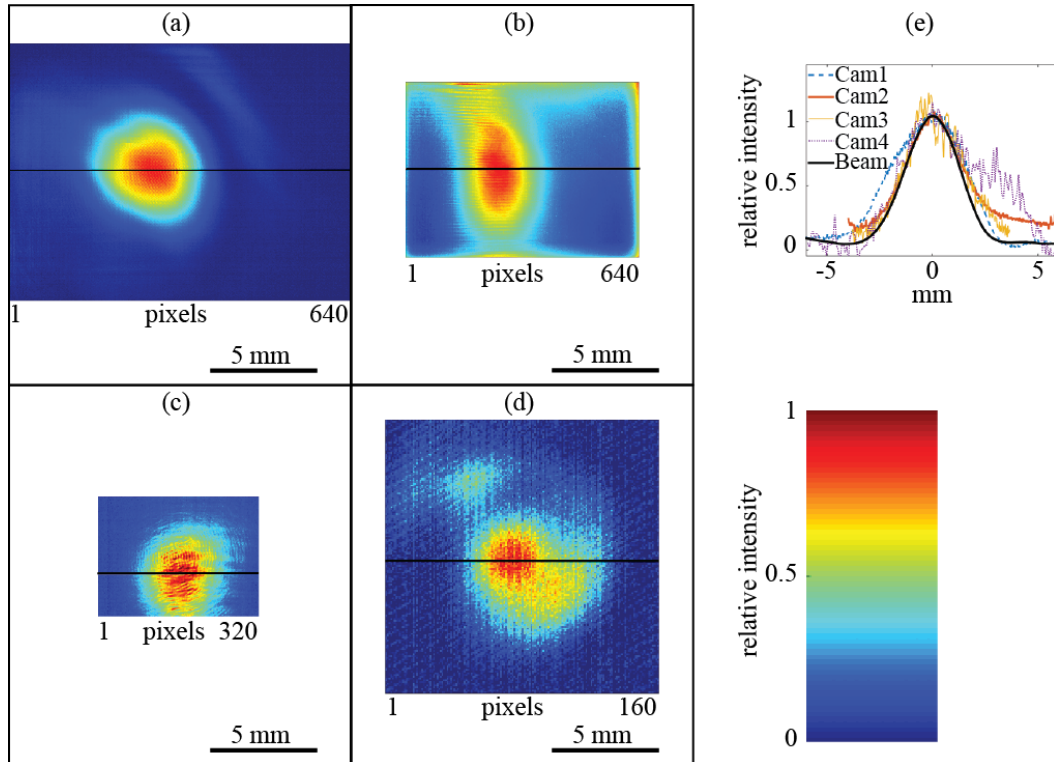


Fig. 4.2.: Beam profile measurements at $\lambda = 118.8 \mu\text{m}$ measured with the four cameras. (a) Cam1; (b) Cam2; (c) Cam3; (d) Cam4; (e) horizontal cross-section through black lines in (a)-(d) and nominal beam profile (black line). From [Hack et al., 2016].

Performance parameter	Cam1	Cam2	Cam3	Cam4
SNR_{ref} for beam profile@ $\lambda = 118.8 \mu\text{m}$	60	80	60	3
SNR_{ref} for beam profile@ $\lambda = 393.6 \mu\text{m}$	10	7	15	3
SNR_{ref} for interference fringes@ $\lambda = 118.8 \mu\text{m}$	85(70)	50	60(40)	0.5

Tab. 4.2.: Results of SNR_{ref} for the cameras at a THz power of $P_{\text{ref}} = 10 \text{ mW}$ and an integration time of $\tau_{\text{ref}} = 25 \text{ ms}$. Numbers in parentheses correspond to values obtained with an IR-filter in front of the camera.

4.3.2 Camera response

Figures 4.3(a)-(d) show the retrieved camera response $\mathcal{R}(\mathbf{x})$ at $\lambda = 118.8 \mu\text{m}$ as determined by scanning the beam across the detector area and according to the analysis outlined in section 4.2.2. We can appreciate diffraction effects from the camera edges and housing, either with rectangular [see, e.g., Fig. 4.3(b)] or circular [Fig. 4.3(c)] edges. While Cam2-4 have rather homogeneous responses,

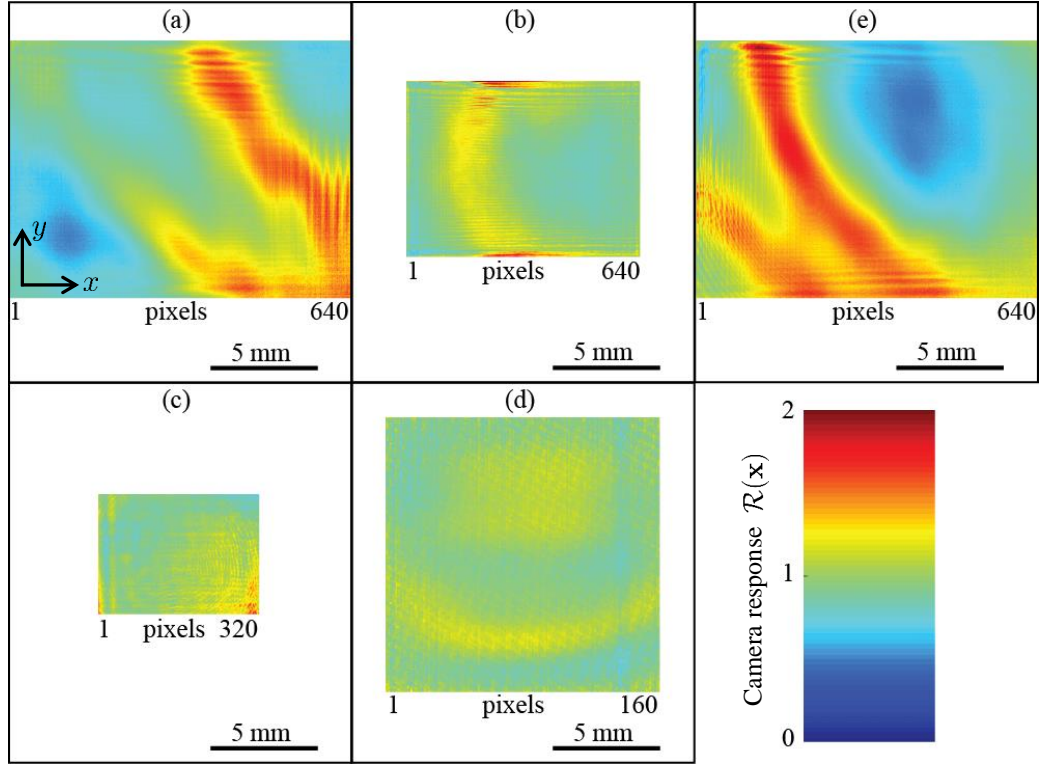


Fig. 4.3.: Camera response across the detection area, as defined in Eq. (4.3), (a)-(d) at $\lambda = 118.8 \mu\text{m}$. (a) Cam1; (b) Cam2; (c) Cam3; (d) Cam4; (e) Cam1 at $\lambda = 96.5 \mu\text{m}$. From [Hack et al., 2016].

the inhomogeneity across the response of Cam1 [Figs. 4.3(a), (e)] is attributed to interference effects resulting from a varying distance between the detector plane and the cover window. As a confirmation of this hypothesis, the response of Cam1 was also estimated at $\lambda = 96.5 \mu\text{m}$ [Fig. 4.3(e)], showing a shift in its maxima and minima, respectively arising from constructive and destructive interference of the waves multiply reflected by the detector plane and the cover window.

4.3.3 Interference fringe contrast

The effect of inhomogeneous camera responses on two-beam interference patterns is clear from Fig. 4.4, where the high-frequency components caused by diffraction at the camera edges have been enhanced for sake of illustration. The observed rectangular (left) and circular (right) patterns confirm the calculations of the camera responses in Figs. 4.3(b) and (c), respectively.

Figure 4.5 shows the same $5 \times 5 \text{ mm}^2$ -area from the fringe patterns measured with the four cameras. After calculating SNR_{exp} as explained in section 4.2.3, this was rescaled according to the reference values $P_{\text{ref}} = 10 \text{ mW}$ and $\tau_{\text{ref}} = 25 \text{ ms}$ and the obtained SNR_{ref} are compiled in the third row of Table 4.2 at $\lambda = 118.8 \mu\text{m}$.

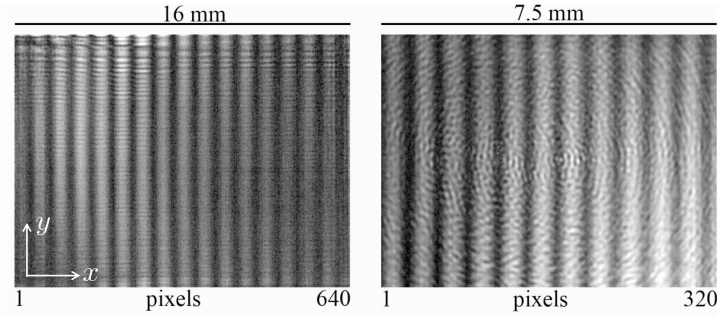


Fig. 4.4.: Two-beam fringe pattern interfering with the high-frequency diffraction patterns caused by the camera housing, measured at $\lambda = 118.8 \mu\text{m}$, for Cam2 (left) and Cam3 (right). From [Hack et al., 2016].

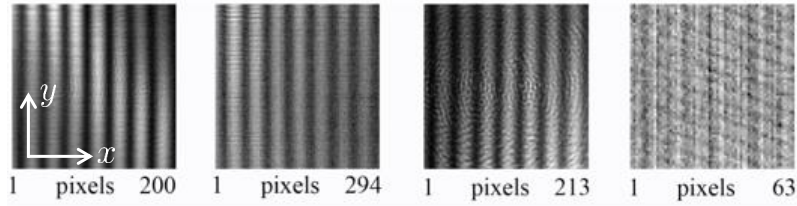


Fig. 4.5.: Central part ($5 \times 5 \text{ mm}^2$) of the two-beam fringe pattern recorded on Cam1 to Cam4 (left to right) at $\lambda = 118.8 \mu\text{m}$. From [Hack et al., 2016].

A direct comparison of SNR_{ref} for beam profiling and interference fringes is not possible due to different experimental conditions.

4.3.4 Real-time off-axis holography

The performance values defined in section 4.2.4 and derived from THz off-axis digital holography experiments are shown in Table 4.3 along with θ_{max} . Note that, even in the most pessimistic case of SNR using Cam4, a minimum THz power of 50 mW has been estimated to allow real-time THz off-axis digital holography. This power level is currently available from powerful continuous-wave THz sources, such as the gas laser used in this work.

Performance parameter	Cam1	Cam2	Cam3	Cam4
$SNR_{\text{ref}}@ \tau_{\text{ref}} = 40 \text{ ms}, P_{\text{ref}} = 10 \text{ mW}$	136	80	96	0.8
$\tau_{\text{ref}}@SNR_{\text{ref}} = 4, P_{\text{ref}} = 10 \text{ mW} [\text{ms}]$	0.035	0.100	0.069	1000
$P_{\text{ref}}@SNR_{\text{ref}} = 4, \tau_{\text{ref}} = 40 \text{ ms} [\text{mW}]$	0.29	0.50	0.42	50
$\theta_{\text{max}}@ \lambda = 118.8 \mu\text{m} [^\circ]$	180	180	180	44
$\theta_{\text{max}}@ \lambda = 96.5 \mu\text{m} [^\circ]$	150	180	180	36

Tab. 4.3.: Use of the cameras in real-time holography and limitation on the off-axis angle θ_{max} .

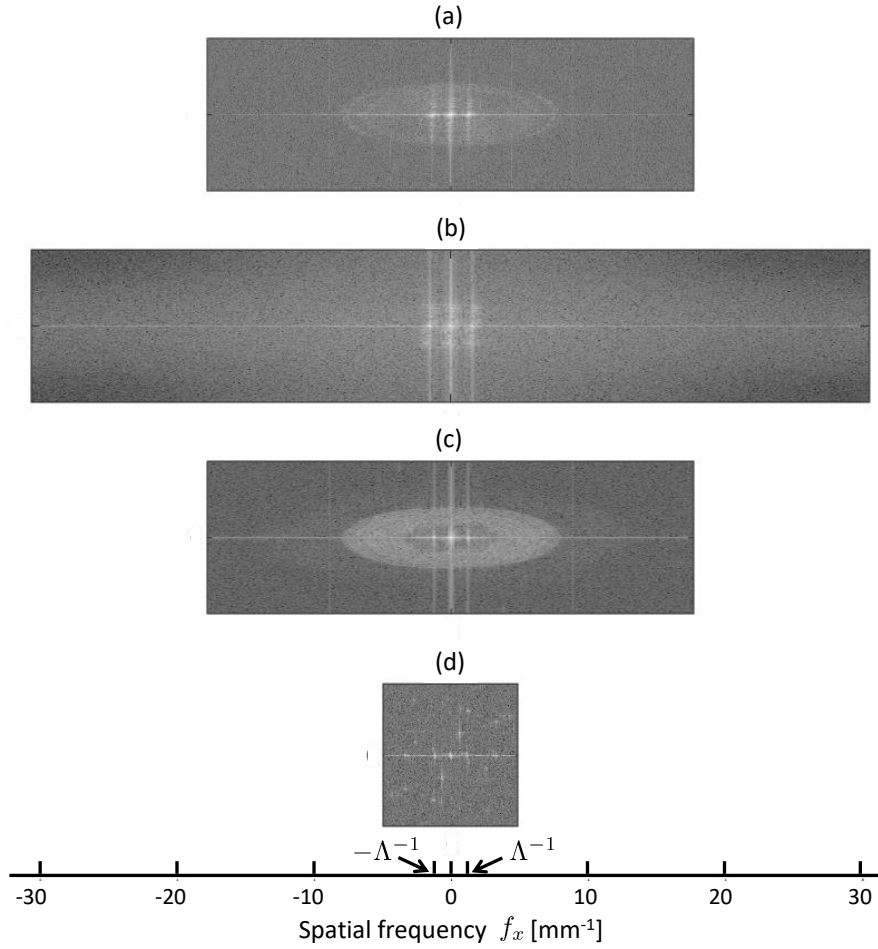


Fig. 4.6.: Fourier spectrum of the two-beam interference pattern recorded at $\lambda = 118.8 \mu\text{m}$ with (a) Cam1; (b) Cam2; (c) Cam3; (d) Cam4. Λ^{-1} denotes the carrier frequency. The spectra (a)-(c) are clipped in the f_y direction. Intensities are plotted on a logarithmic scale. Adapted from [Hack et al., 2016].

When either the pixel pitch or the pixel size δ_x satisfies the relation $4\delta_x < \lambda$, θ is unrestricted, and therefore the carrier frequency can be maximized by setting $\theta = 180^\circ$. In real experiments, however, using large angles may not be recommended or feasible due to excessive diffraction or obstruction from the housing.

Figure 4.6 shows, on a logarithmic scale, the squared modulus of the Fourier Transform (Fourier spectrum) of the interference fringe patterns measured at $\lambda = 118.8 \mu\text{m}$ for all cameras. Plotted along the horizontal axis is the spatial frequency along x , defined as $f_x \equiv x/(N_x \delta_x^2)$, where N_x is the number of pixels along the x -axis. For Cam1-3 the background peak at the origin and the two satellite peaks at $\pm\Lambda^{-1} \approx \pm 1.4 \text{ mm}^{-1}$ are clearly visible [Fig. 4.6(a)-(c)]. Also, the absence of higher harmonics of Λ^{-1} suggests that Cam1-3 operate in their linear regime. This can hardly be assessed for Cam4 [Fig. 4.6(d)], as the satellite peaks are more difficult to identify here. Such conclusions are reflected in the calculated SNR_{ref} (Tables 4.2 and 4.3), whose values for Cam4 are about 2 orders of magnitude lower

than for Cam1-3, as well as in the calculated D^* (Table 4.1), which for Cam4 is a factor 40 lower than for Cam1-3.

We can also observe that Cam1-3 can accommodate much higher spatial frequencies than Cam4, owing to a much smaller pixel pitch. Furthermore, the square and elliptic halos in Figs. 4.5(b) and (c) are caused by diffraction at the rectangular and circular edges of Cam2 and 3, respectively, as already realized from Fig. 4.4.

4.4 Conclusions and final remarks

In this Chapter four thermal cameras have been compared and their performance evaluated in the context of THz imaging and real-time THz off-axis digital holography. These included three uncooled micro-bolometers and one pyroelectric camera. Two micro-bolometers were specifically designed for the range of wavelengths $[8, 14] \mu\text{m}$ (LWIR-bolometers), whereas the other two cameras were dedicated for THz radiation.

The SNR measured for all three bolometers are comparable whereas the pyroelectric camera, for some applications, has a SNR more than two orders of magnitude lower when used at about 3 THz. Our experimental findings correlate with the calculated D^* , although the values for the two LWIR-bolometers were calculated from their specifications in their designated operation range in the infrared band. Nevertheless, all four cameras assessed in this work can be used for THz imaging and real-time THz holography, provided that sufficient THz power is available.

An additional aspect to consider in full-field imaging is the homogeneity of the response of the camera across its detection area. It has been shown that the response of a LWIR-bolometer was severely corrupted by uncontrollable interference effects between the detector plane and the cover window, as well as by diffraction from the camera housing. In order to suppress such artifacts, additional measurements, e.g. with and without samples or at partially overlapping camera positions, can be used. This may limit, however, the possibility to image dynamic scenes.

Unfortunately, the dedicated THz cameras do not yet reach the performance of the LWIR-bolometers, in terms of number of pixels or SNR .

Based on these considerations, for the experiments presented in the next Chapters, Cam2 has been used, featuring:

- High SNR for both beam profiling and off-axis digital holography experiments;
- Moderate inhomogeneities across its detection area, which can be efficiently suppressed by combining several images taken in different experimental conditions;
- The smallest pixel pitch, enabling the use of large off-axis angles, which are an essential requirement for reliable off-axis digital holography reconstructions.

An example of THz off-axis holographic reconstructions, performed with partially overlapping camera images, will be reported in the next Chapter.

Synthetic aperture THz off-axis digital holography

The topic of this Chapter is the reconstruction of an object replicating the structure of human skin. In order to allow its successful reconstruction, we are going to introduce and implement a resolution enhancement technique in a THz off-axis digital holography setup.

5.1 Description of the problem

The resolution limit of off-axis digital holography in the Fresnel diffraction regime expressed by Eq. (2.30) was derived for a point object centered with the detection plane [Picart and Leval, 2008]. However, when an extended object should be reconstructed, the same lateral resolution cannot be reached across the whole object plane, owing to the following reasons, which are illustrated in Fig. 5.1(a).

1. The peripheral regions of the object [shadowed in yellow in Fig. 5.1(a)] will be reconstructed with worse lateral resolution than its central ones, as the wavefront diffracted by them is only partially recorded.
2. Wavefronts diffracted by regions of the object lying outside of the reconstructed region will also be recorded [shadowed in purple in Fig. 5.1(a)], and will wrongly contribute to the reconstruction.

Both these complications arise from the fact that the size of the illuminated object is larger than the camera detection area, and thus they can be overcome by increasing the latter quantity relative to the former.

This Chapter introduces a resolution enhancement technique, known as *synthetic aperture acquisition*, to alleviate these issues. It is based on synthetically increasing the detection area by stitching diffraction patterns collected while stepping the detector to shifted positions across its plane.

5.2 Methods

The holographic acquisition proceeds as outlined in section 2.3.1, by recording the superposition $\Psi(\mathbf{x})$ of the wavefront $O(\mathbf{x})$ diffracted by the object and the off-axis reference beam $R(\mathbf{x})$ at the detection plane, placed at an average distance d from the object [Fig. 5.1(b)]. We record a set of holograms $\Psi_j(\mathbf{x})$, $j = 1, \dots, J$, while stepping the camera across the \mathbf{x} -plane. Each hologram can thus be written as,

$$\Psi_j(\mathbf{x}) = [R(\mathbf{x}) + O(\mathbf{x})] \mathbf{1}_j(\mathbf{x}), \quad (5.1)$$

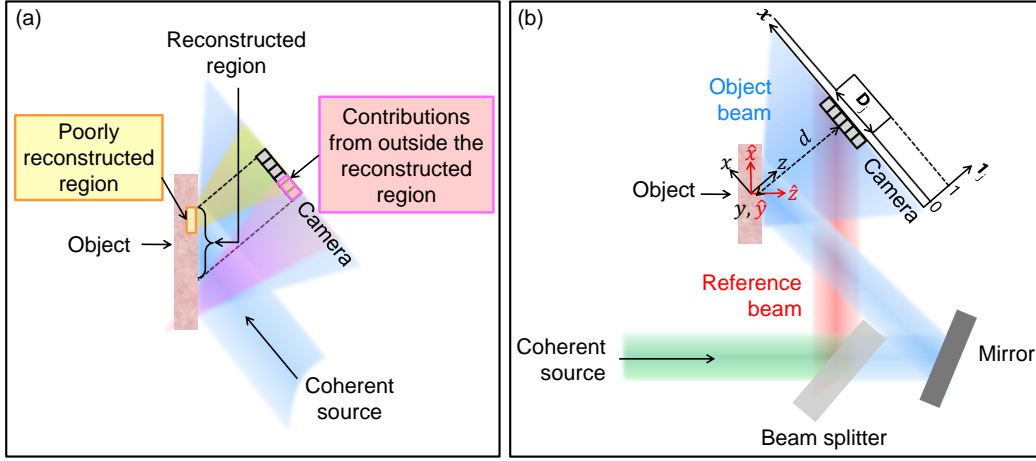


Fig. 5.1.: (a) Complications arising when reconstructing an object with a size comparable to that of the detector. The wavefront diffracted by the outermost regions of the object is shaded in yellow and is recorded at the top of the detector plane, while the wavefront diffracted from outside the reconstructed region is shaded in purple and is recorded at the bottom of the camera. (b) Schematic of the off-axis digital holography setup with synthetic aperture acquisition in reflection. The object coordinate system $(\hat{x}, \hat{y}, \hat{z})$ is rotated with respect to the camera coordinate system (x, y, z) . The average object-camera distance is indicated with d . The function $\mathbf{1}_j$ restricts the detection area to the region \mathbf{D}_j at each position of the camera.

where $\mathbf{1}_j(\mathbf{x})$ is the indicator function evaluating to 1 in the camera detection area \mathbf{D}_j and 0 elsewhere:

$$\mathbf{1}_j(\mathbf{x}) \equiv \begin{cases} 1 & \text{if } \mathbf{x} \in \mathbf{D}_j \\ 0 & \text{elsewhere.} \end{cases} \quad (5.2)$$

Each hologram is individually processed as detailed in section 2.3.1, so that J complex object beam distributions $O_j(\mathbf{x}) \equiv A_{O_j}(\mathbf{x}) \exp[i\phi_{O_j}(\mathbf{x})]$ are retrieved at the detection plane. All their amplitudes and all their phases are then stitched together, yielding the object beam distribution across the whole spanned area on the detection plane, $O(\mathbf{x}) = A_O(\mathbf{x}) \exp[i\phi_O(\mathbf{x})]$, via the stitching operator \mathcal{S} defined in Appendix C:

$$A_O(\mathbf{x}) = \mathcal{S}_{j=1}^J [A_{O_j}(\mathbf{x})]; \quad (5.3a)$$

$$\phi_O(\mathbf{x}) = \mathcal{S}_{j=1}^J [\phi_{O_j}(\mathbf{x})]. \quad (5.3b)$$

Once the stitched object beam distribution has been obtained at the detection plane, the reconstruction of the object is performed via back-propagation by the distance d :

$$o(\mathbf{x}) = O(\mathbf{x}) * h_{-d}(\mathbf{x}). \quad (5.4)$$

Finally, because the object is not parallel to the detection plane, a rotational transformation is required to bring the reconstructed wavefront to the coordinate system of

the object $(\hat{x}, \hat{y}, \hat{z})$ [see Fig. 5.1(b) again]. On the plane $(\hat{x}, \hat{y}, 0)$, shortly denoted with (\hat{x}, \hat{y}) , the reconstructed object $\hat{o}(\hat{x}, \hat{y})$ is calculated as follows:

$$\hat{o}(\hat{x}, \hat{y}) = \mathcal{R}_{\Theta}[o](\hat{x}, \hat{y}), \quad (5.5)$$

where the rotation operator \mathcal{R}_{Θ} is defined in Appendix D.

5.3 Experiments

We implemented the THz off-axis digital holographic setup shown in Fig. 5.1(b). The THz source consisted of the FIRL 100 gas laser described in section 3.3.1, operated at the wavelength $\lambda = 96.5 \mu\text{m}$. In order to assess the capability of our technique to resolve the microscopic ripple structure of human skin, a convex fingertip imprint produced on wax [Fig. 5.2(a)] was used. The holograms were recorded with the Gobi-640-GigE microbolometer camera, featuring 480×640 pixels on a $17 \mu\text{m}$ pitch and described in the previous Chapter. Overall, 42 holograms were recorded on a rectangular grid with steps of $\Delta x = 1 \text{ mm}$ and $\Delta y = 2 \text{ mm}$ along the x - and y -axes, respectively, thus synthetically increasing the detection area by a factor of about 3.5. To remove the incoherent infrared background emitted by the environment at room temperature, a dark frame taken by blocking the THz beam with a shutter was subtracted from each hologram.

5.4 Results and discussion

The amplitude and the phase of the reconstructed object beam $\hat{o}(\hat{x}, \hat{y})$ are shown in Figs. 5.2(d) and (e), respectively. While the ripple structure of the object is apparent from the reconstructed amplitude, a correct interpretation of the reconstructed phase is less straightforward. We recall that the phase difference between each pair of reconstructed points arises from the difference between the optical paths traveled by the wavefronts reflected at the two points. In our 45° -geometry, the phase difference $\Delta\phi$ experienced by two wavefronts reflected at two points on the object surface with a height difference of t is $\Delta\phi = 2\sqrt{2}\pi t/\lambda$, which implies a height difference of about $69 \mu\text{m}$ per 2π phase cycle at $\lambda = 96.5 \mu\text{m}$. Since the height difference between the apex and the outermost reconstructed regions is much larger than λ , the reconstructed phase in Fig. 5.2(e) wraps in several fringes with an oval shape centered at the fingertip apex. The average number of fringes, counted from the apex to the base of the object, located in the outermost reconstructed regions in Fig. 5.2(e), translates to a maximum height around $700 \mu\text{m}$, which is consistent with the value measured with a microscope within 15%. We can identify, however, more subtle reconstructed phase features by subtracting, from the reconstructed phase of Fig. 5.2(e), the oval fringes isolated with a low-pass filter. The result of this subtraction in the region of interest bounded by the black rectangle in Fig. 5.2(e),

converted into height differences and shown in Fig. 5.2(f), reveals the microscopic ripple structure of the fingertip.

In order to confirm our findings, the same object was measured through projection moiré profilometry and the results are shown in Figs. 5.2(b) and (c). Note, that a direct comparison between Figs. 5.2(b) and (e) is not appropriate, owing to the different origin of the reconstructed phase in the two techniques. Nevertheless, after subtracting the low-frequency components in the same way as done in the holographic reconstruction, a comparable height distribution is obtained [Fig. 5.2(c)].

For this object with such a complicated structure, evaluating the resolution across the reconstructed area would require too many subjective assumptions. Therefore, a quantitative estimation of the issues described in section 5.1 also goes beyond the scope of the work in this Chapter. For a systematic study on the lateral resolution of THz off-axis digital holography reconstructions with a synthetic aperture acquisition, the reader is referred to Chapter 7. However, a comparison between a region of the object reconstructed from one [Fig. 5.3(a)] and 42 stitched holograms [Fig. 5.3(b), corresponding to the region bounded by the green rectangle in Fig. 5.2(d)] makes it clear that the reconstructed ripple structure is better visible in the latter image [also see the profiles shown in Fig. 5.3(c), calculated along the red line in Fig. 5.3(a) and the green line in Fig. 5.3(b)], thus confirming the resolution enhancement achieved with the synthetic aperture approach. It is worthwhile mentioning, that such an improvement of the resolution originates from two effects. First, the numerical aperture has been increased because of the increased detection area. Second, consecutive holograms in the synthetic aperture acquisition scheme are strongly overlapping. For example, in these experiments the shifts applied to the camera between two consecutive images were always less than 25% of the size of the detector along the direction parallel to the shift. This overlap improves the reconstruction, in that it increases the signal-to-noise ratio by a factor \sqrt{N} in the regions measured N times, and allows suppressing the unwanted diffraction effects associated with optics and camera edges, which are often an issue when imaging with coherent THz radiation (see Chapter 4 and [Li et al., 2019]).

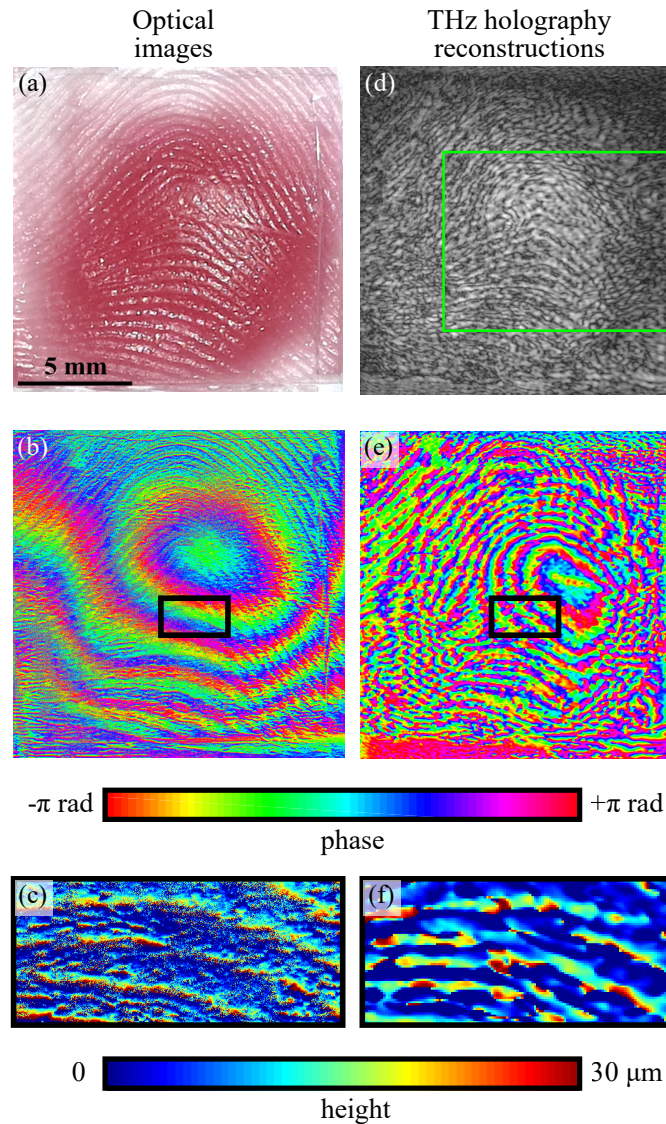


Fig. 5.2.: Comparison between optical images (left-hand side) and THz off-axis digital holography reconstructions (right-hand side) of a fingertip replica. (a) Photograph of the object. (b) Phase from projection moiré profilometry and (c) reconstructed profile of the microscopic ripple structure after filtering the low spatial frequencies in (b). (d) Amplitude and (e) phase from THz off-axis digital holography, and (f) reconstructed ripple profile. The green rectangle in (d) bounds the area shown in Fig. 5.3 (b).

5.5 Conclusions and outlook

In this Chapter, an acquisition scheme for resolution enhancement in off-axis digital holography, termed synthetic aperture acquisition, was introduced. It relies on collecting a set of holograms at partially overlapping positions across the detection plane. It was implemented for the reconstruction of a fingertip replica with THz radiation in a reflection setup. The reconstructed height distribution of the object was confirmed by independent measurements performed with projection moiré

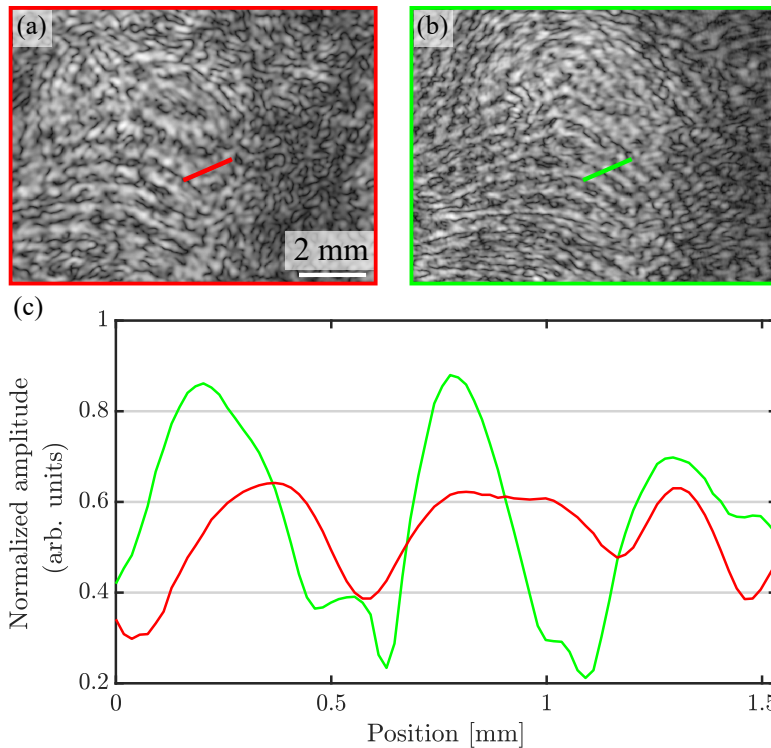


Fig. 5.3.: Comparison between the reconstructed amplitude of a region of the fingertip replica obtained from (a) one and (b) 42 partially overlapping holograms. Profiles along the red and green line in (a) and (b), respectively, are shown in (c) with the corresponding colors.

profilometry. A comparison with a reconstruction obtained with only one hologram demonstrated the benefits of the synthetic aperture approach, which are explained by higher numerical aperture and signal-to-noise ratio.

We should however note that the use of the THz off-axis digital holography setup discussed in this Chapter is limited by some practical requirements. First, the reference beam must not interact with the object, thus a lower limit is set to the recording distance and consequently to the attainable resolution given by Eq. (2.30). Although a compensation for this resolution loss can be obtained by increasing the numerical aperture with the described synthetic aperture approach, two limitations remain:

1. Because the beam always illuminates the same area of the object, the current approach can only be used with objects smaller than the beam size;
2. The synthetic aperture approach is effective only if the camera is moved to regions where the interference between the object beam and the reference beam can be reliably recorded.

In principle, both issues can be solved by scanning the object while, at each position of the object, adjusting the reference beam so to optimize the interference pattern

and recording holograms at different camera shifts. However, this would represent a cumbersome solution.

Therefore, in the next Chapter we will implement a new THz imaging setup, whose simple acquisition procedure allows lifting these limitations.

THz ptychography

In this Chapter, the first experimental demonstration of ptychographic imaging with a coherent THz source is reported [Valzania et al., 2018b], thus extending the range of coherent and lensless THz imaging techniques. Reconstructions of an amplitude and a phase object will be discussed, achieving sub-mm lateral resolution and μm -scale depth resolution.

6.1 Experiments

The experimental setup, described in detail in section 2.4, is sketched in Fig. 6.1 with one of the two objects used in this study. The FIRL 100 gas laser was used as THz source at the wavelength $\lambda = 96.5\ \mu\text{m}$, corresponding to a frequency of 3.1 THz. The output power was several tens of mW. The probe was defined by cropping the THz beam with a circular aperture with a diameter of 3 mm before it impinged on the sample. Pure amplitude and phase objects were imaged. The former was a 100 μm -thick metallic 9-spoked Siemens Star with an inner diameter of 4 mm [see Figs. 6.1 and 6.2(a1)]. The latter was a 2 mm-thick polypropylene (PP) slab where three intersecting rings of 2.1-mm outer diameter, 1.5-mm inner diameter and depths ranging from 37 to 234 μm were engraved by laser ablation [see Fig. 6.2(a2), where the wrapped phase map simulated at $\lambda = 96.5\ \mu\text{m}$ and assuming a refractive index of PP $n_{PP} = 1.51$ [Jin et al., 2006] is color coded]. Diffraction patterns were acquired with the Gobi-640-GigE camera. The incoherent infrared radiation from the environment at room temperature was subtracted by chopping the incident THz beam.

6.2 Results and discussion

Figures 6.2(a1)-(k1) summarize the experiment on the amplitude object. Because the object is totally reflective in its metallic regions and totally transparent in its holes, the validity of the multiplicative approximation [Eq. (2.32)] is trivial. The object was scanned across a square grid of 7×7 points with a spacing of 0.75 mm, resulting in a relative overlap parameter of 75%, when approximating the beam diameter with the aperture diameter [Bunk et al., 2008]. The diffraction pattern of the aperture without object was also recorded, in order to ease the estimation of the probe function and of the distance from the aperture to the camera. The latter was estimated by fitting a simulated diffraction pattern of a circular aperture to the experimental one. In a similar way, the distance from the aperture to the object and from the object to the camera was estimated by comparing experimental diffraction patterns and simulated ones at different distances and choosing the

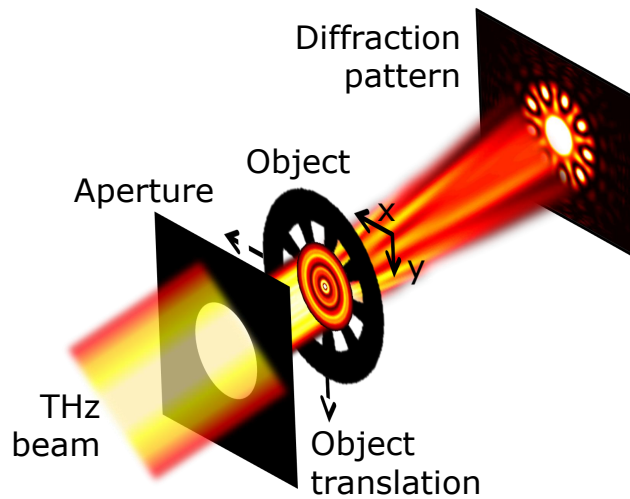


Fig. 6.1.: Schematic experimental setup for transmission ptychography. Adapted from [Valzania et al., 2018b].

values minimizing their difference for each diffraction pattern. Their average and standard deviation define the distance and its accuracy, respectively. We obtained an average object-camera distance of 12.2(7) mm and an aperture-object distance of 3.8(7) mm (standard deviations are given in parentheses in units of the least significant digits). Although such a method is self-consistent, it is indeed prone to large variations, especially when comparing strongly diffracted patterns like Figs. 6.2(d1), (e1). While using a ruler is definitely a simpler and possibly more accurate method, this is not always feasible. In fact, the detection plane of our camera is not directly accessible, as it is hidden behind a cover plate at a distance which must be estimated through indirect methods.

Figures 6.2(b1)-(g1) compare simulated and experimental diffraction patterns at the camera plane when the probe illuminated the three positions highlighted in Fig. 6.2(a1). Experimental patterns were denoised by setting to zero the pixel values below a threshold, determined by a statistical calculation performed in regions with low signal [Wang et al., 2017]. Ptychographic reconstructions, shown in Figs. 6.2(h1)-(k1), were performed with the ePIE algorithm described in section 2.4.1, initialized by a constant value in both amplitude and phase as the first estimate of the object and updated with $\alpha^{(o)} = 0.1$ [Eq. (2.36b)]. Simulated reconstructions [amplitude in Fig. 6.2(h1) and phase in Fig. 6.2(j1)] were obtained after 100 iterations. The probe, shown in the nearby insets (amplitude in the top left inset image, phase in the bottom left inset image), was the diffraction pattern of a 3-mm aperture calculated at the aperture-object distance of 3.8 mm, and it was not updated during the reconstruction process [$\alpha^{(p)} = 0$ in Eq. (2.36b)]. Reconstructions from real data were performed with 200 iterations. The reconstruction of the probe was initialized with the probe used in the simulation and updated with $\alpha^{(p)} = 0.1$ starting

from the 11th iteration. At the end of the last iteration, the metric E [Eq. (2.37)] always differed by less than 1% from the value calculated at the previous iteration.

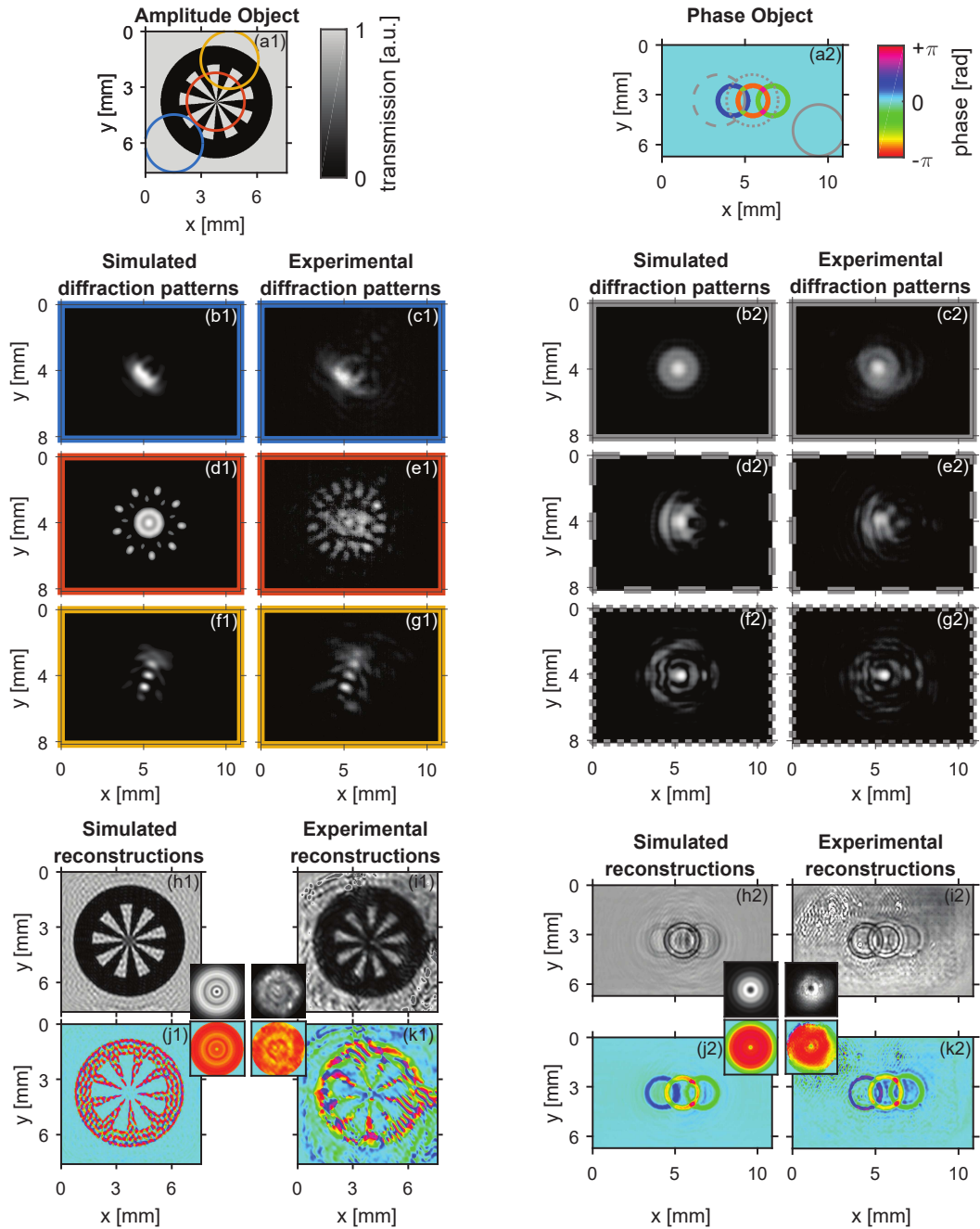


Fig. 6.2.: Ptychographic reconstruction of an amplitude object (label 1) and a phase object (label 2). (a) Simulated object transmission function, with three positions of the probe from the scan. Corresponding diffraction patterns obtained from the (b), (d), (f) simulated and (c), (e), (g) real object. (h) Amplitude and (j) phase of the simulated reconstructions. (i) Amplitude and (k) phase of the experimental reconstructions. Insets show the probe (top: amplitude, bottom: phase; left: simulation, right: experiment). All phase distributions share the same phase scale, shown in (a2). Adapted from [Valzania et al., 2018b].

Figures 6.2(i1), (k1) and the corresponding insets show the reconstructions of the amplitude object and the probe. Here, the reconstructed phase is not meaningful in regions where the amplitude of the transmitted beam is lower than the noise level, and it is distributed according to a uniform rectangular distribution in the range $[-\pi, \pi)$ rad.

For both simulated and experimental reconstructions, the lateral resolution was calculated by averaging the squared amplitude along concentric circles of decreasing radius and evaluating the signal modulation at each step (modulation transfer function [Boreman, 2001]). It was estimated with the inverse of the spatial frequency at which the signal modulation falls below the noise-equivalent modulation. The noise-equivalent modulation was chosen in such a way that the obtained resolution is the same as half the width, calculated at its first zero, of the reconstruction of an on-axis point object. We obtained lateral resolutions of $140 \mu\text{m}$ (1.5λ) and $230 \mu\text{m}$ (2.4λ), i.e. 21 and 13 times smaller than the beam diameter, for simulated and experimental reconstructions, respectively.

Results for the phase object are displayed in an analogous way in Figs. 6.2(a2)-(k2). Owing to the low diffraction and absorption of the object (absorption coefficient $\alpha_{PP}(3.1 \text{ THz}) = 1.5 \text{ cm}^{-1}$ [Lee, 2009]), diffraction patterns in Figs. 6.2(b2)-(g2) are shown with a logarithmic scale. The object was moved across a two-dimensional, rectangular grid of 21×7 points with steps of 0.4 mm and 0.6 mm, resulting in relative overlaps of 87% and 80% along x and y respectively, ensuring a correct reconstruction of all its features. In order to account for refraction through the PP slab, diffraction patterns were also measured in a region far from the three rings [Fig. 6.2(c2)]. This allows us to reconstruct an object whose thickness is the maximum ring depth and not the physical thickness of the slab. Because the maximum ring depth satisfies the condition from Eq. (2.31), the multiplicative approximation is valid in this case too. The object was at 9.6(6) mm from the camera and 12.0(6) mm from the aperture. At the following [link](#)[†] an excerpt from the experimental reconstruction of the phase object has been made available. One can see that acceptable lateral and phase resolutions are obtained already after 5 iterations of the ePIE algorithm. A drop of the laser power by a factor ~ 2 towards the end of the scan caused higher noise at the top left corner of the reconstructed phase and amplitude. In this case the lateral resolution was calculated from the 10% - 90% width of the experimentally reconstructed phase edges of the rings. A conservative estimate amounts to $170 \mu\text{m}$ (1.8λ). The results of the three rings and the regions where they cross are summarized in Table 6.1. The depth t of the rings was measured with an optical microscope (2nd column in Table 6.1), translated into phase differences $\Delta\phi$ at the THz wavelength of $\lambda = 96.5 \mu\text{m}$ through the refractive index of PP according to $\Delta\phi = 2\pi(n_{PP} - 1)t/\lambda$ (3rd column), and compared to experimental and simulated ptychographic reconstructions (4th and 5th column,

[†]https://figshare.com/articles/_/5630380

Region	Depth [μm]	THz phase from optical measurements [rad]	THz phase from ptychography	
			Experiment [rad]	Simulation [rad]
Left ring	157(3)	5.2(1)	4.7(2)	5.2(2)
Crossing left/middle ring	234(3)	7.8(1)	7.8(2)	8.1(1)
Middle ring	77(3)	2.6(1)	2.4(3)	2.4(2)
Crossing middle/right ring	117(3)	3.9(1)	3.8(3)	3.7(1)
Right ring	37(3)	1.2(1)	1.2(1)	1.2(1)

Tab. 6.1.: Depth and reconstructed phase of the phase object measured with an optical microscope (2nd and 3rd columns respectively) and measured with THz ptychography (4th column). The reconstructed phase of the simulated object is given in the 5th column. Standard deviations are given in parentheses in units of the least significant digits.

respectively). The same approach was used in [Hack and Zolliker, 2014] to evaluate the reconstruction performance of THz off-axis digital holography. Note, that *a priori* knowledge on the profile of the object is required to determine the number and sign of 2π -multiples to be added at each phase jump and thus retrieve the absolute phase of the object from its phase reconstruction.

For this phase object, we estimate the phase resolution with the standard deviation of the reconstructed phase inside the left and right rings, far more than one lateral resolution from the ring edges, where it is supposed to be uniform. A phase resolution of $\rho_\phi = 0.1$ rad and 0.06 rad was estimated for experimental and simulated reconstructions, respectively. Finally, we define the depth resolution ρ_d as the smallest depth difference which can be inferred from the reconstructed object phase when the refractive index is constant, namely $\rho_d = \lambda\rho_\phi/[2\pi(n_{PP} - 1)]$. Accordingly, we estimate $\rho_d = 3\mu\text{m}$ ($\approx \lambda/32$) and $1.8\mu\text{m}$ ($\approx \lambda/54$) in PP at $\lambda = 96.5\mu\text{m}$ from experimental and simulated data, respectively.

6.3 Conclusions and outlook

In this Chapter we have shown that ptychography can be performed with THz radiation. It allows reconstructing amplitude and phase objects with $\approx 200\mu\text{m}$ ($\approx 2\lambda$) lateral resolution and μm -scale depth resolutions ($\approx \lambda/30$) at $\lambda \approx 96.5\mu\text{m}$. Note, that comparable performances were obtained with synthetic aperture THz off-axis digital holography in Chapter 5, thus making THz ptychography a promising alternative to THz digital holography. Further studies, quantitatively comparing their resolution limits, will be performed in the next Chapter.

Resolution limits of THz ptychography and THz off-axis digital holography

Following the demonstration of THz ptychographic imaging reported in the previous Chapter, here we will study its resolution limits and how they compare to those of THz off-axis digital holography, used in Chapter 5. The factors impacting the lateral resolution will be investigated on a pure amplitude object with both simulations (section 7.1) and experiments (section 7.2). The reconstruction of a weakly diffracting pure phase object, exhibiting features at the resolution limit for THz imaging techniques, will lead to an estimation of the depth resolution (section 7.2). Finally, section 7.3 summarizes the results and discusses the applicability of THz ptychography as an alternative to THz off-axis digital holography.

7.1 Simulations

The binary amplitude mask used in the previous Chapter, namely the nine-spoked Siemens Star with an inner diameter of 4 mm shown in Fig. 6.2(a1), was simulated and reconstructed at different THz wavelengths, object-camera distances, and camera array sizes. The simulation values reflect parameters of typical THz imaging experiments. The wavelengths correspond to two of the most intense emission lines delivered by CO₂-laser-pumped methanol lines in far-infrared gas lasers [Douglas, 2013], namely $\lambda = 96.5 \mu\text{m}$ and $\lambda = 118.8 \mu\text{m}$. The object-camera distance d varied from 1 to 31 mm, and cameras featuring $N_x \times N_y = 640 \times 480$ pixels on pixel pitches of $\delta_x = \delta_y = 17 \mu\text{m}$ and $25 \mu\text{m}$ are considered, according to the specifications of two popular microbolometer arrays which proved to image THz radiation, and whose performance was reported in Chapter 4.

For each combination of these values, three reconstruction techniques were applied. The first approach, referred to as the “Forth-and-back propagation” method, consisted of propagating a plane wave normally impinging on the object to the camera plane, cropping the complex field distribution according to the camera size, convolving it with the pixel pitch, and back-propagating it to the object plane. Because the phase of the object beam is calculated at the camera plane, this approach does not replicate a phase retrieval experiment. However, it proves useful to separate the *intrinsic* factors impacting the lateral resolution, namely those ultimately determining the best achievable lateral resolution, from the *extrinsic* ones, that is, the factors depending on the specific imaging technique used to solve the phase problem. The second approach, referred to as the “FFT holography” method, re-

produced a THz off-axis digital holography experiment. The hologram obtained from the superposition of the field transmitted through the object and a tilted plane reference wave was simulated. The angle between the propagation directions of the object beam and the reference beam was set to 45° . The phase of the object beam at the camera plane was retrieved from the cropped and re-sampled interference pattern with a Fourier Transform method (section 2.3.1). Finally, the retrieved object wave was back-propagated to the object plane. The third approach (“Ptychography”) reproduced a THz ptychography experiment. A collimated flat-top beam with a diameter of 3 mm impinged on the object, which was moved across a square grid of 7×7 points with steps of 0.75 mm, resulting in a relative overlap of 75%, as defined in [Bunk et al., 2008]. The simulated and cropped ptychograms, re-sampled according to the camera pixel pitch, were used in an ePIE algorithm without probe updating [$\alpha^{(p)} = 0$ in Eq. (2.36b)] with 5 iterations and $\alpha^{(o)} = 0.1$ [Eq. (2.36a)].

For each reconstruction, the lateral resolution was calculated in the same way as in the previous Chapter, namely by evaluating the modulation of the intensity of the reconstructed wave at the object plane along concentric rings with decreasing radii, where the noise-equivalent modulation was determined from the reconstruction of a point object as explained in section 6.2.

Figure 7.1 shows the calculated lateral resolution ρ , normalized to the wavelength, as a function of $d/(N\delta_x) = 1/\tan \theta$, where θ is half the acceptance angle of an equivalent, square camera with $N^2 \equiv N_x N_y$ pixels seen by an on-axis point a distance d apart. Each point represents the average resolution obtained at the two wavelengths $\lambda = 96.5 \mu\text{m}$ and $\lambda = 118.8 \mu\text{m}$ and at the two pixel pitches $\delta_x = \delta_y = 17 \mu\text{m}$ and $25 \mu\text{m}$. The different reconstruction approaches are encoded with different marker types (\circ for “Forth-and-back propagation”, \bullet for “FFT holography”, and \times for “Ptychography”). One can observe that the simulated results can be approximated by the following resolution function, plotted with a solid line:

$$\frac{\rho}{\lambda} = \frac{1}{2 \sin \theta} = \frac{1}{2} \sqrt{1 + \left(\frac{2d}{N \delta_x} \right)^2} \quad (7.1)$$

and corresponding to the diffraction limit $\rho/\lambda = (2NA)^{-1}$, with a numerical aperture $NA \equiv \sin \theta$ set by the acceptance angle of the camera. Therefore λ and NA are regarded as the intrinsic resolution factors. This suggests that ptychography and digital holography share the same intrinsic lateral resolution factors. The presence of some points around $d/(N\delta_x) = 0.5$ lying below the resolution function is caused by the fact that at those distances the wavefront diffracted by the object can be fully recorded by the detector, thus mimicking a NA close to unity and independent of the detector size. We ascribe any difference among the resolutions of the three methods to different extrinsic resolution factors. For the “FFT holography” method, these include residual errors in the elimination of the carrier fringes, and in the optimization of the window used to isolate the first diffraction order from the

DC component [Kreis, 2006]. For the “Ptychography” method, we mention the influence of the overlap parameter [Bunk et al., 2008] and the number of iterations. The “Forth-and-back propagation” method displays the lowest deviation from the theoretical resolution function, because the number of extrinsic resolution factors is minimized, thanks to the known phase of the object beam at the detector plane.

As in classical imaging using a lens [Goodman, 2005], the lateral resolution cannot be pushed below Abbe’s limit $\rho \rightarrow \lambda/2$, which is reached at distances $d \ll N \delta_x$. On the other hand, at distances $d \gg N \delta_x$ (Fresnel diffraction regime), the resolution function approaches the expression derived in [Picart and Leval, 2008] for an on-axis object reconstructed with digital Fresnel holography and introduced in section 2.3.1, that is, $\rho/\lambda = d/(N \delta_x)$. As a consequence, part of the analyses in [Picart and Leval, 2008] can be migrated to ptychography. For example, ptychograms can be zero padded prior to back-propagation to the object plane, leading to a denser sampling of the resolution function.

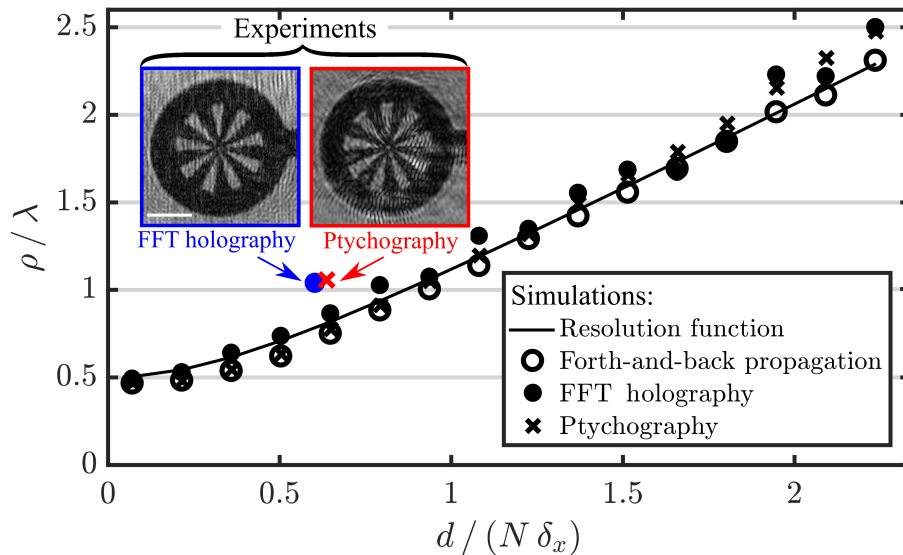


Fig. 7.1.: Lateral resolution (normalized to the wavelength) calculated for a simulated amplitude object reconstructed with the “Forth-and-back propagation” (\circ), “FFT holography” (\bullet), and “Ptychography” (\times) methods as a function of the reconstruction distance normalized to the camera size. The intrinsic resolution function from Eq. (7.1) is plotted with a solid black line. The blue filled circle and the red cross indicate the experimental resolution reached by synthetic aperture THz off-axis digital holography and THz ptychography, respectively (section 7.2). The insets show the corresponding reconstructed amplitudes. Scale bar: 2 mm. From [Valzania et al., 2018a].

7.2 Experiments

In order to experimentally verify the conclusions drawn in section 7.1, synthetic aperture THz off-axis digital holography and THz ptychography experiments were carried out on the real binary amplitude object used in the previous Chapter and simulated in section 7.1. The holograms and the ptychographic diffraction patterns

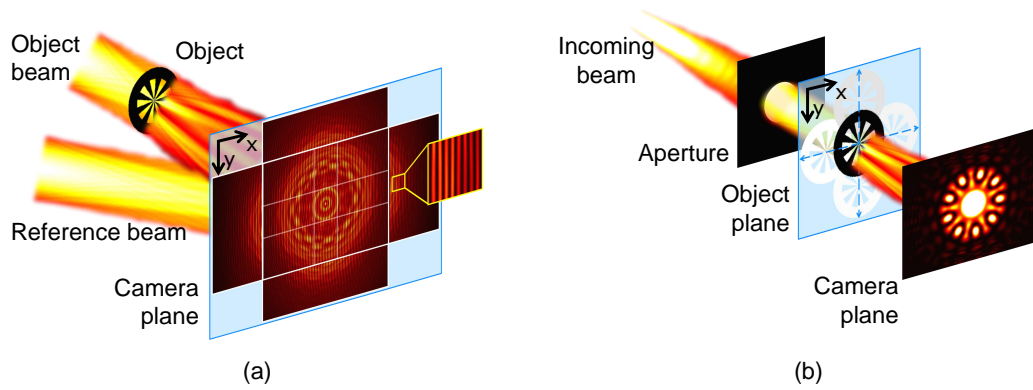


Fig. 7.2.: Schematic experimental setup of (a) synthetic aperture off-axis digital holography and (b) ptychography. Adapted from [Valzania et al., 2018a].

were recorded at the emission line $\lambda = 96.5 \mu\text{m}$ of the FIRL 100 gas laser and with the Gobi-640-GigE camera, featuring $N_x \times N_y = 640 \times 480$ pixels on a $\delta_x = \delta_y = 17 \mu\text{m}$ pitch.

In the synthetic aperture holographic experiments [Fig. 7.2(a)], holograms were acquired by shifting the camera across the camera plane as far as interference fringes could be distinguished. This was achieved by moving the camera across a 11×11 grid with steps of 1.6 mm along both x and y , thereby increasing the size of the camera array by a factor 2.5 and 3 along x and y , respectively. The camera array was placed at the minimum distance from the object that ensured no interaction between the object beam and the reference beam, that is, $d = 15.4$ mm. The phase of the object beam was retrieved with the Fourier Transform method, followed by stitching of the holograms and final back-propagation as detailed in Chapter 5. In the ptychographic experiments [Fig. 7.2(b)], an aperture with a diameter of 3 mm clipped a diverging (full divergence angle of 4.5°), lowest order transverse electro-magnetic (TEM_{00}) Gaussian laser beam at a distance of 7.3 mm from the object. The latter was placed at a distance $d = 6$ mm from the camera, which is a factor of 2.6 closer than the distance employed in the holographic experiments, resulting in a comparable NA . The ptychographic diffraction patterns were then fed in an ePIE algorithm with parameters similar to those used for the experimental reconstructions of the previous Chapter. For the sake of a fair comparison between the two imaging techniques, the same number of images was used: the object was scanned across a 11×11 grid with steps of 0.7 mm along both x and y , resulting in relative overlaps of 77%. Furthermore, identical integration time and procedure for the correction of the incoherent infrared background were employed, while the average THz power incident on the object plane differed by less than 10%.

The amplitudes of the object beam reconstructed with off-axis digital holography and ptychography are shown in the top left inset of Fig. 7.1, and the estimated lateral resolutions are plotted in colors (blue filled circle for synthetic aperture

THz off-axis digital holography, and red cross for THz ptychography). Because comparable results were achieved by the two techniques, we conclude that the larger reconstruction distance needed to perform off-axis digital holography was compensated by increasing the synthetic camera size by the same amount. This conclusion supports the trend predicted with simulations and obtained from Eq. (7.1). We ascribe the difference between the resolutions of the experiment and simulation to uncertainties in the estimation of the reconstruction distance, as well as in the knowledge of the shifts applied to the object or the camera.

The depth resolution was experimentally estimated from a similar type of comparison, performed on a pure phase object with shallow depth features. This was a 4 mm-thick Teflon slab where 9 squares with a side of 3 mm each and depths ranging from 11 to 473 μm were engraved by laser ablation. In order to provide reference values, its profile was measured with projection moiré profilometry. The wrapped phase of holographic and ptychographic reconstructions is displayed in the insets (a) and (b) of Fig. 7.3, respectively. To compensate for tilts of the object with respect to the camera plane, affecting the reconstructed phase, the average phase within each square was measured with respect to the average phase within an adjacent flat surface region. The unwrapped phases were then translated into depths according to $\Delta t = \lambda \Delta \phi / [2\pi(n_T - 1)]$, where Δt is the depth variation causing a phase difference $\Delta \phi$ in Teflon, with a refractive index n_T at the wavelength λ . For Teflon, $n_T = 1.45$ at $\lambda = 96.5 \mu\text{m}$ [Lee, 2009]. The extracted depths are plotted in Fig. 7.3 (blue filled circles for synthetic aperture THz off-axis digital holography, red crosses for THz ptychography, and black diamonds for projection moiré). Table 7.1 shows the reference depth of each square (2nd column) and the unwrapped phase reconstructed with the three methods (3rd-5th columns), in the same format used in Table 6.1. The weak diffraction from this phase object makes the first four squares hardly resolvable with both THz imaging techniques. We define two squares as resolvable, if the difference of their average phase is larger than the arithmetic average of their standard deviations. Accordingly, digital holography can resolve square 1 from square 3, while ptychography can reliably tell the depth difference of square 1 and square 4, at most. This corresponds to depth resolutions of $\approx 20 \mu\text{m}$ ($\approx \lambda/5$) and $\approx 30 \mu\text{m}$ ($\approx \lambda/3$) for THz digital holography and THz ptychography, respectively.

We would like to point out that, theoretically, any limit of the phase resolution must be ascribed to the finite signal-to-noise ratio (SNR) in the measurement data [De Ruijter and Weiss, 1993], as well as to limitations of the experimental setup. According to the definition of depth resolution ρ_d given in the previous Chapter, ρ_d can also be pushed below any arbitrary value, provided that the SNR is sufficiently increased. Note, however, that an alternative definition of depth resolution is also found in literature, and should not be confused with the one used here. This refers to the depth resolution as the size, along the optical axis, of the point-spread function,

$\rho'_d \equiv \lambda/(2NA^2)$, and it is especially used in digital holographic microscopy [Ferraro et al., 2011].

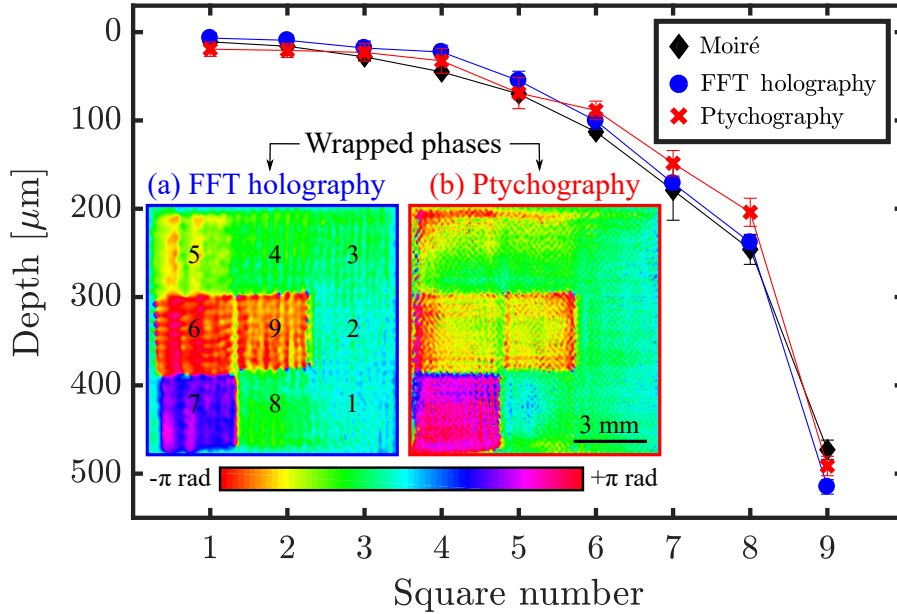


Fig. 7.3.: Reconstructed profile of a phase object consisting of 9 squares with increasing depths. Black symbols show the result of a reference measurement using projection moiré profilometry; blue [red] symbols indicate the depths retrieved by synthetic aperture THz off-axis digital holography [THz ptychography], while the corresponding reconstructed wrapped phase is shown in the inset (a) [(b)]. Wrapped phases share the same colorbar, shown at the bottom. The total length of each errorbar is twice the standard deviation of the retrieved depth within the corresponding square. From [Valzania et al., 2018a].

7.3 Conclusions and final remarks

In this Chapter, we have discussed the theoretical and experimental resolution limits of THz ptychography, and compared them to the performance of THz off-axis digital holography. Simulated reconstructions show that the two approaches share the same intrinsic resolution factors determining the lateral resolution, which is diffraction-limited. A lateral resolution $\rho \approx \lambda$ could be experimentally reached with both techniques, 20% higher than the diffraction limit because of inaccuracies in the knowledge of geometric acquisition parameters. In the holographic measurement this was achieved by a synthetic aperture approach, which compensated the long object-camera distance needed to couple the off-axis reference beam. In ptychography, a shorter recording distance could be afforded, because an off-axis reference beam is not required. It should also be noted that values of ρ/λ on the order of 1 are obtainable thanks to the strong diffraction properties of THz radiation for this type of sample structures. This in turn allows recording diffraction patterns with a much higher NA compared to X-ray diffraction-based imaging techniques [Holler et al.,

Square no.	Depth [μm]	THz phase from projection moiré [rad]	THz phase from THz imaging	
			FFT holography [rad]	Ptychography [rad]
1	11(4)	0.3(1)	0.2(2)	0.6(2)
2	16(3)	0.5(1)	0.3(2)	0.6(2)
3	28(4)	0.8(1)	0.5(2)	0.7(3)
4	45(3)	1.3(1)	0.7(2)	0.9(4)
5	70(4)	2.0(1)	1.6(3)	2.0(5)
6	113(4)	3.3(1)	2.9(3)	2.6(3)
7	179(34)	5.2(10)	5.0(2)	4.3(4)
8	246(17)	7.1(5)	6.9(2)	5.9(5)
9	473(11)	13.7(3)	14.9(2)	14.2(3)

Tab. 7.1.: Depth and reconstructed phase of the phase object measured with projection moiré profilometry (2nd and 3rd columns respectively) and phase reconstructed with THz off-axis digital holography (4th column) and THz ptychography (5th column). Standard deviations are given in parentheses in units of the least significant digits.

2017]. Also, the relatively long THz wavelength makes experimental requirements less stringent, allowing close access to the theoretical resolution limits.

Furthermore, depth variations as low as $\approx \lambda/3$ could be distinguished in a flat and weakly diffracting phase object.

As anticipated in section 5.5, the ptychographic setup lifts some crucial limitations of off-axis digital holography, namely:

1. The reconstructed region is not limited by the beam size, because the object is scanned across the beam;
2. Since a reference beam is not required, the recording distance can be shortened, thereby increasing the numerical aperture and, consequently, improving the lateral resolution beyond what can be achieved with synthetic aperture schemes, where the size of the reference beam is a limiting factor.

On the other hand digital holography, being a non-iterative solution to the phase problem, is computationally less complex than ptychography. In conclusion, we can confirm that THz ptychography is a valid alternative to THz digital holography for imaging objects with sub-mm lateral resolution and a depth resolution approaching the μm range. The choice of one or the other must be taken depending on external constraints, such as the size of the object and the affordable computational complexity.

Coherent reconstruction of an object hidden behind a THz-transparent material through THz off-axis digital holography

This Chapter focuses on the development of a holographic technique for imaging an object hidden behind a transparent cover in reflection with THz radiation. After introducing the problem in section 8.1, an imaging technique based on a three-beam interference model is presented with simulated data (section 8.2) and experimental confirmation (section 8.3) by reconstructing an amplitude object behind a Teflon plate. Its advantages compared to previous methods and its applicability will be outlined in section 8.5, before a summary in section 8.6 ends the Chapter.

8.1 Description of the problem

The problem entails imaging an object hidden behind a transparent and weakly diffracting cover, using the diffraction patterns of the combined system “hidden object + cover” and *a priori* information on the cover. Based on the comparison between off-axis digital holography and ptychography presented in the previous Chapters, we opt for the former approach, because we limit our analysis to hidden objects with a size of a few mm, which can be imaged with a full-field technique avoiding scanning. Therefore, here we extend the imaging procedure developed in Chapter 5, used for the reconstruction of a fingertip replica in reflection, to a case where the incoming radiation illuminates two objects stacked behind each other [Fig 8.1(a)]. Let the coordinate system be such that the detector plane defines the xy -plane, shortly denoted as \mathbf{x} , and let the wavevectors of all beams mostly lie in the xz -plane. The cover is assumed to be weakly diffracting, meaning reflecting and refracting a fraction of the incoming beam without affecting its spatial profile. If we further assume that a plane wave impinges on the cover before interacting with the object, the overall intensity measured at the camera plane can be written as the following three-beam interference:

$$I_{ROT}(\mathbf{x}) \equiv |R(\mathbf{x}) + O(\mathbf{x}) + T(\mathbf{x})|^2, \quad (8.1)$$

where $U(\mathbf{x}) = A_U(\mathbf{x}) \exp[i\phi_U(\mathbf{x})]$, $U \in \{R, O, T\}$, are the complex amplitudes, described by the real amplitudes $A_U(\mathbf{x})$ and phases $\phi_U(\mathbf{x})$, of the reference beam, the beam diffracted from the object, and the contribution from the cover material, respectively, with “T” standing for “Teflon”, since a Teflon plate was used in the

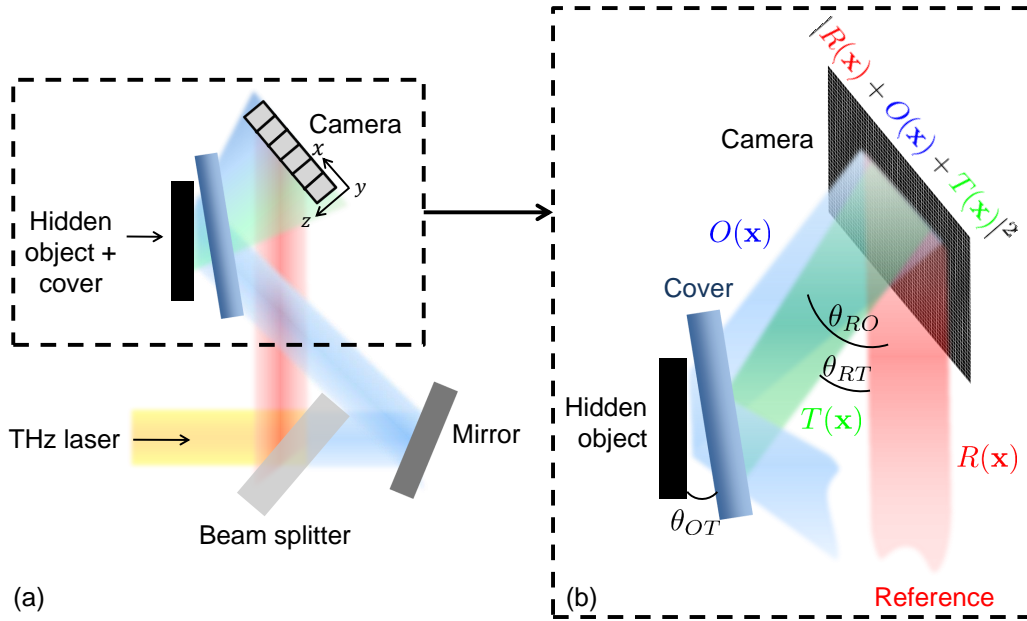


Fig. 8.1.: (a) Schematic of an off-axis digital holographic setup in reflection with two samples stacked behind each other. (b) Insight into the three-beam interference arising from diffraction from the object and reflection from the cover. See the main text for an explanation of the symbols. Adapted from [Valzania et al., 2017b].

experiments described in section 8.3. Note that, for the sake of brevity, here we use a slightly different notation than in section 2.3.1, where $\phi_U(\mathbf{x})$ used to denote the phases observed in a plane perpendicular to the average wavevector of the wavefront.

Equation 8.1 can be expressed as a function of the real amplitudes and phases in the following form:

$$I_{ROT}(\mathbf{x}) \equiv A_R^2(\mathbf{x}) + A_O^2(\mathbf{x}) + A_T^2(\mathbf{x}) + 2A_R(\mathbf{x})A_O(\mathbf{x}) \cos[\phi_R(\mathbf{x}) - \phi_O(\mathbf{x})] + 2A_R(\mathbf{x})A_T(\mathbf{x}) \cos[\phi_R(\mathbf{x}) - \phi_T(\mathbf{x})] + 2A_O(\mathbf{x})A_T(\mathbf{x}) \cos[\phi_O(\mathbf{x}) - \phi_T(\mathbf{x})]. \quad (8.2)$$

The meaning of the terms contained in Eq. (8.2) is clarified with simulations of three-beam interference patterns. A 9-spoked reflective Siemens Star [Fig. 8.2(a)], making an angle of 45° with the camera plane, was used as the hidden object. The reference beam [Fig. 8.2(b)] was approximated by a wave with a Gaussian intensity distribution and flat phase front. A set of Gaussian beamlets with random phases and exponential distribution of intensities, on top of a larger Gaussian distribution, was chosen as a reflected beam $T(\mathbf{x})$, in order to simulate random reflections hindering the reconstruction of the hidden object. The parameters used in the simulations reproduced those from a typical experiment (see section 8.3). The angle θ_{OT} between the hidden object and the cover [Fig 8.1(b)] was set to 0° without loss of generality. The three complex fields were propagated through the propagation kernel of Eq.

(2.14), rotated to the camera plane as described in Chapter 5 and Appendix D, and finally summed. The squared modulus of the sum yields the interference pattern I_{ROT} of Eq. (8.2) and it is shown in Fig. 8.2(d).

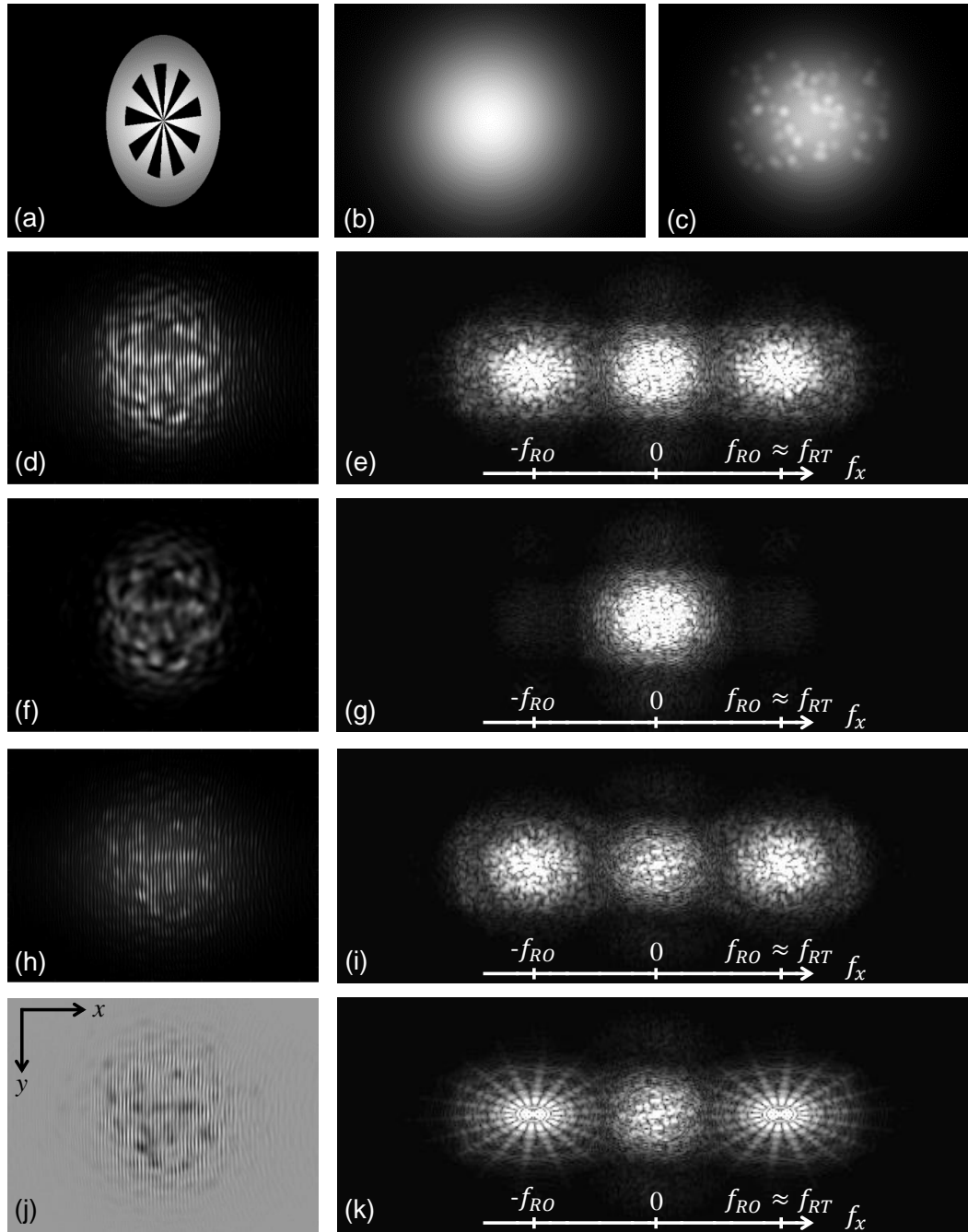


Fig. 8.2.: Simulation results. Amplitude distribution of (a) the hidden object, (b) the reference beam, and (c) the beam $T(\mathbf{x})$. Their interference pattern $I_{ROT}(\mathbf{x})$ is shown in (d), along with the modulus of its Fourier Transform in (e). (f) Interference pattern $I_{OT}(\mathbf{x})$ and (g) modulus of its Fourier Transform. (h) Interference pattern $I_{RT}(\mathbf{x})$ and (i) modulus of its Fourier Transform. (j) Intensity distribution of the subtraction performed to retrieve the hidden object and (k) modulus of its Fourier Transform. All the spectra are displayed on a common logarithmic scale. Adapted from [Valzania et al., 2017b].

The problem is an extension of the tilted-beam interference model from two to three interfering beams. While the former version, discussed in section 2.3.1, is easily solved modulating the object beam at a large enough carrier frequency to allow the separation of the diffraction orders, applying the same method to the latter case is more challenging. The Fourier Transform of $I_{ROT}(\mathbf{x})$, whose modulus is plotted in Fig. 8.1(e), contains contributions:

1. Around the spatial frequency $\mathbf{f} \equiv (f_x, f_y) = (0, 0)$, due to the terms $A_R^2(\mathbf{x})$, $A_O^2(\mathbf{x})$ and $A_T^2(\mathbf{x})$;
2. Around the spatial frequency $\mathbf{f} = (\pm f_{RO}, 0)$, with $f_{RO} \equiv \sin(\theta_{RO})/\lambda$ being the carrier frequency set by the average angle θ_{RO} between the propagation directions of $R(\mathbf{x})$ and that of $O(\mathbf{x})$, and where λ is the wavelength;
3. Around the spatial frequency $\mathbf{f} = (\pm f_{RT}, 0)$, with $f_{RT} \equiv \sin(\theta_{RT})/\lambda$ being the carrier frequency set by the average angle θ_{RT} between the propagation directions of $R(\mathbf{x})$ and that of $T(\mathbf{x})$;
4. Around the spatial frequency $\mathbf{f} = (\pm f_{OT}, 0)$, with $f_{OT} \equiv \sin(\theta_{OT})/\lambda$ being the carrier frequency set by the average angle θ_{OT} between the propagation directions of $O(\mathbf{x})$ and that of $T(\mathbf{x})$ which, in a reflection setup, corresponds to the average angle between the hidden object and the cover.

To reconstruct the hidden object, the beam diffracted from it needs to be separated from the one reflected from the cover. Because both beams are modulated by the tilted reference beam to the same spectral region, separating them via a filtering operation in the spatial frequency domain is not feasible. In other words, if we denote the Fourier bandwidth of $O(\mathbf{x})$ with B_O , then we have $|f_{RO} - f_{RT}| < B_O$.

The same problem has been encountered in several applications of optical interferometry, especially in mechanical engineering [Rastogi and Hack, 2012]. For example, in order to simultaneously measure the multidimensional deformation components of an object, an approach consists of illuminating it with multiple object beams, and recording their interference with a reference beam. Methods have been proposed to achieve signal separation from a multiple-beam digital holographic setup with multiple illuminating object beams and a single reference beam [Rajshekhar et al., 2012; Kulkarni and Rastogi, 2014b; Kulkarni and Rastogi, 2014a; Kulkarni and Rastogi, 2015b; Rajshekhar et al., 2011; Kulkarni and Rastogi, 2015a]. In [Rajshekhar et al., 2011], a spatial carrier in one of the object beams was introduced. In [Rajshekhar et al., 2012], an alternative approach based on a piecewise multicomponent polynomial phase formulation was presented, thus avoiding the need for a spatial carrier. Kulkarni et al. [Kulkarni and Rastogi, 2015a] proposed an iterative procedure which consists of dividing the interference field in blocks where the phase has a simple form and applying an augmented matrix based reconstruction to each block. However, most of these methods exploit the fact that the intensity as well as the propagation direction of the two object beams can be independently controlled in the experimental setup. This is not feasible

in our case, since the multiple object beams come from the cover and the hidden object, and the ratio of their intensities as well as their phases is governed by their structural and optical properties like the absorption coefficient and the refractive index. Therefore, separation approaches based on phase shifting of the interfering beams fail, as well.

Furthermore, when testing the surface flatness of transparent plates with interferometric methods, three-beam interferences are measured between a reference beam and two object beams coming from the front surface and the tilted back surface of the plate. In order to unwrap the three-beam interferogram, Sunderland et al. [Sunderland et al., 2014; Sunderland and Patorski, 2015] subtracted a two-beam interferogram obtained by blocking the reference beam from the three-beam interferogram in a Twyman-Green or in a Fizeau setup. Finally, they used continuous wavelet and pseudo-Wigner-Hough transforms to separate the phase distributions at the front and back surfaces.

8.2 Method

Here, similarly to the method reported in [Sunderland et al., 2014; Sunderland and Patorski, 2015], the three interfering beams are reconstructed with difference measurements, however using three interference patterns instead of two. With our experimental setup, we can record the following interference patterns besides I_{ROT} :

$$I_{OT} \equiv A_O^2(\mathbf{x}) + A_T^2(\mathbf{x}) + 2A_O(\mathbf{x})A_T(\mathbf{x}) \cos[\phi_O(\mathbf{x}) - \phi_T(\mathbf{x})], \quad (8.3)$$

$$I_{RT} \equiv A_R^2(\mathbf{x}) + A_T^2(\mathbf{x}) + 2A_R(\mathbf{x})A_T(\mathbf{x}) \cos[\phi_R(\mathbf{x}) - \phi_T(\mathbf{x})], \quad (8.4)$$

where I_{OT} [shown in Fig. 8.2(f), along with the modulus of its Fourier Transform in Fig. 8.2(g)] is obtained by blocking the reference beam, while I_{RT} [shown in Fig. 8.2(h), along with the modulus of its Fourier Transform in Fig. 8.2(i)] is obtained by removing the object and measuring the beam reflected from the cover, superimposed with the reference beam. We now notice that

$$I_{ROT}(\mathbf{x}) - I_{RT}(\mathbf{x}) - I_{OT}(\mathbf{x}) = -A_T^2(\mathbf{x}) + 2A_R(\mathbf{x})A_O(\mathbf{x}) \cos[\phi_R(\mathbf{x}) - \phi_O(\mathbf{x})], \quad (8.5)$$

namely the subtraction of the two-beam interference patterns from the three-beam interference pattern leaves only the beam $O(\mathbf{x})$ modulated at the spatial frequency f_{RO} , as displayed in Fig. 8.2(j) and in the modulus of its Fourier Transform in Fig. 8.2(k).

At this stage, $O(\mathbf{x})$ can be extracted as explained in section 2.3.1, as long as f_{RO} is large enough to allow its separation from the Fourier Transform of $A_T^2(\mathbf{x})$ centered at the origin of the spatial frequency space. It should be noted, however, that this condition is usually met for $\lambda \approx 0.1$ mm, $\theta_{RO} \approx 45^\circ$ and upon illuminating a weakly diffracting object with a plane wave. Therefore $A_R(\mathbf{x})A_O(\mathbf{x})$ and $\phi_R(\mathbf{x}) - \phi_O(\mathbf{x})$

are obtained from Eq. (8.5) with the Fourier Transform method. Analogously, $A_R(\mathbf{x})A_T(\mathbf{x})$ and $\phi_R(\mathbf{x}) - \phi_T(\mathbf{x})$ are obtained using Eq. (8.4). Subtracting the fringe pattern $2A_R(\mathbf{x})A_T(\mathbf{x})\cos[\phi_R(\mathbf{x}) - \phi_T(\mathbf{x})]$ from $I_{RT}(\mathbf{x})$ yields $A_R^2(\mathbf{x}) + A_T^2(\mathbf{x})$. Once the sum and the product of $A_R^2(\mathbf{x})$ and $A_T^2(\mathbf{x})$ are known, $A_R(\mathbf{x})$ and $A_T(\mathbf{x})$ can be separated. Finally, this allows extracting $A_O(\mathbf{x})$ from $A_R(\mathbf{x})$ and the product $A_O(\mathbf{x})A_R(\mathbf{x})$. Since $\phi_R(\mathbf{x})$ varies linearly across the camera plane, $\phi_O(\mathbf{x})$ can be obtained from the phase difference $\phi_R(\mathbf{x}) - \phi_O(\mathbf{x})$ by subtracting a phase ramp. Alternatively, $\phi_R(\mathbf{x})$ can be directly measured from the off-axis hologram of a mirror in place of the hidden object. Although not strictly necessary, further measurements can be taken to confirm the retrieved amplitudes. For example, $A_R(\mathbf{x})$ can be directly measured by blocking the beam before it interacts with the cover and the hidden object. Similarly, $A_T(\mathbf{x})$ can be measured after blocking the reference beam in the setup used to record $I_{RT}(\mathbf{x})$.

The amplitude and the phase of the complex field $O(\mathbf{x})$ at the camera plane are shown in Figs. 8.3(a) and (b), respectively. The corresponding amplitude and phase back-propagated by the object-camera distance are displayed in Figs. 8.3(c) and (d), respectively. The reconstructed phase distribution is flat where the object is present, because the object is flat. On the background, where the amplitude is within the noise level, the phase has been thresholded with an amplitude-based criterion and set to a constant value to improve the visibility of the reconstruction.

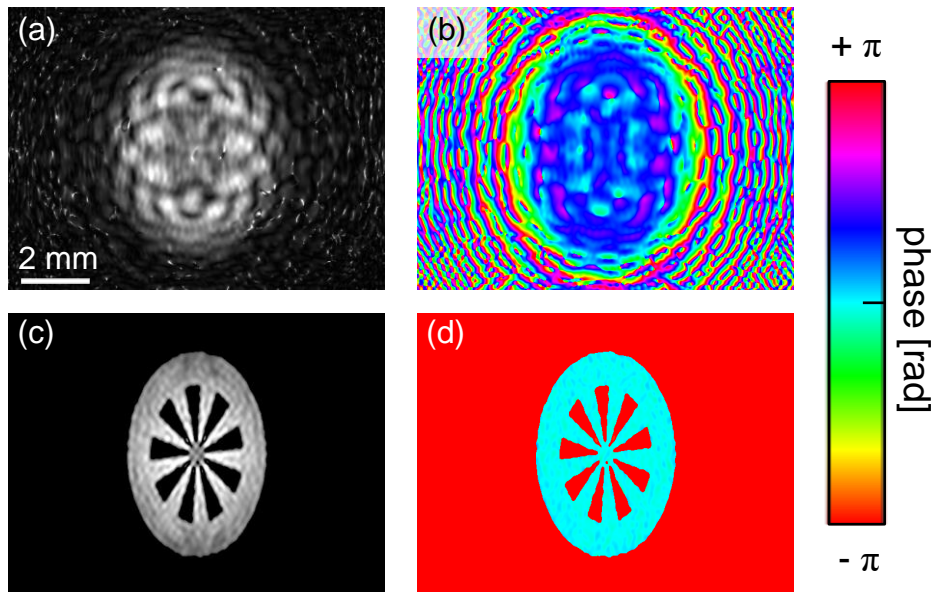


Fig. 8.3: Simulation results. (a) Retrieved amplitude and (b) phase distributions of the hidden object at the camera plane. (c) Reconstructed amplitude and (d) phase distributions after back-propagation to the position of the object. Adapted from [Valzania et al., 2017b].

8.3 Experiment

The experimental demonstration of the proposed method was provided using a THz off-axis digital holography setup like the one in Fig. 8.1(a). The THz source was the FIRL 100 gas laser operated at $\lambda = 96.5 \mu\text{m}$. A quartz beam splitter with about 70% power transmission coefficient was used to provide the reference beam, while a metal mirror directed the beam towards the stacked objects. The hidden object was the 100 μm -thick metallic 9-spoked Siemens Star with an inner diameter of 4 mm, placed about 17 mm and at an angle of about 45° from the camera plane. The cover was a 2 mm-thick Teflon plate, which is known to be highly transparent and weakly diffracting in the low THz range [Lee, 2009] and which was placed at a distance of about 2 mm from the hidden object. Reflecting part of the incident beam from its front and back surfaces, it provided the beam $T(\mathbf{x})$. As in the experiments described in the previous Chapters, each interference pattern, recorded with the Gobi-640-GigE camera, was the difference of averaging 20 images with the shutter open and 20 images with the shutter closed, so to subtract the incoherent background radiation emitted by the surrounding scene at room temperature.

8.4 Results

The experimental interference patterns $I_{ROT}(\mathbf{x})$, $I_{OT}(\mathbf{x})$ and $I_{RT}(\mathbf{x})$, are shown in the top row of Fig. 8.4. The oblique modulation observed in Figs. 8.4(a), (b) is caused by a non-zero angle θ_{OT} between the object and the cover. Besides displaying the modulation due to the interference between $A_R(\mathbf{x})$ and $A_T(\mathbf{x})$, the experimental pattern $I_{RT}(\mathbf{x})$ [Fig. 8.4(c)] also features interference effects along the rim caused by multiple reflections of the reference beam from the rectangular camera housing. Furthermore, our 45° -geometry implies that all the experimental images are less resolved on their left-hand side, where the object and the cover were farther from the camera.

Simulations of the experiment using the three-beam interference model are shown in the bottom row of Fig. 8.4. The parameters reproducing the experimental diffraction patterns best were: a propagation distance of 17.7 mm; interference angles of $\theta_{RO,xz} = 48^\circ$ and $\theta_{RO,yz} = 4^\circ$ on the xz - and yz -plane, respectively; an angle of $\theta_{OT,xz} \approx \theta_{OT,yz} \approx 7^\circ$. These values, especially $\theta_{OT,xz}$ and $\theta_{OT,yz}$, should be understood as effective parameters, since the Teflon plate had an undetermined curvature, and its orientation cannot be only described with two angles with respect to the surface of the hidden object. The modulation in the experimental pattern $I_{OT}(\mathbf{x})$ was best reproduced with a simulated amplitude ratio $A_T(\mathbf{x})/A_O(\mathbf{x})$, averaged over all the pixels, of about 0.5. It must be noted that this result is consistent with our 45° -acquisition, our experimental setup and the properties of our samples, namely: the Teflon plate had a thickness of 2 mm, a refractive index of 1.45 and an absorption coefficient of 2 cm^{-1} at 3 THz [Lee, 2009]; 80% of the total area of

the hidden object was 100% reflecting, because it was made of metal; the incident radiation was linearly polarized along the y -axis (s -polarization).

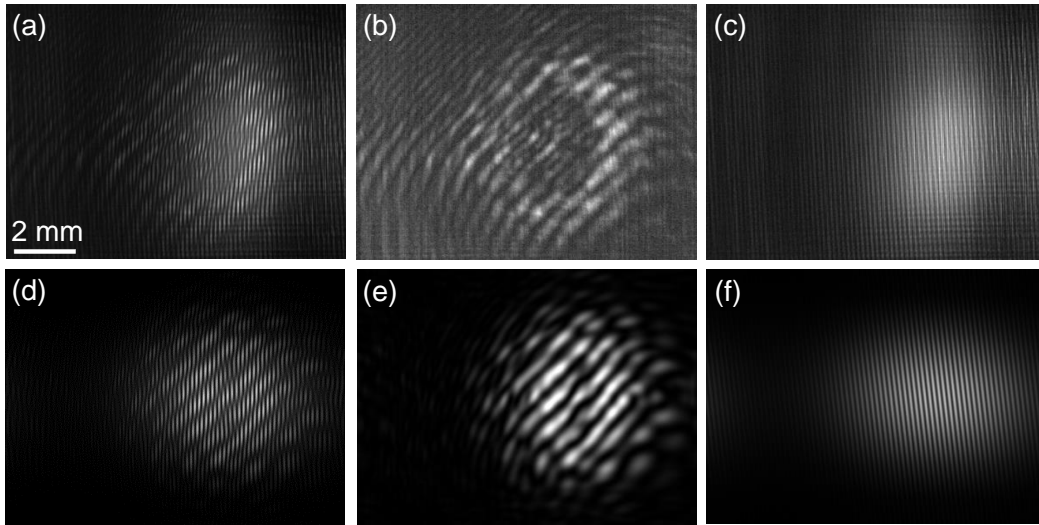


Fig. 8.4.: Top row, experimental interference patterns: (a) $I_{ROT}(\mathbf{x})$, (b) $I_{OT}(\mathbf{x})$, (c) $I_{RT}(\mathbf{x})$. Bottom row, corresponding simulated patterns: (d) $I_{ROT}(\mathbf{x})$, (e) $I_{OT}(\mathbf{x})$, (f) $I_{RT}(\mathbf{x})$. Adapted from [Valzania et al., 2017b].

The reconstructed amplitude and phase, after back-propagation and rotation of $O(\mathbf{x})$ to the object plane as performed in Chapter 5, are shown in the first and second row of Fig. 8.5, respectively. In the reference reconstructions shown in Figs. 8.5(a), (b) the object was not hidden, and it was reconstructed with a standard Fourier transform method. The wavy features observed in some spokes of the object are likely caused by spurious waves diffracted to the camera from the surroundings. The same reconstruction approach, however with the object hidden behind the Teflon plate, leads to the reconstructions shown in Figs. 8.5(g), (h). As expected, neglecting the reflections from the cover leaves the oblique modulation already noticed in the patterns $I_{ROT}(\mathbf{x})$ and $I_{OT}(\mathbf{x})$ [Figs. 8.4(a) and (b), respectively], and severely compromises the reconstruction of the hidden object.

After application of the proposed method, an improved reconstruction is obtained. The oblique interference effects due to the cover are reduced and the hidden object can be clearly seen in Figs. 8.5(d), (e). The reconstruction distance was optimized to obtain sharp edges. For the reconstructions in Figs. 8.5(a), (b), an object-camera distance of 17.7 mm was used. Although it was not changed when placing the Teflon plate, optimization led to an effective optical distance of 16.7 mm in the case of Figs. 8.5(d), (e). Furthermore, the image is displaced by roughly 0.5 mm along the horizontal axis upon insertion of the plate, and a shift of lesser extent along the vertical axis can also be observed [compare Figs. 8.5(a) and (d)]. We ascribe these effects to refraction through the plate, and indeed they can be quantitatively predicted based on the acquisition geometry and the properties of the

samples. All the reconstructed phases have been thresholded according to the amplitude criterion mentioned above and previously used on the simulated reconstructions of Fig. 8.3.

The phase distributions are not flat because the hidden object had a minor bending, and the wavefront impinging on the hidden object was slightly curved. After unwrapping the phase along the black lines shown in Figs. 8.5(b), (e), we could provide an estimate of a curved profile, plotted in Figs. 8.5(c), (f) for the reconstructions without and with Teflon plate, respectively (black symbols: experimental data points; red line: fit). Their parabolic fits yielded the same curvature to within 10%.

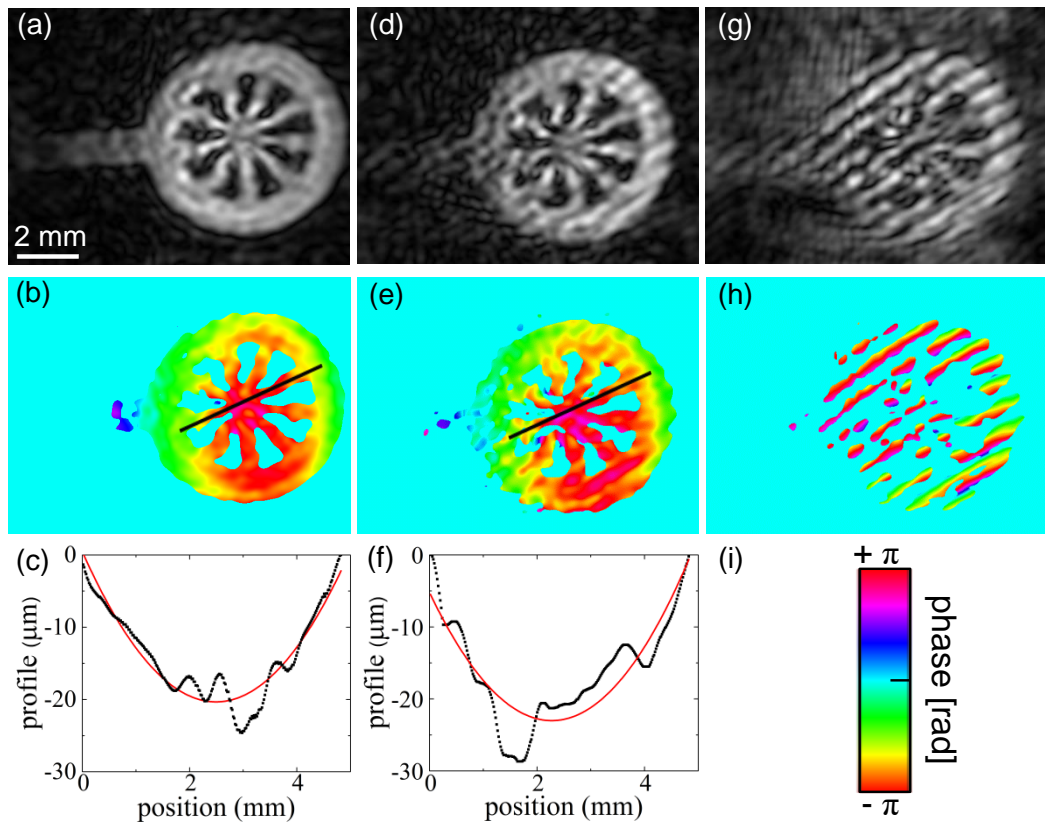


Fig. 8.5.: Experimental reconstructions of the object. Amplitudes (a), (d), (g), wrapped phases (b), (e), (h), and profiles (c), (f). (a), (b), (c): the object was not hidden; (d), (e), (f): the object was hidden behind a Teflon plate and the signal separation was applied to eliminate the contribution from the plate; (g), (h): the object was hidden behind the Teflon plate, but a standard Fourier Transform method was applied. In the plots (c) and (f), black symbols represent experimental data along the cross-sections highlighted in (b) and (e), while red lines show a parabolic fit. (i): colorbar for the wrapped phase. Adapted from [Valzania et al., 2017b].

8.5 Discussion

With the developed signal separation method, the wavefront diffracted by an object hidden behind a THz-transparent cover is reconstructed within a three-beam interference model based on difference measurements. The quality of the reconstruction is comparable with that of the same object, when it is directly seen by the camera. Although a thorough investigation of the attained resolution has not been performed, we point out that the technique is compatible with a synthetic aperture acquisition, which enables better reconstructions at the expense of an increased acquisition time.

The independent control of intensity and propagation direction of each beam, essential for unraveling three-beam interference patterns in previous methods, is not needed here. Our procedure subtracts parasitic and unwanted beams reflected once or multiple times (upon multiple internal reflections) from the surfaces of the cover, irrespective of their propagation direction and intensity relative to that of the beam diffracted by the hidden object, under the assumption that all the beams are stationary in time.

The second requirement is that the incident beam is transmitted through and reflected from the cover with negligible diffraction effects. This ensures that its Fourier bandwidth is short enough, not to overlap with the signal modulated at frequency f_{RO} in Eq. (8.5). It should also be noted, that the proposed three-beam interference model does not in general reconstruct the hidden object itself. Rather, it always recovers a wavefront having, in sequence: (i) transmitted through the cover, possibly after multiple internal reflections; (ii) interacted with the hidden object in reflection; (iii) transmitted again through the cover, possibly after multiple internal reflections. As a consequence, eventual inner or surface structures of the cover, changing the spatial distribution of the incoming plane wave after transmission through it, would degrade the reconstruction quality of the hidden object. Therefore, in its current state, the technique is applicable to objects hidden behind a stable and flat transparent cover, whose reflection properties could also be measured without hidden object at a calibration stage.

As a short note on a potential improvement of the method, we point out that comparing the reconstruction of a hidden object to that of a flat reference plate at the same location may favor its separation, extending the range of applicability to structured and even diffusing cover materials.

8.6 Conclusions

In this Chapter, a multiple-beam analysis has been developed and experimentally demonstrated, allowing the reconstruction of an object hidden behind a THz-transparent cover in the framework of THz off-axis digital holography in reflection.

Simulations and experimental results confirm the applicability of a three-beam interference model in order to explain the features observed in the experimental images. By combining three interference patterns, we have shown that the beam diffracted by the hidden object can be separated from spurious reflections caused by the cover, without *a priori* knowledge about either the intensity of the interfering beams or their interference angles. Holographic reconstructions, performed on a metallic object behind a Teflon plate, substantially improved after the application of the method, and are comparable to the reconstruction of the object when it is not hidden, thus confirming that the contributions from the cover were properly eliminated.

At the end of the Chapter, we have drawn our attention to the requirement that the cover must be weakly diffracting, which is currently limiting the applicability of the technique to simple cases. A more powerful method, reconstructing objects behind strongly diffracting covers, will be presented in the next Chapter.

Coherent reconstruction of a textile and a hidden object through a THz phase retrieval technique

In this Chapter we report a phase retrieval technique, which simultaneously reconstructs two objects, stacked one behind the other, from relative movements between them and in a transmission geometry. It is demonstrated by reconstructing a glass fabric sample and a hidden amplitude or phase object with THz radiation.

9.1 Description of the problem

Figure 9.1 shows the acquisition setup, where a coherent and collimated beam propagates through an object, represented as a nine-spoked Siemens Star. The transmitted wavefront impinges on a second object, schematically represented as a two-dimensional periodic structure, placed at a distance u from the first object and hiding it from the camera field of view. The intensity of the resultant diffraction pattern is recorded by the camera at a distance v_1 downstream of the second object. We assume that the interaction of each object with its corresponding incident wavefront can be described by the “multiplicative approximation” introduced in section 2.4.1. If a planar wavefront of unit amplitude impinges on the hidden object, the complex amplitude of the wavefront at the camera plane reads as follows:

$$\Psi(\mathbf{x}) = \{[o(\mathbf{x}) * h_u(\mathbf{x})]t(\mathbf{x})\} * h_{v_1}(\mathbf{x}). \quad (9.1)$$

Here $\mathbf{x} \equiv (x, y)$ in Fig. 9.1, and $o(\mathbf{x})$ and $t(\mathbf{x})$ are the two-dimensional, complex transmission functions of the first and second object, respectively, where t stands for “textile”, because the experiments discussed in sections 9.3 and 9.4 will deal with reconstructions behind a fabric sample. Despite that, no assumptions on the spatial distribution of the objects are made.

Although reconstructions behind textiles have already been reported, especially in the sub-THz range [Cooper et al., 2011], the effect of the textile has been neglected or simply averaged out so far. However, reconstructing both objects is crucial in order to assess their interaction, e.g. when monitoring skin healing processes behind medical gauzes [Taylor et al., 2011; Harmer et al., 2016].

Therefore, our aim is to reconstruct both $o(\mathbf{x})$ and $t(\mathbf{x})$, by translating one object across the other one by the amounts \mathbf{x}_j , $j = 1, 2, \dots, N_{xy}$ across the (x, y) plane. The obtained wavefronts at the camera plane are thus the following:

$$\Psi_j(\mathbf{x}) = \{[o(\mathbf{x}) * h_u(\mathbf{x})]t(\mathbf{x}-\mathbf{x}_j)\} * h_{v_1}(\mathbf{x}). \quad (9.2)$$

Note, that the problem is formally identical to ptychography, where in Eq. (9.2) $o(\mathbf{x}) * h_u(\mathbf{x})$ corresponds to the illumination function, and $t(\mathbf{x}-\mathbf{x}_j)$ plays the role of the shifted object transmission function. The key to the success of a ptychographic algorithm is to combine sufficient new information from the different diffraction patterns with enough redundant information in the regions of the object measured multiple times, so to allow the iterative phase retrieval. The approach implemented in Chapters 6 and 7 consisted of using an illumination function smaller than the object, translated to positions with relative linear overlaps in the range of 60-85% [Bunk et al., 2008]. An alternative implementation, termed *near-field ptychography* [Stockmar et al., 2013], employs an illumination function larger than the object and structured on a length scale comparable with the diffraction fringes cast at the camera plane. Although the latter implementation requires fewer diffraction patterns to scan the object, the diffuser used to structure the wavefront incident onto the object must be carefully chosen, as a wrong choice may prevent the algorithm from converging. In the current formulation described by Eq. (9.2), whether the first or second mentioned case applies depends on the transmission properties of the unknown object $o(\mathbf{x})$.

To bypass these complications, we implemented an alternative reconstruction technique, which is detailed in the next section.

9.2 Methods

Our reconstruction technique relies on two steps.

1. *Reconstruction of the complex wavefronts exiting the cover object.*

These correspond to the quantity $\psi_j(\mathbf{x}) \equiv [o(\mathbf{x}) * h_u(\mathbf{x})]t(\mathbf{x}-\mathbf{x}_j)$ and, by analogy with ptychography, we denote them with the term “exit waves”. Their reconstruction will be accomplished using a set of N_z diffracted intensities along the z -axis taken at the distances v_k , $k = 1, 2, \dots, N_z$, from the second object, following the SBMIR procedure from section 2.5. Despite it was originally demonstrated with visible radiation, migrating the SBMIR algorithm to the THz regime involves no fundamental changes. However, as already pointed out for THz ptychography in section 2.4.1, Fresnel numbers on the order of ~ 10 can be achieved using THz radiation, which makes the far-field approximation not applicable. This also has an impact on the choice of the recording distances v_k . The reader interested in the optimum acquisition parameters in SBMIR

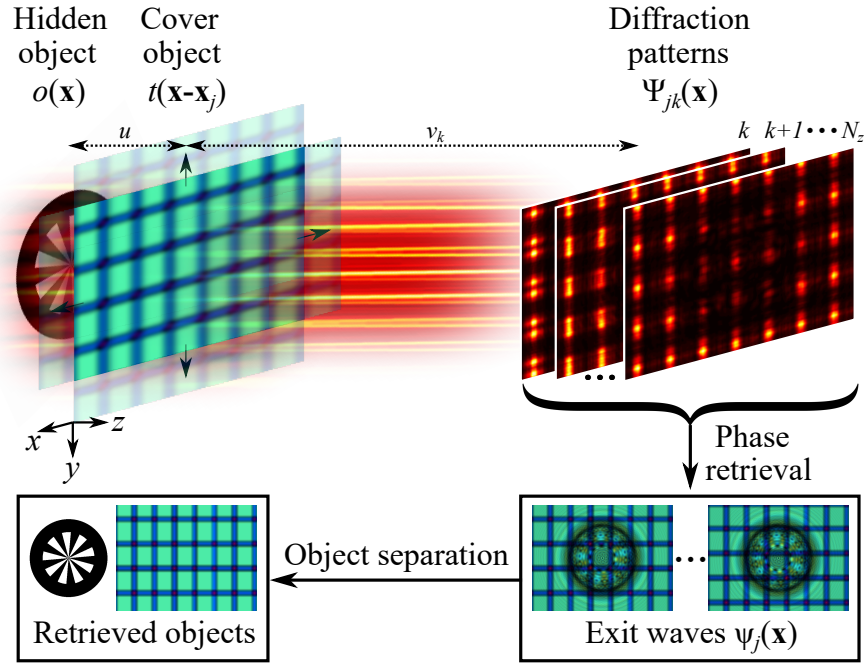


Fig. 9.1.: Setup and summary of the implemented reconstruction technique. A collimated laser beam impinges from the left on a hidden object (here a Siemens Star) and a cover object (here a schematic textile) at the distance u and with transmission functions $o(\mathbf{x})$ and $t(\mathbf{x})$, respectively. The intensity of the complex wavefield $\Psi_{jk}(\mathbf{x})$ is recorded with a camera at multiple distances v_k from the cover object. This stack of diffraction patterns allows reconstructing the complex wavefields exiting the cover object $\psi_j(\mathbf{x})$. By shifting the cover object by the amounts \mathbf{x}_j , the two transmission functions are retrieved. From [Valzania et al., 2019].

reconstructions as well as in the attainable lateral resolution is referred to Appendix E.

2. *Separation of the transmission functions of the two objects from their relative translations.*

The stitching algorithm detailed in Appendix C and used to synthetically increase the detection area (Chapter 5) will be applied in order to reconstruct the individual transmission functions $o(\mathbf{x})$ and $t(\mathbf{x})$ from the knowledge of their product and the applied shifts, as explained in the next subsection.

Thus the complete dataset is written as,

$$\Psi_{jk}(\mathbf{x}) = \{[o(\mathbf{x}) * h_u(\mathbf{x})]t(\mathbf{x}-\mathbf{x}_j)\} * h_{v_k}(\mathbf{x}) \equiv \psi_j(\mathbf{x}) * h_{v_k}(\mathbf{x}). \quad (9.3)$$

9.2.1 Separation of the transmission functions of the two objects from their relative translations

We can regard the set of measurements from Eq. (9.2) as a synthetic aperture experiment, where $t(\mathbf{x})$ is acquired under N_{xy} viewing angles and is probed by N_{xy} strongly diffracted illumination functions, represented by the object function $o(\mathbf{x})$

propagated to $z = u$ and translated by the amounts \mathbf{x}_j . Properly choosing the values of \mathbf{x}_j and N_{xy} allows the diffraction fringes of the illumination function to be washed out upon averaging in the regions illuminated multiple times, mimicking a slowly-varying wavefront probing $t(\mathbf{x})$ and thus enabling its reconstruction. Therefore, our estimates of the amplitude and the phase of $t(\mathbf{x})$ are obtained by stitching the amplitude and phase of all the $\psi_j(\mathbf{x})$, respectively, after compensating for their shifts:

$$|t(\mathbf{x})| \approx \mathcal{S}_{j=1}^{N_{xy}} [|\psi_j(\mathbf{x} + \mathbf{x}_j)|] \quad (9.4a)$$

$$\phi_t(\mathbf{x}) \approx \mathcal{S}_{j=1}^{N_{xy}} [\phi_{\psi_j}(\mathbf{x} + \mathbf{x}_j)], \quad (9.4b)$$

where $\phi_t(\mathbf{x})$ and $\phi_{\psi_j}(\mathbf{x})$ are the phase of $t(\mathbf{x})$ and $\psi_j(\mathbf{x})$, respectively, and $\mathcal{S}_{j=1}^{N_{xy}}$ is the stitching operator defined in Appendix C. It is noteworthy that shifts between adjacent images on the order of the wavelength λ are enough to average out the finest diffraction fringes cast by the first object onto the second one. Consequently, a large overlap among consecutive images is maintained. As already noted in off-axis digital holography with a synthetic aperture acquisition (Chapter 5), taking partially overlapping images increases the signal-to-noise ratio by the factor $\sqrt{N_{xy}}$ in the pixels measured N_{xy} times, and reduces the diffraction effects contributed by optics and camera edges.

The final step consists of retrieving the transmission function of the hidden object from Eq. (9.2) as follows,

$$o(\mathbf{x}) = \left\langle \frac{\psi_j(\mathbf{x})}{t(\mathbf{x} - \mathbf{x}_j)} \right\rangle_j * h_{-u}(\mathbf{x}), \quad (9.5)$$

where $\langle \rangle_j$ stands for the average over all the configurations with different positions of the second object. Although not strictly necessary, the average operation helps mitigate the poor conditioning of Eq. (9.5), as well as errors in the estimation of the shifts \mathbf{x}_j .

9.3 Experiments

We demonstrated our proposed procedure by reconstructing a pure amplitude and a pure phase object hidden behind a textile and illuminated with THz radiation. As a THz source, the FIRL 100 gas laser was used, operating at $\lambda = 96.5 \mu\text{m}$ (3.1 THz). The objects were the same which were imaged in [Valzania et al., 2018b] and in Chapter 6, namely the 9-spoked Siemens Star and the polypropylene (PP) slab with three intersecting rings engraved with different depths. The former is shown in Fig. 9.2(a1), while Fig. 9.2(a2) displays the wrapped phase map of the latter, simulated with $\lambda = 96.5 \mu\text{m}$ and with a refractive index $n_{PP} = 1.51$ [Jin et al., 2006], from the nominal depths given in Table 6.1 (note that in these experiments the phase object was rotated 90° counterclockwise around the z -axis with respect to the orientation

at which it was measured in Chapter 6). The textile was a 0.2 mm-thick glass fabric sample with plain weave pattern, 8 warp ends per cm and 6.5 warp picks per cm (available from Suter Kunststoffe AG, Fraubrunnen, Switzerland). The diffraction patterns from the combined system “hidden object+cover object” were recorded using the Gobi-640-GigE uncooled microbolometer camera, containing 480×640 pixels on a pixel pitch of $17 \mu\text{m}$, and the subtraction of a dark frame was performed to suppress the incoherent infrared background. For the reconstruction of both hidden objects, $N_z = 5$ diffraction patterns were acquired by stepping the camera along the z -axis with shifts $\Delta z = 1 \text{ mm}$. These were employed in a SBMIR algorithm, started with a flat distribution in both amplitude and phase as initial solution and further improved with 200 iterations. At each camera position, diffraction patterns were acquired while moving the textile on the (x, y) plane across a two-dimensional square grid of $N_{xy} = 20 \times 20 = 400$ points with steps of $76 \mu\text{m}$ ($\approx 0.8\lambda$).

9.4 Results

The hidden amplitude object and the textile, reconstructed after the separation procedure, are shown in Figs. 9.2(b1) and (c1), respectively. We estimated the best reconstruction distances u and v_1 by optimizing the lateral resolution of the reconstructed amplitude object, as displayed in Fig. 9.3. Here the presence of several good reconstruction distances around (u, v_1) coordinates satisfying $u + v_1 \approx 8.6 \text{ mm}$ is caused by both the intrinsic depth of focus of the imaging system, and by the thickness of the textile, which was neglected as a consequence of the multiplicative approximation. The amplitude object was reconstructed at $u = 3.1 \text{ mm}$ and $v_1 = 5.5 \text{ mm}$ (indicated with a red star in Fig. 9.3). At these distances, the lateral resolution was around $140 \mu\text{m}$ ($\approx 1.5\lambda$), which agrees well with the resolution of a corresponding *unhidden* simulated object, reconstructed with the SBMIR algorithm and with the same reconstruction parameters as in our experiments (see Appendix E). Figure 9.4 shows reconstructions using 22 (left), 50 (middle) and 100 (right) exit waves, which were randomly chosen from the 400 exit waves used for the reconstructions of Fig. 9.2. With $N_{xy} = 100$ exit waves, the lateral resolution is around $170 \mu\text{m}$ ($\approx 1.8\lambda$).

When the hidden object is smaller than the cover, the outermost regions of the diffraction patterns only bear information on the shifted $t(\mathbf{x}-\mathbf{x}_j)$. Therefore, cross-correlating neighboring intensities allows us to extract the positions \mathbf{x}_j , thus obviating the need for their *a priori* knowledge. Figures 9.2(d1), (e1) show the objects reconstructed after retrieving the $N_{xy} = 400$ positions of the textile. Overall, an average error of about $50 \mu\text{m}$ was made in the estimation of each *absolute* position \mathbf{x}_j .

Nevertheless, knowing the shifts is not necessary in order to reconstruct the hidden object. If we perform the stitching described in Eqs. (9.4) with vanishing shifts, i.e. $\mathbf{x}_j = 0, \forall j \in [1, N_{xy}]$, the amplitude and phase modulations imposed by

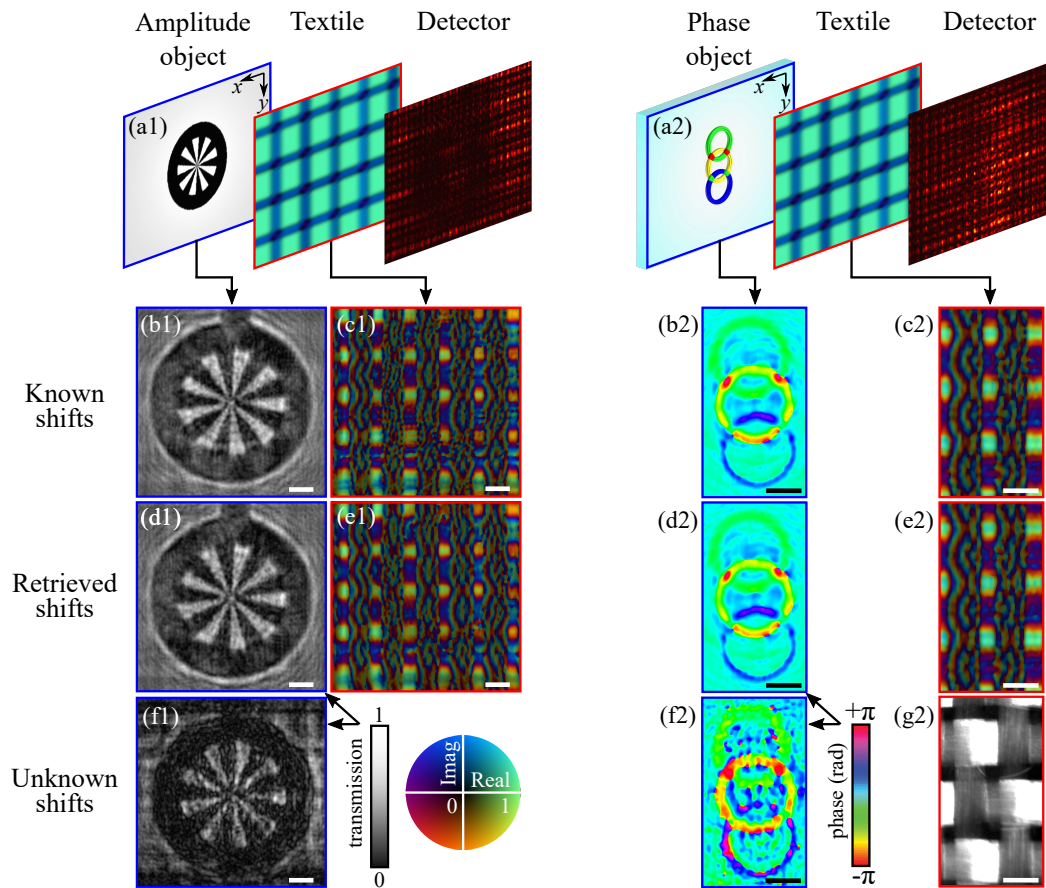


Fig. 9.2.: Experimental reconstructions of the textile and the hidden objects (amplitude object on the left-hand side, label 1; phase object on the right-hand side, label 2). (a) Schematic of the hidden object. Reconstructed hidden object [textile] (b) [(c)] using prior information of the shifts applied to the textile, (d) [(e)] after retrieving the shifts through cross-correlation, and (f) assuming unknown shifts. (g2) Image of the textile taken with a microscope in reflection mode. The lower right panels show the colorbars used for amplitude, phase and complex-valued reconstructions. The reconstructions of the textile share the same colorbar, where the hue encodes ϕ_t and the brightness $\sqrt{|t|}$. Scale bars: 1 mm. From [Valzania et al., 2019].

the textile are washed out, and the hidden object is revealed, as can be seen in Fig. 9.2(f1). The worse resolution of this reconstruction, compared to the ones in Figs. 9.2(b1) and (d1), is due to the fact that averaging a quasi-periodic pattern, like the structure of the textile, is not as efficient as averaging a non-periodic object. Since an integer number of textile periods will be summed up only accidentally, amplitude and phase modulations may be left on the background after stitching.

The right-hand side of Fig. 9.2 shows the corresponding reconstructions of the pure phase object. We note that, in all the reconstructions of the textile, its pattern along y is more visible than the one along x . This feature is ascribed to a polarization-dependent transmission through the textile fibers, which preferentially transmit THz radiation with a polarization perpendicular to their alignment direction. A comparison with an image of the textile taken with a microscope [Fig. 9.2(g2)]

confirms our hypothesis, as it shows that the reconstructed fibers are oriented along x , consistently with an independently measured incident polarization along y . Owing to a lower diffraction by the phase object compared to the amplitude object, for the former we were able to retrieve the absolute positions of the textile with an average error as low as $17 \mu\text{m}$ (1 camera pixel). The phase resolution ρ_ϕ was estimated as done for the ptychographic reconstruction of the same object in Chapter 6, namely with the standard deviation of the reconstructed phase inside the two rings farthest from each other, evaluated in regions far more than one lateral resolution from the edges of the rings, where it is supposed to be uniform. We obtained values of 0.30 rad, 0.31 rad and 0.67 rad with known, extracted through cross-correlation and unknown shifts, respectively, which translate to depth resolutions $\rho_d = \lambda\rho_\phi/[2\pi(n_{PP} - 1)]$ of 9.0 , 9.2 ($\approx \lambda/10$) and $20 \mu\text{m}$ ($\approx \lambda/5$), respectively.

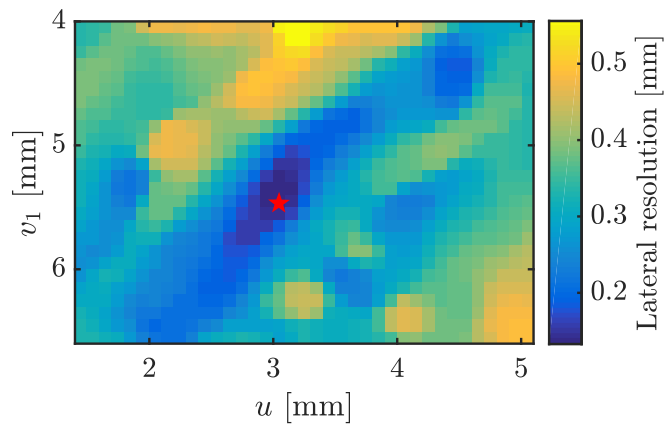


Fig. 9.3.: Lateral resolution of the hidden amplitude object reconstructed at multiple (u, v_1) distances (u : distance between the two objects; v_1 : textile-camera distance). The red star indicates the values used for the results on the left-hand side of Fig. 9.2 and in Fig. 9.4. From [Valzania et al., 2019].

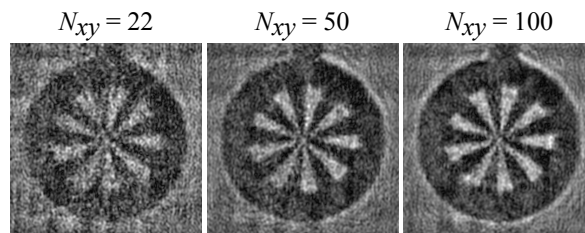


Fig. 9.4.: Reconstructed hidden amplitude object using $N_{xy} = 22$ (left), 50 (middle), and 100 (right) exit waves selected at random positions. From [Valzania et al., 2019].

9.5 Discussion

This imaging technique consists of the combination of a known phase retrieval algorithm, named SBMIR, and a method for the separation of the transmission

functions of the objects, based on a stitching procedure. It should be noted, however, that the SBMIR phase retrieval can be replaced by any other phase retrieval approach, be it iterative or not. For instance an off-axis holographic setup would obviate the need for the longitudinal camera stepping and thus reduce the measurement time. As a drawback, this would introduce the limitations already described in section 5.5.

As anticipated, our technique bears a resemblance to ptychography in two aspects. The first one concerns the experimental method, in that transverse shifts are used to reconstruct two transmission functions. The second aspect is related to the mathematical model, since in both techniques a multiplicative approximation is assumed when describing the interaction between the two transmission functions. This implies that the first and second object (or, in the ptychographic analogy, the illumination function and the object transmission function) can be interchanged, without modifying the mathematical description of the problem. To confirm our hypothesis, we reconstructed the same objects with interchanged positions, so that the textile was hidden, and the results are shown in Fig 9.5. The reconstructions of the textile are worse due to two reasons. First, in these experiments it was farther from the detector than in the previous ones. Second, its reconstruction distance cannot be refined by optimizing the resolution of the object, as done previously [see Fig. 9.3 again].

On the other hand, the fundamental difference between the two reconstruction procedures is that, while in ptychography the shifts provide both redundant and new information to solve the phase problem, here they serve as a means to separate the transmission functions, once their product is known from phase retrieval. Furthermore, our method is overall computationally simpler than ptychography, because it requires neither starting guesses of the solutions, nor fine tuning of the update parameters. This comes at the expense of a somewhat more complicated experimental setup, needed to perform the preliminary phase retrieval. Besides these preliminary observation, we believe that thorough comparisons between the two techniques are worthwhile.

A fabric sample was chosen as the cover object because of the potential application of this method to imaging through wound casts, in the context of imaging the interface between skin and textiles discussed in Chapter 1, where seeing through textiles is a crucial requirement. Our results are still preliminary, because a transmission rather than a reflection setup was employed. However, we can already claim that several features of our method are suited to this use. First, relative shifts between the two objects on the order of the THz wavelength naturally occur in such cases. Second, we can account for random shifts. Third, such shifts need not be known, because they can be either retrieved or neglected, if one is interested in reconstructing the hidden object only, thus suggesting that fly-scan imaging is also achievable.

Interestingly, since no assumptions on the two transmission functions have been made, further applications of our method go beyond the use of THz radiation and reconstructions through quasi-periodic objects. For example, Wu et al. [Wu et al., 2017] reported reconstructions of a multiple scattering medium and an object hidden behind it within the multiplicative approximation, using diffraction patterns collected by longitudinally stepping the camera. In order to identify a shift-invariant point-spread function, they needed the hidden object to be placed within the angular speckle correlation range of the multiple scattering medium. Our approach could be an alternative solution to their problem. Although the number of required diffraction patterns must be increased by a factor N_{xy} , no speckle correlations must be assumed, making the experimental constraints more relaxed in terms of field of view, size of the objects and their relative distance. Such results would represent a significant step towards imaging through biological tissues, representing the most relevant example of multiple scattering media. In this perspective, one can foresee reconstructing hidden objects, such as tumor masses, along with their surrounding environment of healthy tissue.

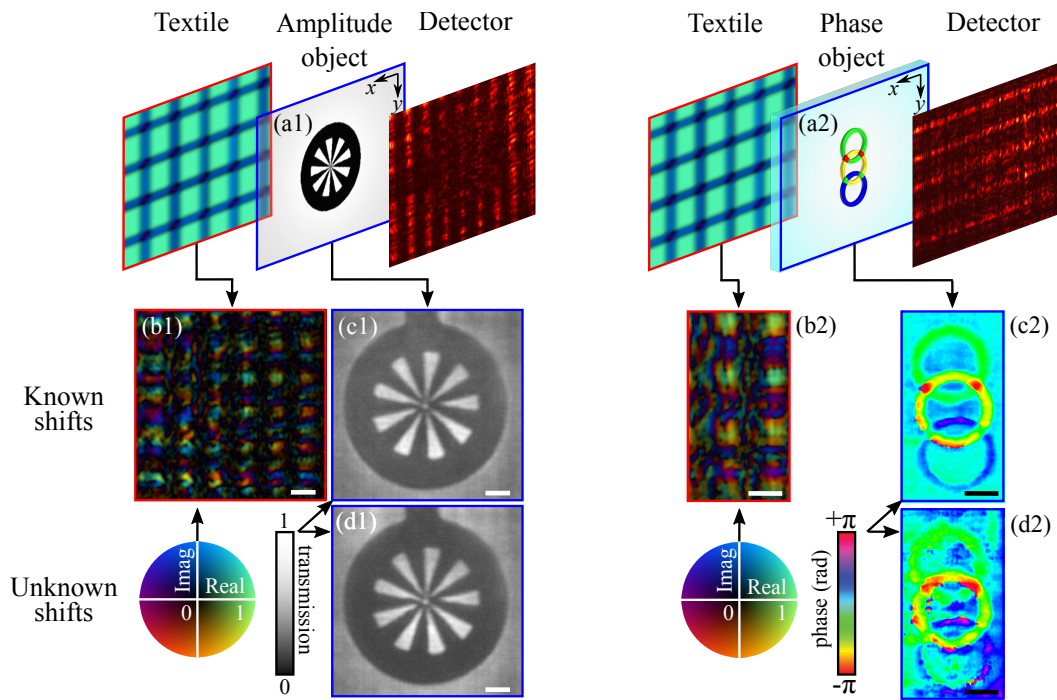


Fig. 9.5.: Experimental reconstructions of the object and the textile hidden behind it (amplitude object on the left-hand side, label 1; phase object on the right-hand side, label 2). (a) Schematic of the object. Reconstructed textile [object] (b) [(c)] using prior information of the shifts applied to the textile, and (d) assuming unknown shifts. The lower left panels show the colorbars used for amplitude, phase and complex-valued reconstructions. The reconstructions of the textile share the same colorbar, where the hue encodes ϕ_t and the brightness $\sqrt{|t|}$. Scale bars: 1 mm. From [Valzania et al., 2019].

9.6 Conclusions

In this Chapter, we described a coherent imaging technique for reconstructing a scattering object and an object hidden behind it in a transmission geometry, working in two steps. First, the combined wavefront diffracted by the two objects was reconstructed through a phase retrieval procedure. Second, relative transverse shifts between the two objects were implemented and used in a stitching algorithm to separate their transmission functions, where a multiplicative interaction was assumed between them. Experimental demonstration was provided with a THz laser, by reconstructing a glass fabric sample and a hidden pure amplitude or pure phase object. For the former, we showed that the obtained lateral resolution is close to the resolution of a simulated and unhidden amplitude object (see also Appendix E). The applied shifts were shown to be reliably retrievable through cross-correlation of the experimental images, without any prior knowledge. This aspect makes our method particularly interesting for the real-life applications described in Chapter 1, where the relative shifts between two objects, e.g. skin and a textile sample, are not known. Analogies and differences with ptychography were also outlined. Although a quantitative comparison is still needed, we believe that the implemented technique can replace ptychography in some situations, e.g. when the experimental setup allows for an additional phase retrieval step through a longitudinal camera scan, as shown in these results, or a reference beam. Finally, potential applications were discussed in the context of non-invasive imaging technologies, especially for the investigation of complex biological tissues.

Conclusions and outlook

Throughout this work, advancements in full-field, coherent and lensless THz imaging have been contributed in different aspects, namely:

1. The evaluation of the performance of thermal cameras for real-time THz imaging;
2. The assessment of THz imaging towards the reconstruction of biological samples;
3. The development and implementation of new coherent lensless imaging techniques.

In what follows, we are going to discuss the obtained results and their outlook from the perspective of the application described in Chapter 1, which consists of using THz imaging to deliver real-time images of skin for health monitoring through textiles such as, among others, clothes, wound casts, or wearable sensors.

Currently, infrared micro-bolometers can be regarded as the best cameras in the THz range. Although they are designed for a different frequency range, satisfactory values of signal-to-noise ratio are obtained upon dark frame subtraction (Chapter 4). However, this approach limits the frame rate, since the dark frame should be taken as close in time as possible to the image, so to allow an efficient background subtraction even in cases where the imaged scene is subject to thermal drifts around room temperature. To obviate the need for dark frame subtraction, real-time THz imaging would greatly benefit from the development of THz cameras with comparable performance to infrared arrays.

The need for better THz cameras was also realized when imaging complicated objects, like the fingertip replica (Chapter 5). Successful reconstructions were obtained only with an off-axis digital holographic setup with a synthetic aperture acquisition, improving the measurement data in two aspects: (i) increase of the numerical aperture and, consequently, of the lateral resolution, through the increased detector size and (ii) increase of the signal-to-noise ratio through the redundant data collected in the regions measured multiple times. One can therefore obviate synthetic aperture approaches, thereby making the measurements faster, by using cameras with a larger detector area and a lower noise equivalent power (NEP). Although promising THz detectors have been manufactured (see, e.g., [Boppel et al., 2012]), whose NEP is close to the one of the infrared camera used in our experiments, the reported array size and frame rate are still far from reaching those of infrared cameras. Similar considerations are valid for THz sources: in order to make real-time THz imaging of skin-textile interfaces possible, the portability of the imaging system is a crucial requirement. While much smaller, on-chip sources

working at room temperature are currently available (e.g., quantum cascade lasers [Belkin and Capasso, 2015]), their power is a factor ≈ 30 lower than that of gas lasers.

A relevant step towards our goal would be to obtain reconstructions, comparable to the ones in Chapter 5, on real skin samples. *In vivo* measurements certainly provide the most realistic conditions to evaluate the potential of our technique. More controlled and reproducible experiments can instead be performed with *ex vivo* and *in vitro* studies, although some physiological functions may be altered.

The issue of reconstructing objects larger than the beam size was solved by implementing ptychography, a scan-based coherent lensless technique which exploits relative movements between the beam and the object to iteratively reconstruct the latter (Chapters 6 and 7). It is noteworthy that, in the context of our selected application, movements of skin against a counter-surface are at the basis of friction processes. Ptychography can naturally take advantage of such movements to reconstruct the scene, provided that the camera records partially overlapping images. The need to deal with continuous movements of the object should not pose a problem, since ptychography has been demonstrated to achieve fly-scan imaging in the X-ray range [Odstrčil et al., 2018].

The innovative phase retrieval technique developed and implemented in Chapter 9, reconstructing two objects stacked one in front of the other, also exploits relative movements between them. It could be further improved by noting that physical translations of the objects can also be mimicked with tilted illuminations, as in the reciprocal space variant of ptychography, named Fourier ptychography [Zheng et al., 2013]. Adding an angular scan would introduce constraints between the diffraction patterns obtained with translated objects and no tilt in the illumination and those obtained with steady objects and tilted illumination. It would also be desirable to allow reconstructions behind objects much thicker than the THz wavelength, for which the multiplicative approximation used in Eq. (9.1) breaks down. Here multi-slice approaches, like those employed in ptychography [Tsai et al., 2016], could be implemented. Yet another improvement of our method is making it applicable in a reflection setup. Along these lines, one may think of combining it with time-resolved measurements, which allow discriminating the wavefronts reflected from one object or the other, based on their arrival time on the detector. For instance, using a THz photoconductive emitter, like the one manufactured by Toptica [*Photoconductive antennas, Toptica Photonics*], in a low-coherence holographic setup would yield a depth resolution in reflection of about the coherence length of the source, that is, $20\ \mu\text{m}$. At the currently available average powers, on the order of $10\ \mu\text{W}$, THz pulses can penetrate several mm of non-conducting materials, like textiles, while posing no danger on human health. Once these upgrades are implemented, reconstructions behind weakly diffracting covers in reflection mode, like the ones reported in Chapter 8, would be achievable without large efforts.

One of the two tasks related to imaging skin-textile interfaces which still needs to be tackled [see Fig. 1.1(b)] is imaging the contact area of two objects subject to friction. This situation introduces a further complication in the reconstruction procedure devised in Chapter 9, that is, the two objects are not always the same while they are rubbed against each other, owing to mechanical deformations at the interface. A possible approach to deal with it consists of assuming the object functions not to change significantly, except for an overall translation, within close positions.

The second step, which we have not taken yet towards our application, is assessing the capability of our techniques to image the interfacial humidity content. If, on the one hand, the strong absorption of THz radiation by water worsens the reconstruction of the interface with increasing water content, on the other hand it can be used as a contrast agent, allowing us to follow the onset of sweating processes in real-time. What would have to be estimated is the minimum resolvable amount of water and the maximum hydration level of skin, which still enables its reconstruction.

As a last word, we would like to stress that the relevance of the methods implemented in this thesis goes well beyond the application considered here. Further applications are expected in materials science, e.g., for the investigation of THz-transparent materials, like plastics and intrinsic semiconductors. Also, our methods are not restricted to the use of THz radiation, thus giving our studies a broad impact on the field of coherent lensless imaging techniques, which is currently living an exciting era.

Appendices

Proof of the object update equation in the extended ptychographical iterative engine (ePIE)

In this Appendix, the update equation for the object transmission function of the extended ptychographical iterative engine (ePIE) [Eq. (2.36a)] will be derived in three ways. Because of the analogy between Eq. (2.36a) and the update equation for the probe function [Eq. (2.36b)], the latter can be obtained in the same manner, by swapping the object with the probe function. The approach adopted by [Maiden et al., 2017] will be followed.

A.1 First proof: weighted sum of solutions

Let us consider Eq. (2.32), expressing the multiplicative interaction between the k th estimates of the probe function $p_k(\mathbf{x})$ and of the object function $o_k(\mathbf{x} - \mathbf{x}_k)$. Applying the change of variables $\mathbf{x} \rightarrow \mathbf{x} + \mathbf{x}_k$, it becomes

$$\psi_k(\mathbf{x} + \mathbf{x}_k) = p_k(\mathbf{x} + \mathbf{x}_k)o_k(\mathbf{x}). \quad (\text{A.1})$$

A reasonable tentative solution for the new object function $o_{k+1}(\mathbf{x})$ would be the following:

$$o_{k+1}(\mathbf{x}) = \frac{\psi'_k(\mathbf{x} + \mathbf{x}_k)}{p_k(\mathbf{x} + \mathbf{x}_k)}, \quad (\text{A.2})$$

where we recall that $\psi'_k(\mathbf{x} + \mathbf{x}_k)$ is the k th estimate of the exit wave at the object plane, after correction with the intensity constraint. However, such an estimate is poorly conditioned when $p_k(\mathbf{x} + \mathbf{x}_k)$ is below the noise level. Therefore, a better estimate consists of maintaining the previous estimate $o_k(\mathbf{x})$ in regions where $p_k(\mathbf{x} + \mathbf{x}_k)$ is low and using Eq. (A.2) where it is well above the noise. If we define a weight function $0 \leq w_k(\mathbf{x} + \mathbf{x}_k) \leq 1$, which evaluates to 1 where $p_k(\mathbf{x} + \mathbf{x}_k)$ is high and approaches 0 where $p_k(\mathbf{x} + \mathbf{x}_k)$ is low, the new estimate can be written as follows

$$\begin{aligned} o_{k+1}(\mathbf{x}) &= [1 - w_k(\mathbf{x} + \mathbf{x}_k)]o_k(\mathbf{x}) + w_k(\mathbf{x} + \mathbf{x}_k) \frac{\psi'_k(\mathbf{x} + \mathbf{x}_k)}{p_k(\mathbf{x} + \mathbf{x}_k)} \\ &= o_k(\mathbf{x}) + w_k(\mathbf{x} + \mathbf{x}_k) \frac{p_k^*(\mathbf{x} + \mathbf{x}_k)}{|p_k(\mathbf{x} + \mathbf{x}_k)|^2} [\psi'_k(\mathbf{x} + \mathbf{x}_k) - \psi_k(\mathbf{x} + \mathbf{x}_k)], \end{aligned} \quad (\text{A.3})$$

where the last side has been obtained using Eq. (A.1). Setting

$$w_k(\mathbf{x} + \mathbf{x}_k) \equiv \alpha^{(o)} \frac{|p_k(\mathbf{x} + \mathbf{x}_k)|^2}{\max_{\mathbf{x}} |p_k(\mathbf{x} + \mathbf{x}_k)|^2}, \quad (\text{A.4})$$

with $0 \leq \alpha^{(o)} \leq 1$, yields Eq. (2.36a).

A.2 Second proof: gradient descent

Let us consider the following error function, evaluating the difference between the k th estimate of the exit wave at the object plane and its corrected version using the intensity constraint:

$$\begin{aligned} E_k^{(\text{res})}(\mathbf{x}) &\equiv |\psi_k(\mathbf{x} + \mathbf{x}_k) - \psi'_k(\mathbf{x} + \mathbf{x}_k)|^2 \\ &= |p_k(\mathbf{x} + \mathbf{x}_k)o_k(\mathbf{x}) - \psi'_k(\mathbf{x} + \mathbf{x}_k)|^2. \end{aligned} \quad (\text{A.5})$$

We aim at finding an object function decreasing $E_k^{(\text{res})}(\mathbf{x})$. To this end, we calculate the rate of change of $E_k^{(\text{res})}(\mathbf{x})$ when the object changes, by computing the gradient of $E_k^{(\text{res})}(\mathbf{x})$ with respect to $o_k(\mathbf{x})$. Recalling that $\nabla_x |ax - b|^2 = 2a^*(ax - b)$ and making use of Eq. (A.1), we obtain

$$\begin{aligned} \nabla_{o_k} E_k^{(\text{res})}(\mathbf{x}) &= 2p_k^*(\mathbf{x} + \mathbf{x}_k) [p_k(\mathbf{x} + \mathbf{x}_k)o_k(\mathbf{x}) - \psi'_k(\mathbf{x} + \mathbf{x}_k)] \\ &= -2p_k^*(\mathbf{x} + \mathbf{x}_k) [\psi'_k(\mathbf{x} + \mathbf{x}_k) - \psi_k(\mathbf{x} + \mathbf{x}_k)] \end{aligned} \quad (\text{A.6})$$

The new estimate of the object function will therefore be obtained by changing the object by the amount γ in the direction opposite to the gradient:

$$\begin{aligned} o_{k+1}(\mathbf{x}) &= o_k(\mathbf{x}) - \gamma \nabla_{o_k} E_k^{(\text{res})}(\mathbf{x}) \\ &= o_k(\mathbf{x}) + 2\gamma p_k^*(\mathbf{x} + \mathbf{x}_k) [\psi'_k(\mathbf{x} + \mathbf{x}_k) - \psi_k(\mathbf{x} + \mathbf{x}_k)]. \end{aligned} \quad (\text{A.7})$$

Equation (A.7) is equivalent to Eq. (2.36a) when

$$\gamma \equiv \frac{\alpha^{(o)}}{2 \max_{\mathbf{x}} |p_k(\mathbf{x} + \mathbf{x}_k)|^2}. \quad (\text{A.8})$$

A.3 Third proof: minimization of a regularized cost function

In [Thibault and Menzel, 2013] the following regularized error function was considered:

$$E_k^{\text{reg}}(\mathbf{x}) \equiv |p_k(\mathbf{x} + \mathbf{x}_k)o_{k+1}(\mathbf{x}) - \psi'_k(\mathbf{x} + \mathbf{x}_k)|^2 + u_k(\mathbf{x} + \mathbf{x}_k)|o_{k+1}(\mathbf{x}) - o_k(\mathbf{x})|^2. \quad (\text{A.9})$$

It is minimized at the stationary point, obtained by setting to zero its gradient with respect to the new object function

$$\begin{aligned} \nabla_{o_{k+1}} E_k^{(\text{reg})}(\mathbf{x}) = & 2p_k^*(\mathbf{x} + \mathbf{x}_k) [p_k(\mathbf{x} + \mathbf{x}_k)o_{k+1}(\mathbf{x}) - \psi'_k(\mathbf{x} + \mathbf{x}_k)] + \\ & + 2u_k(\mathbf{x} + \mathbf{x}_k)[o_{k+1}(\mathbf{x}) - o_k(\mathbf{x})]. \end{aligned} \quad (\text{A.10})$$

This yields

$$o_{k+1}(\mathbf{x}) = o_k(\mathbf{x}) + \frac{p_k^*(\mathbf{x} + \mathbf{x}_k)}{|p_k(\mathbf{x} + \mathbf{x}_k)|^2 + u_k(\mathbf{x} + \mathbf{x}_k)} [\psi'_k(\mathbf{x} + \mathbf{x}_k) - \psi_k(\mathbf{x} + \mathbf{x}_k)], \quad (\text{A.11})$$

where Eq. (A.1) has been used once again. Equation (A.11) becomes Eq. (2.36a) if we choose

$$u_k(\mathbf{x} + \mathbf{x}_k) \equiv \frac{\max_{\mathbf{x}} |p_k(\mathbf{x} + \mathbf{x}_k)|^2}{\alpha^{(o)}} - |p_k(\mathbf{x} + \mathbf{x}_k)|^2. \quad (\text{A.12})$$

Combining Eqs. (A.4) and (A.12) we also get

$$u_k(\mathbf{x} + \mathbf{x}_k) = |p_k(\mathbf{x} + \mathbf{x}_k)|^2 [w_k^{-1}(\mathbf{x} + \mathbf{x}_k) - 1], \quad (\text{A.13})$$

from which we deduce that w_k and u_k have an opposite effect on the update of the object function. On the one hand, a large value of w_k is employed where a change of the object can be trusted, namely where the probe is much higher than the noise level. On the other hand, u_k can be regarded as a penalty term, which is large where the probe is comparable to the noise level. As a consequence, in those regions the cost function $E_k^{(\text{reg})}$ is large and updating the object is not considered reliable.

Definition of some detector figures of merit used in Chapter 4

In this appendix, some of the figures of merit used to characterize the thermal cameras compared in Chapter 4 will be defined. The equations that will be provided, taken from [Kruse, 2001], have been used to calculate the NEP and D^* values reported in Table 4.1.

Responsivity

The responsivity R is defined as the ratio between the output signal S_{out} from a pixel and the radiant power P_{in} incident on it, namely

$$R \equiv \frac{S_{\text{out}}}{P_{\text{in}}}. \quad (\text{B.1})$$

Because S_{out} is usually a voltage or a current, R is expressed in V/W or A/W.

Noise equivalent power

The noise equivalent power NEP , expressed in W, corresponds to the radiant power incident on a pixel and giving rise to a signal S_{out} equal to the noise level N within the device bandwidth. Using Eq. (B.1) with $P_{\text{in}} = NEP$ and $S_{\text{out}} = N$ gives

$$NEP \equiv \frac{N}{R}. \quad (\text{B.2})$$

Noise equivalent temperature difference

The noise equivalent temperature difference $NETD$ is defined as the change in temperature of a blackbody, giving rise to a change of the signal-to-noise ratio $SNR \equiv S_{\text{out}}/N$ by 1. Unlike the previous parameters, $NETD$ also depends on the optics used to produce the image on the detector, as well as the temperature. It is calculated as follows,

$$NETD \equiv \frac{4F^2}{T_{\text{opt}}} \frac{NEP}{A_{\text{pix}}(dI/dT)_{\lambda_1-\lambda_2}}, \quad (\text{B.3})$$

where $F \equiv (2NA_{\text{opt}})^{-1}$ is a geometric factor inversely proportional to the numerical aperture of the optics, T_{opt} is the optics power transmission coefficient, A_{pix} is the area of one pixel, and $(dI/dT)_{\lambda_1-\lambda_2}$ is the rate of change of the radiant intensity emitted by a blackbody, expressed in W/m², with respect to the temperature T and

within the wavelength range $[\lambda_1, \lambda_2]$. For a thermal detector designated in the infrared band $[8, 14] \mu\text{m}$, one has $(dI/dT)_{8-14} = 2.62 \text{ W m}^{-2} \text{ K}^{-1}$. When the detector is used without optics, as in the studies performed in Chapter 4, we can set $T_{\text{opt}} = NA_{\text{opt}} = 1$, so that the first fraction on the right-hand side of Eq. (B.3) equals 1 and the $NETD$ takes the simplified form

$$NETD' \equiv \frac{NEP}{A_{\text{pix}}(dI/dT)_{\lambda_1-\lambda_2}}. \quad (\text{B.4})$$

Equation (B.4) has been used in Chapter 4 to calculate the NEP in cases where only the $NETD'$ was available from the camera specification sheet. When the pixel pitch instead of the pixel size was known, the former was used to calculate A_{pix} .

Specific detectivity

The specific detectivity D^* can be regarded as the reciprocal of the NEP , normalized to the square root of the pixel area and of the bandwidth B , namely

$$D^* \equiv \frac{\sqrt{A_{\text{pix}}B}}{NEP}. \quad (\text{B.5})$$

It is commonly expressed in $\text{cm}\sqrt{\text{Hz}}/\text{W}$, a unit which is also known as Jones. The values of D^* compiled in Table 4.1 have been calculated from Eq. (B.5) assuming $B = 1 \text{ Hz}$.

Definition of the stitching operator \mathcal{S} used in Chapters 5, 9

Let us consider two functions $f, g: \mathbf{D} \mapsto \mathbb{R}$ describing two images taken at different positions of the camera, with $\mathbf{D} \equiv \mathbf{D}_f \cup \mathbf{D}_g$ and $\mathbf{D}_f, \mathbf{D}_g$ denoting the detection areas while acquiring f and g , respectively. Therefore, they are assumed to evaluate to 0 on either $\mathbf{D} \setminus \mathbf{D}_f$ or $\mathbf{D} \setminus \mathbf{D}_g$. We define the sum operator acting on f and g , $\mathbb{S}(f, g)$, as follows:

$$\mathbb{S}(f, g) = \begin{cases} f(\mathbf{x}) & \text{if } \mathbf{x} \in \mathbf{D}_f \setminus \mathbf{D}_g \\ 1/2[f(\mathbf{x}) + g'(\mathbf{x})] & \text{if } \mathbf{x} \in \mathbf{D}_f \cap \mathbf{D}_g, \\ g'(\mathbf{x}) & \text{otherwise} \end{cases} \quad (\text{C.1})$$

where g' is derived from g in a way that ensures that f and g have the same mean value in their overlap region, i.e. $g'(\mathbf{x}) \equiv \alpha g(\mathbf{x}) + \beta$. The gain α and the offset β are used to compensate for exposure differences during the acquisition of the images and are obtained through a pixel-wise linear regression in the overlap region $\mathbf{D}_f \cap \mathbf{D}_g$.

If f and g contain circular data because, for instance, they represent phase values bound in the range $[-\pi, \pi)$, the sum in their overlap region must be carefully performed. In order to avoid 2π -jumps, the stitched image obtained from f and g , $\mathcal{S}(f, g)$, must be calculated according to $\mathcal{S}(f, g) = \arctan2[\mathbb{S}(\sin f, \sin g), \mathbb{S}(\cos f, \cos g)]$, where $\alpha = 1$ and β compensating for a phase offset between f and g with no physical relevance.

In all the other cases, the sum operator applied to the two images directly provides the stitched image, that is, $\mathcal{S}(f, g) = \mathbb{S}(f, g)$.

Finally, we extend the stitching operation to more than two images by defining the new, extended stitching operator \mathcal{S} , acting on the set of f_m . Denoting with $\mathbf{1}_m$ the indicator function of each f_m , which equals 1 in the corresponding detector area and 0 elsewhere in the total stitched image, we define the stitched image recursively with the following cumulative moving average:

$$\mathcal{S}_{m=1}^M(f_m) \equiv \mathcal{S} \left(\frac{2}{\sum_{m=1}^M \mathbf{1}_m} f_M, \frac{2 \sum_{m=1}^{M-1} \mathbf{1}_m}{\sum_{m=1}^M \mathbf{1}_m} \mathcal{S}_{m=1}^{M-1}(f_m) \right), \quad \text{with } \mathcal{S}_{m=1}^1(f_m) \equiv f_1, \quad (\text{C.2})$$

that is, the stitching is performed pair-wise between the new image and the already stitched image.

Rotational transformation of the complex amplitude of a wavefront

We analytically derive an expression for the complex amplitude of a wavefront in a coordinate system rotated with respect to the camera coordinate system at which it is usually reconstructed. The approach described in [Matsushima et al., 2003; Matsushima, 2008] will be mostly followed.

D.1 Definitions

We refer to the coordinate systems shown in Fig. 5.1(b). A wavefront u is described in the “camera coordinates” $\mathbf{r} \equiv (x, y, z)$ after it has been reconstructed via one of the techniques described in this thesis. Let us assume that its $(x, y, 0)$ plane is parallel to the camera detection plane and its origin is at the center of the object and at the distance d from the center of the detection plane. The wavefront $u(x, y, z)$ may therefore have been obtained upon back-propagating the complex amplitude retrieved at the detection plane by the distance d . We wish to express u in the “object coordinate system” $\hat{\mathbf{r}} \equiv (\hat{x}, \hat{y}, \hat{z})$, whose $(\hat{x}, \hat{y}, 0)$ plane lies on the object. This coordinate system shares the origin with \mathbf{r} and it is obtained by applying a rotational transformation, described by the matrix Θ , to \mathbf{r} , as follows:

$$\hat{\mathbf{r}} = \Theta \mathbf{r} \quad (\text{D.1a})$$

$$\mathbf{r} = \Theta^{-1} \hat{\mathbf{r}}, \quad (\text{D.1b})$$

where the inverse matrix Θ^{-1} equals the transpose matrix Θ^T . Denoting the matrix elements of Θ with

$$\Theta \equiv \begin{pmatrix} a_1 & a_4 & a_7 \\ a_2 & a_5 & a_8 \\ a_3 & a_6 & a_9 \end{pmatrix}, \quad (\text{D.2})$$

then

$$\Theta^{-1} \equiv \Theta^T = \begin{pmatrix} a_1 & a_2 & a_3 \\ a_4 & a_5 & a_6 \\ a_7 & a_8 & a_9 \end{pmatrix}. \quad (\text{D.3})$$

We hereby note that if the rotation axis, described through the unit vector $\mathbf{b} \equiv (b_x, b_y, b_z)$, $|\mathbf{b}| = 1$, and the rotation angle β are known, then Θ takes the more suggestive form, obtained from Rodrigues' rotation formula [Mebius, 2007]:

$$\Theta = \exp(\beta \mathbf{B}) \quad (\text{D.4a})$$

$$\mathbf{B} \equiv \begin{pmatrix} 0 & -b_z & b_y \\ b_z & 0 & -b_x \\ -b_y & b_x & 0 \end{pmatrix}. \quad (\text{D.4b})$$

In the following derivation, we will adopt the notation with the general matrix elements of Eqs. (D.2) and (D.3).

D.2 Angular spectrum representation of $u(\mathbf{x}, y, z)$

We first write the wavefront $u(x, y, z)$ in a convenient way, which will ease the coordinate transformation detailed in the next section. We begin by expressing $u(x, y, 0)$ through its two-dimensional Fourier Transform $U(f_x, f_y)$, namely:

$$u(x, y, 0) = \mathcal{F}^{-1}\{U(f_x, f_y)\} \equiv \iint_{-\infty}^{+\infty} U(f_x, f_y) \exp[2\pi i(f_x x + f_y y)] df_x df_y, \quad (\text{D.5})$$

where the spatial frequencies of $u(x, y, z)$ along x and y have been denoted with f_x and f_y , respectively. We realize that Eq. (D.5) describes $u(x, y, 0)$ as a superposition of plane waves in the form

$$A_{k_x, k_y} \exp[i(k_x x + k_y y)], \quad (\text{D.6})$$

with amplitudes A_{k_x, k_y} and wavevectors $\mathbf{k} \equiv (k_x, k_y, k_z)$, which propagate at the angles $\cos^{-1}(k_x/|\mathbf{k}|)$ and $\cos^{-1}(k_y/|\mathbf{k}|)$ with respect to the x and y axes, respectively. For this reason, $U(f_x, f_y)$ is also referred to as the *angular spectrum* of $u(x, y, 0)$. Comparing the integrand on the right-hand side of Eq. (D.5) with Eq. (D.6), A_{k_x, k_y} corresponds to the infinitesimal quantity $U(f_x, f_y)df_x df_y$, while the x and y components of the wavevector are $k_{x,y} = 2\pi f_{x,y}$. The z component of the wavevector instead depends on k_x, k_y , as the modulus $|\mathbf{k}|$ must satisfy $|\mathbf{k}| \equiv \sqrt{k_x^2 + k_y^2 + k_z^2} \equiv 2\pi/\lambda$, leading to $k_z = k_z(k_x, k_y) = \sqrt{4\pi^2/\lambda^2 - k_x^2 - k_y^2}$. By analogy with f_x and f_y , the spatial frequency along z can be defined as $f_z \equiv k_z/(2\pi)$, and is obtained from f_x, f_y through $f_z(f_x, f_y) = \sqrt{\lambda^{-2} - f_x^2 - f_y^2}$. This allows us to write the wavefront u at any position in space, $u(x, y, z)$, as

$$u(x, y, z) = \iint_{-\infty}^{+\infty} U(f_x, f_y) \exp\{2\pi i[f_x x + f_y y + f_z(f_x, f_y)z]\} df_x df_y. \quad (\text{D.7})$$

D.3 Coordinate transformation

We are now interested in expressing $u(x, y, z)$ in the object coordinate system, and evaluate it on the object plane $(\hat{x}, \hat{y}, 0)$. Let us identify this sought quantity with $\hat{u}(\hat{x}, \hat{y}, 0)$. Because the fields u and \hat{u} must represent the same wavefront, we must have

$$\hat{u}(\hat{\mathbf{r}}) = u(\mathbf{r}) \quad (\text{D.8})$$

which, using Eqs. (D.1b), (D.3) and (D.7) and evaluating at $\hat{\mathbf{r}} = (\hat{x}, \hat{y}, 0)$, yields the following:

$$\begin{aligned} \hat{u}(\hat{x}, \hat{y}, 0) &= u(a_1\hat{x} + a_2\hat{y}, a_4\hat{x} + a_5\hat{y}, a_7\hat{x} + a_8\hat{y}) \\ &= \iint_{-\infty}^{+\infty} U(f_x, f_y) \exp\{2\pi i[(a_1f_x + a_4f_y + a_7f_z)\hat{x} + (a_2f_x + a_5f_y + \\ &\quad + a_8f_z)\hat{y}]\} df_x df_y. \end{aligned} \quad (\text{D.9})$$

Note that the matrix Θ also transforms the wavevector \mathbf{k} and, consequently, the spatial frequencies $\mathbf{f} \equiv (f_x, f_y, f_z)$, from the camera coordinate system to the object coordinate system, as it does for the spatial coordinates \mathbf{r} , that is,

$$\hat{\mathbf{f}} = \Theta \mathbf{f} \quad (\text{D.10a})$$

$$\mathbf{f} = \Theta^{-1} \hat{\mathbf{f}}, \quad (\text{D.10b})$$

Therefore, the first and last sides of Eq. (D.9) can be rewritten as

$$\hat{u}(\hat{x}, \hat{y}, 0) = \iint_{-\infty}^{+\infty} U(f_x, f_y) \exp\{2\pi i[\hat{f}_x\hat{x} + \hat{f}_y\hat{y}]\} df_x df_y. \quad (\text{D.11})$$

In order to write $\hat{u}(\hat{x}, \hat{y}, 0)$ in a form similar to Eq. (D.5), we should now express $U(f_x, f_y)df_xdf_y$ as a function of the transformed spatial frequencies \hat{f}_x, \hat{f}_y . Let us define the following function $\alpha(\hat{f}_x, \hat{f}_y)$:

$$\alpha(\hat{f}_x, \hat{f}_y) \equiv [\alpha_1(\hat{f}_x, \hat{f}_y); \alpha_2(\hat{f}_x, \hat{f}_y)], \quad (\text{D.12})$$

with

$$f_x = \alpha_1(\hat{f}_x, \hat{f}_y) \equiv a_1\hat{f}_x + a_2\hat{f}_y + a_3\hat{f}_z(\hat{f}_x, \hat{f}_y) \quad (\text{D.13a})$$

$$f_y = \alpha_2(\hat{f}_x, \hat{f}_y) \equiv a_4\hat{f}_x + a_5\hat{f}_y + a_6\hat{f}_z(\hat{f}_x, \hat{f}_y), \quad (\text{D.13b})$$

which were obtained from Eq. (D.10b). The change of variables in the integral of Eq. (D.11) requires the determinant of the Jacobian matrix $J_\alpha(\hat{f}_x, \hat{f}_y)$ of $\alpha(\hat{f}_x, \hat{f}_y)$, which is

$$\det J_\alpha(\hat{f}_x, \hat{f}_y) = \frac{\partial \alpha_1}{\partial \hat{f}_x} \frac{\partial \alpha_2}{\partial \hat{f}_y} - \frac{\partial \alpha_1}{\partial \hat{f}_y} \frac{\partial \alpha_2}{\partial \hat{f}_x} \quad (\text{D.14})$$

and allows us to make the substitution

$$df_x df_y = |\det J_\alpha(\hat{f}_x, \hat{f}_y)| d\hat{f}_x d\hat{f}_y. \quad (\text{D.15})$$

Finally, the wavefront in the object coordinate system is written as

$$\hat{u}(\hat{x}, \hat{y}, 0) = \mathcal{F}^{-1}\{\hat{U}(\hat{f}_x, \hat{f}_y)\} \equiv \iint_{-\infty}^{+\infty} \hat{U}(\hat{f}_x, \hat{f}_y) \exp[2\pi i(\hat{f}_x \hat{x} + \hat{f}_y \hat{y})] d\hat{f}_x d\hat{f}_y, \quad (\text{D.16})$$

with

$$\hat{U}(\hat{f}_x, \hat{f}_y) \equiv U[\alpha_1(\hat{f}_x, \hat{f}_y), \alpha_2(\hat{f}_x, \hat{f}_y)] |\det J_\alpha(\hat{f}_x, \hat{f}_y)| \quad (\text{D.17})$$

and where in numerical implementations the values of $\hat{U}(\hat{f}_x, \hat{f}_y)$ are obtained by interpolation on the grid of points where $U(f_x, f_y)$ is given. If we define the following rotation operator

$$\mathcal{R}_\Theta[\cdot] \equiv \mathcal{F}^{-1}\{\mathcal{F}\{\cdot\}[\alpha_1, \alpha_2]|\det J_\alpha|\} \quad (\text{D.18})$$

then the transformed wavefront on the $(\hat{x}, \hat{y}, 0)$ plane, shortly referred to as (\hat{x}, \hat{y}) , can be expressed as

$$\hat{u}(\hat{x}, \hat{y}) = \mathcal{R}_\Theta[u](\hat{x}, \hat{y}), \quad (\text{D.19})$$

which corresponds to Eq. (5.5) for the object function o .

Optimum acquisition parameters and lateral resolution of the SBMIR technique in the THz range

The minimum recording distance of a SBMIR phase retrieval experiment can be obtained using the Nyquist criterion. The smallest period Λ contained in the fringe pattern produced by the wavefront scattered by the object must be reliably sampled by the detector pixel pitch δ . For an object of size L at a distance v from the detector, $\Lambda = \lambda/[2 \sin(\alpha/2)]$, where λ is the wavelength and $\alpha \equiv 2 \arctan[L/(2v)]$ is the angle under which an on-axis point on the detector sees the object. The Nyquist criterion requires that $2\delta < \Lambda$, or $\sin(\alpha/2) < \lambda/(4\delta)$. In the visible range [Almoro et al., 2006], this limits α to the range of a few mrad, as $\lambda_{\text{vis}}/(4\delta) \sim 10^{-2}$ for standard CCD cameras. However, using THz radiation sets no limits on α , since $\lambda_{\text{THz}}/(4\delta) > 1$, namely the object can be placed as close to the detector as experimental constraints allow, thereby increasing the numerical aperture of the imaging system.

By analogy with ptychography, the SBMIR algorithm requires that each diffraction pattern collected at a different distance from the object provides both new and redundant information. The distance along the optical axis z , after which the diffraction pattern of the object has significantly changed from the pattern at the distance v , is comparable with the depth of focus ϵ_z of the imaging system, defined as $\epsilon_z \equiv \lambda(v/w)^2$, where w is the beam diameter. Therefore a reasonable choice of the longitudinal shifts Δz is on the order of ϵ_z .

We investigated the lateral resolution ρ of the SBMIR reconstructions with simulations. The simulated object was the Siemens Star, with an inner diameter of 4 mm, already reconstructed in several Chapters of this thesis. For its reconstruction we used diffraction patterns taken at $N_z = 5$ planes perpendicular to the z -axis and 200 iterations, which were started with flat amplitude and phase distributions as the initial solution. The minimum recording distance v_1 spanned the range 1.6–12.6 mm, resulting in a maximum numerical aperture $NA_{\text{max}} \equiv \sin \theta_{\text{max}}$ between 0.35 and 0.95, where θ_{max} is half the detector acceptance angle seen from an on-axis point at the distance v_1 . The diffraction patterns were acquired at equidistant planes separated by Δz from each other. The results shown in Fig. E.1 were obtained for two values of Δz , which have been expressed in units of a reference depth of focus $\epsilon_0 = 0.87$ mm calculated at $\lambda = 96.5 \mu\text{m}$, $w = 4$ mm and $v = 12$ mm. For each reconstruction, the lateral resolution was estimated with the inverse of the cutoff

frequency of the modulation transfer function, obtained by averaging the intensity of the reconstructed wavefront along concentric rings with decreasing radii and centered with the Siemens Star, as detailed in [Valzania et al., 2018a] and in Chapter 6. Each simulation point plotted in Fig. E.1 is the average of ρ/λ , performed over 8 wavelengths in the range $96.5 - 400 \mu\text{m}$, while its standard deviation corresponds to the total length of each error bar. For fixed Δz and N_z , ρ/λ is shown to be bound by the resolution limits $(2NA_{\max})^{-1}$ (plotted with a black line) and $(2NA_{\min})^{-1}$ (plotted with the color of the corresponding Δz) from below and above, respectively, where the minimum numerical aperture NA_{\min} is calculated at the farthest recording plane, at the distance v_5 from the object. The light-blue square indicates the lateral resolution of the experimental reconstruction of Fig. 9.2(b1), obtained with a real 4-mm Siemens Star behind a glass fabric sample and the same reconstruction parameters employed here. The experimental resolution is compatible with the SBMIR reconstruction of the simulated Siemens Star, where no cover object was present.

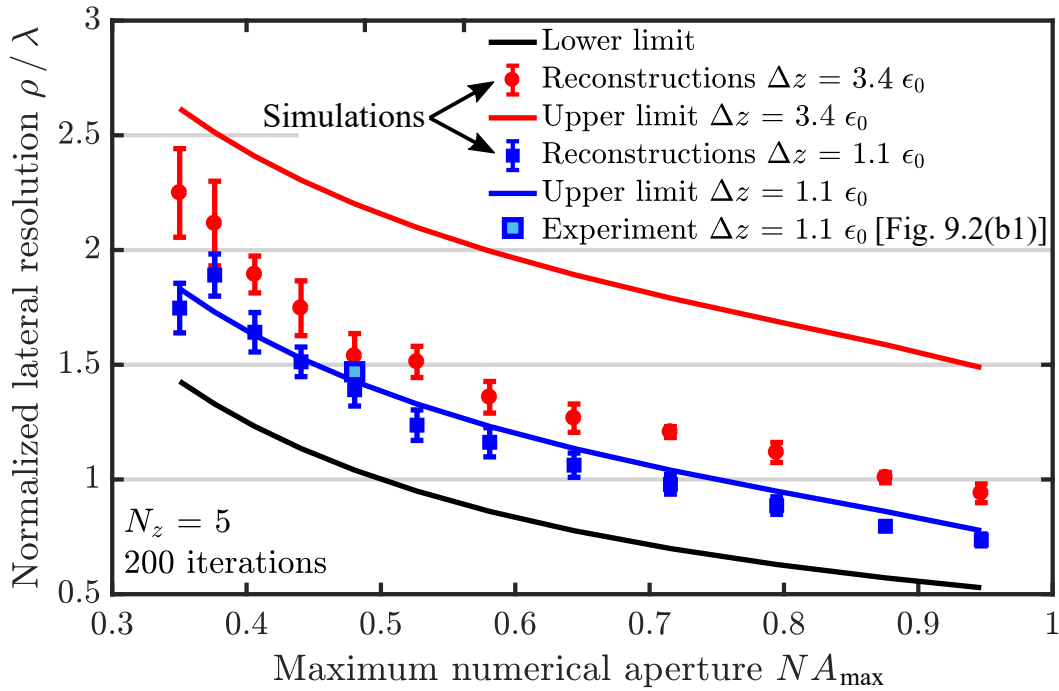


Fig. E.1.: Lateral resolution ρ normalized to the wavelength λ of the SBMIR reconstructions simulated with $N_z = 5$ diffraction patterns at relative distances $\Delta z = 1.1\epsilon_0$ (blue) and $\Delta z = 3.4\epsilon_0$ (red), used in 200 iterations. The estimated normalized resolutions are plotted with markers, while the resolution limits $(2NA_{\max})^{-1}$ (in black) and $(2NA_{\min})^{-1}$ (in the color of the corresponding Δz) are plotted with lines. The light-blue square shows the resolution of the experimental reconstruction in Fig. 9.2(b1). Adapted from [Valzania et al., 2019].

Bibliography

- Al Hadi R., Sherry H., Grzyb J., Zhao Y., Forster W., Keller H. M., Cathelin A., Kaiser A., and Pfeiffer U. R. (2012). “A 1 k-pixel video camera for 0.7–1.1 terahertz imaging applications in 65-nm CMOS”. *IEEE J. Solid-State Circuits* 47.12, pp. 2999–3012 (cit. on p. 32).
- Almoro P., Pedrini G., and Osten W. (2006). “Complete wavefront reconstruction using sequential intensity measurements of a volume speckle field”. *Appl. Opt.* 45.34, pp. 8596–8605 (cit. on p. 109).
- Atkins P. W. and De Paula J. (1998). *Physical chemistry*. Vol. 4. Oxford university press, Oxford UK (cit. on p. 25).
- Belkin M. A. and Capasso F. (2015). “New frontiers in quantum cascade lasers: high performance room temperature terahertz sources”. *Phys. Scr.* 90.11, p. 118002 (cit. on pp. 30, 92).
- Bessou M., Chassagne B., Caumes J.-P., Pradère C., Maire P., Tondusson M., and Abraham E. (2012). “Three-dimensional terahertz computed tomography of human bones”. *Appl. Opt.* 51.28, pp. 6738–6744 (cit. on p. 28).
- Bøggild P., Mackenzie D. M., Whelan P. R., Petersen D. H., Buron J. D., Zurutuza A., Gallop J., Hao L., and Jepsen P. U. (2017). “Mapping the electrical properties of large-area graphene”. *2D Mater.* 4.4, p. 042003 (cit. on p. 28).
- Boppel S., Lisauskas A., Mundt M., Seliuta D., Minkevicius L., Kasalynas I., Valusis G., Mittendorff M., Winnerl S., Krozer V., et al. (2012). “CMOS integrated antenna-coupled field-effect transistors for the detection of radiation from 0.2 to 4.3 THz”. *IEEE Trans. Microw. Theory Techn.* 60.12, pp. 3834–3843 (cit. on p. 91).
- Boreman G. D. (2001). *Modulation transfer function in optical and electro-optical systems*. Vol. 21. SPIE press Bellingham, WA (cit. on p. 58).
- Born M. and Wolf E. (2013). *Principles of optics: electromagnetic theory of propagation, interference and diffraction of light*. Elsevier (cit. on p. 16).
- Brahm A., Wilms A., Dietz R. J., Göbel T., Schell M., Notni G., and Tünnermann A. (2014). “Multichannel terahertz time-domain spectroscopy system at 1030 nm excitation wavelength”. *Opt. Express* 22.11, pp. 12982–12993 (cit. on p. 32).
- Bunk O., Dierolf M., Kynde S., Johnson I., Marti O., and Pfeiffer F. (2008). “Influence of the overlap parameter on the convergence of the ptychographical iterative engine”. *Ultramicroscopy* 108.5, pp. 481–487 (cit. on pp. 18, 55, 62, 63, 82).
- Chatterjee S., Grunwald T., Köhler D., Pierz K., Golde D., Kira M., and Koch S. (2009). “THz measurements of the optical response in a two-dimensional electron gas”. *Physica status solidi c* 6.2, pp. 453–456 (cit. on p. 24).

- Clothier R. H. and Bourne N. (2003). “Effects of THz exposure on human primary keratinocyte differentiation and viability”. *J. Biol. Phys.* 29.2-3, pp. 179–185 (cit. on p. 1).
- Cocker T. L., Jelic V., Gupta M., Molesky S. J., Burgess J. A., De Los Reyes G., Titova L. V., Tsui Y. Y., Freeman M. R., and Hegmann F. A. (2013). “An ultrafast terahertz scanning tunnelling microscope”. *Nat. Photonics* 7.8, p. 620 (cit. on p. 29).
- Cooper K. B., Dengler R. J., Llombart N., Thomas B., Chattopadhyay G., and Siegel P. H. (2011). “THz imaging radar for standoff personnel screening”. *IEEE Trans. THz Sci. Technol.* 1.1, pp. 169–182 (cit. on p. 81).
- Dai J., Liu J., and Zhang X.-C. (2011). “Terahertz wave air photonics: terahertz wave generation and detection with laser-induced gas plasma”. *IEEE J. Sel. Topics Quantum Electron.* 17.1, pp. 183–190 (cit. on p. 33).
- De Ruijter W. and Weiss J. (1993). “Detection limits in quantitative off-axis electron holography”. *Ultramicroscopy* 50.3, pp. 269–283 (cit. on p. 65).
- Dhillon S. S., Vitiello M. S., Linfield E. H., Davies A. G., Hoffmann M. C., Booske J., Paoloni C., Gensch M, Weightman P, Williams G. P., Castro-Camus E, Cumming D. R. S., Simoens F, Escorcia-Carranza I, Grant J, Lucyszyn S., Kuwata-Gonokami M., Konishi K., Koch M., Schmuttenmaer C. A., Cocker T. L., Huber R., Markelz A. G., Taylor Z. D., Wallace V. P., Zeitler J. A., Sibik J., Korter T. M., Ellison B, Rea S, Goldsmith P, Cooper K. B., Appleby R., Pardo D, Huggard P. G., Krozer V, Shams H., Fice M., Renaud C., Seeds A., Stöhr A., Naftaly M., Ridler N., Clarke R., Cunningham J. E., and Johnston M. B. (2017). “The 2017 terahertz science and technology roadmap”. *J. Phys. D: Appl. Phys.* 50.4, p. 043001 (cit. on pp. 23, 31, 33).
- Douglas N. G. (2013). *Millimetre and submillimetre wavelength lasers: a handbook of CW measurements*. Vol. 61. Springer (cit. on pp. 25, 61).
- Edinburgh Instruments Far Infrared / THz lasers*. <https://bit.ly/2TG7fgk>. Accessed: 2019-03-28 (cit. on p. 30).
- Edinburgh Instruments FIRL 100 system*. <https://bit.ly/2uAvH8L>. Accessed: 2019-03-30 (cit. on p. 25).
- Edo T., Batey D., Maiden A., Rau C, Wagner U, Pešić Z., Waigh T., and Rodenburg J. (2013). “Sampling in x-ray ptychography”. *Phys. Rev. A* 87.5, p. 053850 (cit. on p. 17).
- Fan S., Ung B. S., Parrott E. P., Wallace V. P., and Pickwell-MacPherson E. (2017). “In vivo terahertz reflection imaging of human scars during and after the healing process”. *J. Biophotonics* 10.9, pp. 1143–1151 (cit. on pp. 2, 24).
- Fattering C. and Grischkowsky D (1988). “Point source terahertz optics”. *Appl. Phys. Lett.* 53.16, pp. 1480–1482 (cit. on p. 23).
- Ferraro P., Wax A., and Zalevsky Z. (2011). *Coherent Light Microscopy: Imaging and Quantitative Phase Analysis*. Vol. 46. Springer Science & Business Media (cit. on pp. 14, 66).
- Gabor D. (1948). “A new microscopic principle”. *Nature* 161.4098, pp. 777–778 (cit. on p. 13).
- Gallagher J., Blue M., Bean B, and Perkowitz S (1977). “Tabulation of optically pumped far infrared laser lines and applications to atmospheric transmission”. *Infrared Phys.* 17.1, pp. 43–55 (cit. on p. 25).

- Gardner D. F., Tanksalvala M., Shanblatt E. R., Zhang X., Galloway B. R., Porter C. L., Karl Jr R., Bevis C., Adams D. E., Kapteyn H. C., Murnane M. M., and Mancini G. F. (2017). “Subwavelength coherent imaging of periodic samples using a 13.5 nm tabletop high-harmonic light source”. *Nat. Photonics* 11.4, pp. 259–263 (cit. on p. 17).
- Gavrilov N., Knyazev B., Kolobanov E., Kotenkov V., Kubarev V., Kulipanov G., Matveenko A., Medvedev L., Miginsky S., Mironenko L., et al. (2007). “Status of the Novosibirsk high-power terahertz FEL”. *Nucl. Instrum. Methods Phys. Res., Sect. A* 575.1-2, pp. 54–57 (cit. on p. 30).
- Gente R. and Koch M. (2015). “Monitoring leaf water content with THz and sub-THz waves”. *Plant methods* 11.1, p. 15 (cit. on p. 24).
- Godard P., Carbone G., Allain M., Mastropietro F., Chen G., Capello L., Diaz A, Metzger T., Stangl J, and Chamard V. (2011). “Three-dimensional high-resolution quantitative microscopy of extended crystals”. *Nat. Commun.* 2, p. 568 (cit. on p. 17).
- Golay cell*, *Microtech Instruments*. <https://bit.ly/2TCKfyN>. Accessed: 2019-03-28 (cit. on p. 32).
- Goodman J. W. (2005). *Introduction to Fourier optics*. Roberts and Company Publishers (cit. on pp. 7, 11, 19, 63).
- Griffiths D. J. (1962). *Introduction to electrodynamics*. Prentice Hall New Jersey (cit. on p. 12).
- Guerboukha H., Nallappan K., and Skorobogatiy M. (2018). “Toward real-time terahertz imaging”. *Adv. Opt. Photonics* 10.4, pp. 843–938 (cit. on pp. 23, 29, 31, 33).
- Guizar-Sicairos M. (2010). *Methods for coherent lensless imaging and x-ray wavefront measurement*. University of Rochester. Institute of Optics (cit. on p. 2).
- Hack E. and Zolliker P. (2014). “Terahertz holography for imaging amplitude and phase objects”. *Opt. Express* 22.13, pp. 16079–16086 (cit. on p. 59).
- Hack E., Valzania L., Gäumann G., Shalaby M., Hauri C. P., and Zolliker P. (2016). “Comparison of thermal detector arrays for off-axis THz holography and real-time THz imaging”. *Sensors* 16.2, p. 221 (cit. on pp. 5, 32, 37, 40–43).
- Han S.-P., Ko H., Kim N., Lee W.-H., Moon K., Lee I.-M., Lee E. S., Lee D. H., Lee W., Han S.-T., et al. (2014). “Real-time continuous-wave terahertz line scanner based on a compact 1×240 InGaAs Schottky barrier diode array detector”. *Opt. Express* 22.23, pp. 28977–28983 (cit. on p. 32).
- Harmer S. W., Shylo S., Shah M., Bowring N. J., and Owda A. Y. (2016). “On the feasibility of assessing burn wound healing without removal of dressings using radiometric millimetre-wave sensing”. *Progress In Electromagnetics Research* 45, pp. 173–183 (cit. on p. 81).
- Hartwick T., Hodges D., Barker D., and Foote F. (1976). “Far infrared imagery”. *Appl. Opt.* 15.8, pp. 1919–1922 (cit. on p. 23).
- He W, Zhang L, Bowes D, Yin H, Ronald K, Phelps A., and Cross A. (2015). “Generation of broadband terahertz radiation using a backward wave oscillator and pseudospark-sourced electron beam”. *Appl. Phys. Lett.* 107.13, p. 133501 (cit. on p. 30).
- He Y., Ku P. I., Knab J., Chen J., and Markelz A. (2008). “Protein dynamical transition does not require protein structure”. *Phys. Rev. Lett.* 101.17, p. 178103 (cit. on p. 24).

- Hernandez-Cardoso G., Rojas-Landeros S., Alfaro-Gomez M, Hernandez-Serrano A., Salas-Gutierrez I, Lemus-Bedolla E, Castillo-Guzman A., Lopez-Lemus H., and Castro-Camus E (2017). “Terahertz imaging for early screening of diabetic foot syndrome: A proof of concept”. *Sci. Rep.* 7, p. 42124 (cit. on pp. 2, 24).
- Holler M., Guizar-Sicairos M., Tsai E. H., Dinapoli R., Müller E., Bunk O., Raabe J., and Aeppli G. (2017). “High-resolution non-destructive three-dimensional imaging of integrated circuits”. *Nature* 543.7645, pp. 402–406 (cit. on pp. 17, 66).
- Hoppe W (1969). “Diffraction in inhomogeneous primary wave fields. 1. Principle of phase determination from electron diffraction interference”. *Acta Crystallogr., Sect. A: Cryst. Phys., Diffr., Theor. Gen. Crystallogr.* 25, pp. 495–501 (cit. on p. 17).
- Huber A. J., Keilmann F., Wittborn J, Aizpurua J., and Hillenbrand R. (2008). “Terahertz near-field nanoscopy of mobile carriers in single semiconductor nanodevices”. *Nano Lett.* 8.11, pp. 3766–3770 (cit. on p. 29).
- Ishibashi T., Muramoto Y., Yoshimatsu T., and Ito H. (2014). “Unitraveling-carrier photodiodes for terahertz applications”. *IEEE J. Sel. Topics Quantum Electron.* 20.6, pp. 79–88 (cit. on p. 31).
- Jin K. H., Kim Y., Yee D.-S., Lee O. K., and Ye J. C. (2009). “Compressed sensing pulse-echo mode terahertz reflectance tomography”. *Opt. Lett.* 34.24, pp. 3863–3865 (cit. on p. 29).
- Jin Y.-S., Kim G.-J., and Jeon S.-G. (2006). “Terahertz dielectric properties of polymers”. *J. Korean Phys. Soc.* 49.2, pp. 513–517 (cit. on pp. 55, 84).
- Joseph C. S., Patel R., Neel V. A., Giles R. H., and Yaroslavsky A. N. (2014). “Imaging of ex vivo nonmelanoma skin cancers in the optical and terahertz spectral regions optical and terahertz skin cancers imaging”. *J. Biophotonics* 7.5, pp. 295–303 (cit. on p. 2).
- Khalid A., Dunn G., Macpherson R., Thoms S, Macintyre D, Li C, Steer M., Papageorgiou V, Thayne I, Kuball M, et al. (2014). “Terahertz oscillations in an In_{0.53}Ga_{0.47}As submicron planar Gunn diode”. *J. Appl. Phys.* 115.11, p. 114502 (cit. on p. 30).
- Koch-Dandolo C. L., Filtenborg T., Fukunaga K., Skou-Hansen J., and Jepsen P. U. (2015). “Reflection terahertz time-domain imaging for analysis of an 18th century neoclassical easel painting”. *Appl. Opt.* 54.16, pp. 5123–5129 (cit. on p. 28).
- Kreis T. (2006). *Handbook of holographic interferometry: optical and digital methods*. John Wiley & Sons (cit. on pp. 14, 63).
- Kruse P. W. (2001). *Uncooled thermal imaging: arrays, systems, and applications*. Vol. 2003. SPIE press Bellingham, WA (cit. on p. 101).
- Kulkarni R. and Rastogi P. (2014a). “Digital holographic moiré for the direct and simultaneous estimation of strain and slope fields”. *Opt. Express* 22.19, pp. 23192–23201 (cit. on p. 72).
- Kulkarni R. and Rastogi P. (2014b). “Simultaneous measurement of in-plane and out-of-plane displacements using pseudo-Wigner-Hough transform”. *Opt. Express* 22.7, pp. 8703–8711 (cit. on p. 72).
- Kulkarni R. and Rastogi P. (2015a). “Iterative signal separation based multiple phase estimation in digital holographic interferometry”. *Opt. Express* 23.20, pp. 26842–26852 (cit. on p. 72).

- Kulkarni R. and Rastogi P. (2015b). “Three-dimensional displacement measurement from phase signals embedded in a frame in digital holographic interferometry”. *Appl. Opt.* 54.11, pp. 3393–3397 (cit. on p. 72).
- Lee Y.-S. (2009). *Principles of terahertz science and technology*. Vol. 170. Springer Science & Business Media (cit. on pp. 58, 65, 75).
- Leinß S., Kampfrath T., Volkmann K. v., Wolf M., Steiner J. T., Kira M., Koch S. W., Leitenstorfer A., and Huber R. (2008). “Terahertz coherent control of optically dark paraexcitons in Cu₂O”. *Phys. Rev. Lett.* 101.24, p. 246401 (cit. on p. 24).
- Li Z., Yan Q., Qin Y., Kong W., Li G., Zou M., Wang D., You Z., and Zhou X. (2019). “Sparsity-based continuous wave terahertz lens-free on-chip holography with sub-wavelength resolution”. *Opt. Express* 27.2, pp. 702–713 (cit. on p. 50).
- Liu K., Xu J., and Zhang X.-C. (2004). “GaSe crystals for broadband terahertz wave detection”. *Appl. Phys. Lett.* 85.6, pp. 863–865 (cit. on p. 33).
- Locatelli M., Ravaro M., Bartalini S., Consolino L., Vitiello M. S., Cicchi R., Pavone F., and De Natale P. (2015). “Real-time terahertz digital holography with a quantum cascade laser”. *Sci. Rep.* 5, p. 13566 (cit. on p. 28).
- Lucchini M., Brüggemann M., Ludwig A., Gallmann L., Keller U., and Feurer T. (2015). “Ptychographic reconstruction of attosecond pulses”. *Opt. Express* 23.23, pp. 29502–29513 (cit. on p. 17).
- Mackenzie D. M., Whelan P. R., Bøggild P., Jepsen P. U., Redo-Sanchez A., Etayo D., Fabricius N., and Petersen D. H. (2018). “Quality assessment of terahertz time-domain spectroscopy transmission and reflection modes for graphene conductivity mapping”. *Opt. Express* 26.7, pp. 9220–9229 (cit. on p. 28).
- Maiden A., Humphry M., Sarahan M., Kraus B., and Rodenburg J. (2012a). “An annealing algorithm to correct positioning errors in ptychography”. *Ultramicroscopy* 120, pp. 64–72 (cit. on p. 17).
- Maiden A., Johnson D., and Li P. (2017). “Further improvements to the ptychographical iterative engine”. *Optica* 4.7, pp. 736–745 (cit. on pp. 17, 97).
- Maiden A. M. and Rodenburg J. M. (2009). “An improved ptychographical phase retrieval algorithm for diffractive imaging”. *Ultramicroscopy* 109.10, pp. 1256–1262 (cit. on p. 17).
- Maiden A. M., Humphry M. J., and Rodenburg J. (2012b). “Ptychographic transmission microscopy in three dimensions using a multi-slice approach”. *JOSA A* 29.8, pp. 1606–1614 (cit. on p. 17).
- Mastropietro F., Godard P., Burghammer M., Chevillard C., Daillant J., Duboisset J., Allain M., Guenoun P., Nouet J., and Chamard V. (2017). “Revealing crystalline domains in a mollusc shell single-crystalline prism”. *Nat. Mater.* 16.9, p. 946 (cit. on p. 17).
- Matsushima K. (2008). “Formulation of the rotational transformation of wave fields and their application to digital holography”. *Appl. Opt.* 47.19, pp. D110–D116 (cit. on p. 105).
- Matsushima K., Schimmel H., and Wyrowski F. (2003). “Fast calculation method for optical diffraction on tilted planes by use of the angular spectrum of plane waves”. *JOSA A* 20.9, pp. 1755–1762 (cit. on p. 105).

- May R. K., Evans M. J., Zhong S., Warr I., Gladden L. F., Shen Y., and Zeitler J. A. (2011). "Terahertz in-line sensor for direct coating thickness measurement of individual tablets during film coating in real-time". *J. Pharm. Sci.* 100.4, pp. 1535–1544 (cit. on pp. 24, 28).
- Mebius J. E. (2007). "Derivation of the Euler-Rodrigues formula for three-dimensional rotations from the general formula for four-dimensional rotations". *arXiv preprint math/0701759* (cit. on p. 106).
- Minamide H., Hayashi S., Nawata K., Taira T., Shikata J.-i., and Kawase K. (2014). "Kilowatt-peak terahertz-wave generation and sub-femtojoule terahertz-wave pulse detection based on nonlinear optical wavelength-conversion at room temperature". *Journal of Infrared, Millimeter, and Terahertz Waves* 35.1, pp. 25–37 (cit. on p. 31).
- Mittleman D. M. (2018). "Twenty years of terahertz imaging". *Opt. Express* 26.8, pp. 9417–9431 (cit. on p. 23).
- Moruzzi G. (2018). *Microwave, Infrared, and Laser Transitions of Methanol Atlas of Assigned Lines from 0 to 1258 cm⁻¹*. CRC Press (cit. on p. 25).
- Odstrčil M., Holler M., and Guizar-Sicairos M. (2018). "Arbitrary-path fly-scan ptychography". *Opt. Express* 26.10, pp. 12585–12593 (cit. on p. 92).
- Pasumarty S. M., Johnson S. A., Watson S. A., and Adams M. J. (2011). "Friction of the human finger pad: influence of moisture, occlusion and velocity". *Tribol. Lett.* 44.2, p. 117 (cit. on p. 1).
- Pedrini G., Osten W., and Zhang Y. (2005). "Wave-front reconstruction from a sequence of interferograms recorded at different planes". *Opt. Lett.* 30.8, pp. 833–835 (cit. on p. 20).
- Pfeiffer F. (2018). "X-ray ptychography". *Nat. Photonics* 12.1, p. 9 (cit. on p. 17).
- Photoconductive antennas, Toptica Photonics*. <https://bit.ly/2TGswGP>. Accessed: 2019-03-28 (cit. on pp. 31, 32, 92).
- Picart P. (2015). *New techniques in digital holography*. John Wiley & Sons (cit. on p. 14).
- Picart P. and Leval J. (2008). "General theoretical formulation of image formation in digital Fresnel holography". *JOSA A* 25.7, pp. 1744–1761 (cit. on pp. 16, 47, 63).
- Rajshekhar G., Gorthi S. S., and Rastogi P. (2011). "Simultaneous multidimensional deformation measurements using digital holographic moiré". *Appl. Opt.* 50.21, pp. 4189–4197 (cit. on p. 72).
- Rajshekhar G., Gorthi S. S., and Rastogi P. (2012). "Estimation of multiple phases from a single fringe pattern in digital holographic interferometry". *Opt. Express* 20.2, pp. 1281–1291 (cit. on p. 72).
- Rastogi P. K. and Hack E. (2012). *Optical methods for solid mechanics: a full-field approach*. John Wiley & Sons (cit. on pp. 14, 72).
- Razeghi M., Lu Q., Bandyopadhyay N, Zhou W, Heydari D, Bai Y, and Slivken S (2015). "Quantum cascade lasers: from tool to product". *Opt. Express* 23.7, pp. 8462–8475 (cit. on p. 31).
- Redo-Sanchez A., Heshmat B., Aghasi A., Naqvi S., Zhang M., Romberg J., and Raskar R. (2016). "Terahertz time-gated spectral imaging for content extraction through layered structures". *Nat. Commun.* 7, p. 12665 (cit. on p. 28).

- Report of the International Telecommunication Union*. <https://bit.ly/2JTMuhP>. Accessed: 2019-03-31 (cit. on p. 23).
- Rodenburg J. M. (2008). “Ptychography and related diffractive imaging methods”. *Adv. Imaging Electron Phys.* 150, pp. 87–184 (cit. on pp. 2, 17).
- Rodenburg J. M. and Faulkner H. M. (2004). “A phase retrieval algorithm for shifting illumination”. *Appl. Phys. Lett.* 85.20, pp. 4795–4797 (cit. on p. 17).
- Schnars U. and Jueptner W. (2005). *Digital Holography: Digital Hologram Recording, Numerical Reconstruction, and Related Techniques*. Springer (cit. on p. 14).
- Schottky diodes, VDI*. <https://bit.ly/2V3qvWK>. Accessed: 2019-03-28 (cit. on p. 32).
- Seaberg M. D., Zhang B., Gardner D. F., Shanblatt E. R., Murnane M. M., Kapteyn H. C., and Adams D. E. (2014). “Tabletop nanometer extreme ultraviolet imaging in an extended reflection mode using coherent Fresnel ptychography”. *Optica* 1.1, pp. 39–44 (cit. on p. 17).
- Silva J. C. da and Menzel A. (2015). “Elementary signals in ptychography”. *Opt. Express* 23.26, pp. 33812–33821 (cit. on p. 17).
- Spangenberg D., Neethling P., Rohwer E., Brüggmann M. H., and Feurer T. (2015). “Time-domain ptychography”. *Phys. Rev. A* 91.2, p. 021803 (cit. on p. 17).
- Spiricon Pyrocam IIIHR, Ophir Photonics*. <https://bit.ly/2U3b1p3>. Accessed: 2019-03-28 (cit. on p. 32).
- Stockmar M., Cloetens P., Zanette I., Enders B., Dierolf M., Pfeiffer F., and Thibault P. (2013). “Near-field ptychography: phase retrieval for inline holography using a structured illumination”. *Sci. Rep.* 3, p. 1927 (cit. on p. 82).
- Sun Q., Parrott E. P., He Y., and Pickwell-MacPherson E. (2018). “In vivo THz imaging of human skin: Accounting for occlusion effects”. *J. Biophotonics* 11.2, e201700111 (cit. on p. 2).
- Sun Q., Stantchev R. I., Wang J., Parrott E. P., Cottenden A., Chiu T.-W., Ahuja A. T., and Pickwell-MacPherson E. (2019). “In vivo estimation of water diffusivity in occluded human skin using terahertz reflection spectroscopy”. *J. Biophotonics* 12.2, e201800145 (cit. on p. 2).
- Sunderland Z. and Patorski K. (2015). “Three-beam interferogram analysis method for surface flatness testing of glass plates and wedges”. *Photonics Applications in Astronomy, Communications, Industry, and High-Energy Physics Experiments 2015*. Vol. 9662. International Society for Optics and Photonics, p. 96620M (cit. on p. 73).
- Sunderland Z., Patorski K., Wielgus M., and Pokorski K. (2014). “Evaluation of optical parameters of quasi-parallel plates with single-frame interferogram analysis methods and eliminating the influence of camera parasitic fringes”. *19th Polish-Slovak-Czech Optical Conference on Wave and Quantum Aspects of Contemporary Optics*. Vol. 9441. International Society for Optics and Photonics, p. 944111 (cit. on p. 73).
- Taylor Z. D., Singh R. S., Bennett D. B., Tewari P., Kealey C. P., Bajwa N., Culjat M. O., Stojadinovic A., Lee H., Hubschman J.-P., et al. (2011). “THz medical imaging: in vivo hydration sensing”. *IEEE Trans. Terahertz Sci. Technol.* 1.1, pp. 201–219 (cit. on p. 81).
- Terasense imaging products*. <https://bit.ly/2GDqd4A>. Accessed: 2019-02-11 (cit. on p. 12).

- Tesař R. (2018). *Type-II thin film superconductors studied by terahertz radiation*. Univerzita Karlova, Matematicko-fyzikální fakulta (cit. on p. 27).
- Thibault P. and Menzel A. (2013). “Reconstructing state mixtures from diffraction measurements”. *Nature* 494.7435, p. 68 (cit. on pp. 17, 98).
- Thibault P., Dierolf M., Menzel A., Bunk O., David C., and Pfeiffer F. (2008). “High-resolution scanning X-ray diffraction microscopy”. *Science* 321.5887, pp. 379–382 (cit. on p. 17).
- Thibault P., Dierolf M., Bunk O., Menzel A., and Pfeiffer F. (2009). “Probe retrieval in ptychographic coherent diffractive imaging”. *Ultramicroscopy* 109.4, pp. 338–343 (cit. on p. 17).
- Tsai E. H., Usov I., Diaz A., Menzel A., and Guizar-Sicairos M. (2016). “X-ray ptychography with extended depth of field”. *Opt. Express* 24.25, pp. 29089–29108 (cit. on pp. 17, 18, 92).
- Valzania L, Zolliker P, and Hack E (2017a). “Towards the assessment of biomechanical interfaces: Topography of hidden objects obtained with THz holography”. *42nd International Conference on Infrared, Millimeter, and Terahertz Waves (IRMMW-THz)*. IEEE, pp. 1–2 (cit. on p. 5).
- Valzania L., Zolliker P., and Hack E. (2017b). “Topography of hidden objects using THz digital holography with multi-beam interferences”. *Opt. Express* 25.10, pp. 11038–11047 (cit. on pp. 6, 70, 71, 74, 76, 77).
- Valzania L., Hack E., Zolliker P., Brönnimann R., and Feurer T. (2018a). “Resolution limits of terahertz ptychography”. *Unconventional Optical Imaging*. Vol. 10677. International Society for Optics and Photonics, p. 1067720 (cit. on pp. 6, 63, 64, 66, 110).
- Valzania L., Feurer T., Zolliker P., and Hack E. (2018b). “Terahertz ptychography”. *Opt. Lett.* 43.3, pp. 543–546 (cit. on pp. 5, 55–57, 84).
- Valzania L., Zolliker P., and Hack E. (2019). “Coherent reconstruction of a textile and a hidden object with terahertz radiation”. *Optica* 6.4, pp. 518–523 (cit. on pp. 6, 83, 86, 87, 89, 110).
- Vicario C, Jazbinsek M, Ovchinnikov A., Chefonov O., Ashitkov S., Agranat M., and Hauri C. (2015). “High efficiency THz generation in DSTMS, DAST and OH1 pumped by Cr: forsterite laser”. *Opt. Express* 23.4, pp. 4573–4580 (cit. on p. 31).
- Vine D., Williams G., Abbey B, Pfeifer M., Clark J., De Jonge M., McNulty I, Peele A., and Nugent K. (2009). “Ptychographic Fresnel coherent diffractive imaging”. *Phys. Rev. A* 80.6, p. 063823 (cit. on p. 17).
- Wang C., Xu Z., Liu H., Wang Y., Wang J., and Tai R. (2017). “Background noise removal in x-ray ptychography”. *Appl. Opt.* 56.8, pp. 2099–2111 (cit. on p. 56).
- Wang J., Stantchev R. I., Sun Q., Chiu T.-W., Ahuja A. T., and MacPherson E. P. (2018). “THz in vivo measurements: the effects of pressure on skin reflectivity”. *Biomed. Opt. Express* 9.12, pp. 6467–6476 (cit. on p. 2).
- Wilmsink G. J., Rivest B. D., Ibey B. L., Roth C. L., Bernhard J., and Roach W. P. (2010). “Quantitative investigation of the bioeffects associated with terahertz radiation”. *Optical Interactions with Tissues and Cells XXI*. Vol. 7562. International Society for Optics and Photonics, p. 75620L (cit. on p. 1).
- Witteaman W. J. (2013). *The CO₂ laser*. Vol. 53. Springer (cit. on p. 25).

- Wu Q, Hewitt T., and Zhang X.-C. (1996). “Two-dimensional electro-optic imaging of THz beams”. *Appl. Phys. Lett.* 69.8, pp. 1026–1028 (cit. on p. 33).
- Wu T., Dong J., Shao X., and Gigan S. (2017). “Imaging through a thin scattering layer and jointly retrieving the point-spread-function using phase-diversity”. *Opt. Express* 25.22, pp. 27182–27194 (cit. on p. 89).
- Yang X., Zhao X., Yang K., Liu Y., Liu Y., Fu W., and Luo Y. (2016). “Biomedical applications of terahertz spectroscopy and imaging”. *Trends Biotechnol.* 34.10, pp. 810–824 (cit. on p. 2).
- Yao C., Zhou M., and Luo Y. (2014). “A 0.33 THz Schottky diode frequency doubler with 8% efficiency and 5.4 mW output power”. *Proceedings of 2014 3rd Asia-Pacific Conference on Antennas and Propagation*. IEEE, pp. 1399–1401 (cit. on p. 30).
- Yu C., Fan S., Sun Y., and Pickwell-MacPherson E. (2012). “The potential of terahertz imaging for cancer diagnosis: A review of investigations to date”. *Quantitative imaging in medicine and surgery* 2.1, p. 33 (cit. on p. 24).
- Zheng G., Horstmeyer R., and Yang C. (2013). “Wide-field, high-resolution Fourier ptychographic microscopy”. *Nat. Photonics* 7.9, p. 739 (cit. on pp. 17, 92).

Acknowledgments

While I definitely take the blame for every mistake contained in this book, I realize that it wouldn't have been completed without the support of many people.

A special thank goes to Thomas, who allowed me to undertake my PhD at the Institute of Applied Physics of the University of Bern. I truly appreciated his helpful contributions and, in particular, it's thanks to him if *p-t-y-c-h-o-g-r-a-p-h-y* is now a bit more than just a jawbreaker to me.

I can regard Empa as my "scientific cradle", where I shaped myself as a scientist, taking advantage of the endless resources it could offer me. I cannot leave this place without acknowledging some exceptional colleagues.

I would like to express my deepest gratitude to Erwin and Peter for being my "scientific parents", always willing to help me solve my troubles. Peter, thank you for the hours spent in the lab together, especially during my first year, and for sharing several useful Matlab codes. Erwin, thank you for your theoretical insights, and for trying to instill perfectionism in my mind: *"It's 99.9% good, but it's not 100% perfect yet"*. I wouldn't be fair if I didn't thank both of them also for their constant support in every matter, besides the scientific ones, and most importantly for being such authentic persons. I must admit that sometimes they believed in me more than I did.

I should not forget how Rico and the team of apprentices were instrumental in improving the automatization in the lab. Thank you for making my experiments easier. Thank you Rolf, for your help in the preparation of samples, and Fabrizio, for our discussions on the biomedical applications of my project.

Many thanks go to my fellow members of the organizing committee of the Empa PhD Students' Symposium 2017. Emilija, Kristyna, Nadine, Manoj and Mark, it's been a pleasure to work with such motivated people as you!

I had the great honor of sharing an entropic office with a bunch of lovely colleagues. Among the oldest friends, I would like to thank Roman for his wise life advice in Switzerland, which I never followed; Arno, for taking me out to play volleyball and drink beer, especially during the first months of my PhD when I knew almost nobody in Switzerland; and Ivan, for his extremely positive attitude towards life. Thanks to the whole Basel group, who filled our Lab with a lot of vibrating and

stimulating ideas. I really enjoyed, and I'll miss, our relaxing coffee- and tea-breaks after lunch!

A special thank is for the friends I shared my everyday life with. *Zurich Gigios*, I will never forget the laughs and our weekends and holidays spent together. You definitely took part of my soul and made it a *Gigio* one! I wish you the greatest luck for your future.

Looking back at the past, I want to acknowledge all the group of friends who rose in *Via Ronchi 24* in Milan. If I reached this point now, it's also thanks to them. In particular I would like to thank Manu for welcoming me into his flat in Milan whenever I needed during the last four years, and for organizing wonderful trips around the world, which I only had to enjoy. I wish you and Beatrice all the very best.

Il completamento di questa tesi non sarebbe stato possibile senza il supporto incondizionato della mia famiglia: mia mamma, mio papà, mio fratello e mia nonna. Anche se lontani, un'indissolubile interazione a distanza ci lega sempre.

Il più grande Grazie va ad Ale, la mia fonte di felicità. Grazie infinite per il costante incoraggiamento, la pazienza con cui ascolti storie a cui solo io sono interessato, e semplicemente per esserci.

Lorenzo

After all, because we are in Switzerland and money matters (!), the financial support by Empa and the Swiss National Science Foundation, under Project no. 200021_160078/1, is gratefully acknowledged.

Declaration of consent

on the basis of Article 30 of the RSL Phil.-nat. 18

Name/First Name: Valzania Lorenzo

Matriculation Number: 15-126-295

Study program: Physics

Bachelor Master Dissertation

Title of the thesis: Coherent lensless imaging techniques using terahertz radiation

Supervisor: Prof. Dr. Thomas Feurer

I declare herewith that this thesis is my own work and that I have not used any sources other than those stated. I have indicated the adoption of quotations as well as thoughts taken from other authors as such in the thesis. I am aware that the Senate pursuant to Article 28. RSL Phil.-nat. 05 is authorized to revoke the title awarded on the basis of this thesis.

For the purposes of evaluation and verification of compliance with the declaration of originality and the regulations governing plagiarism, I hereby grant the University of Bern the right to process my personal data and to perform the acts of use this requires, in particular, to reproduce the written thesis and to store it permanently in a database, and to use said database, or to make said database available, to enable comparison with future theses submitted by others.

Bern, 17. April 2019

Place/Date



Signature

Curriculum vitae & Research output

Personal information

Surname, name Valzania, Lorenzo
Address Kriesbachstrasse 20
CH-8600 Dübendorf
Phone +41 (0)76 779 26 50
E-mail lorenzo.valzania@empa.ch
Date of birth October 23rd, 1990
Nationality Italian

Education

07/15 - 06/19 PhD Student
Empa, Swiss Federal Laboratories for Materials Science and
Technology, Dübendorf (Switzerland)
and Institute of Applied Physics, University of Bern (Switzer-
land).
09/12 - 04/15 Master of Science in Engineering Physics
Polytechnic University of Milan (Italy).
10/14 - 03/15 Internship at Beamline ID11
ESRF, European Synchrotron Radiation Facility (France).
09/09 - 07/12 Bachelor of Science in Engineering Physics
Polytechnic University of Milan (Italy).
09/04 - 07/09 High School
Liceo Scientifico "A. Righi", Cesena (Italy).

Teaching experiences

07/15 - 06/19 Laboratory Tutor for the Master level course "Optical Methods
in Experimental Mechanics", Mechanical Engineering Program
ETH Zurich (Switzerland).

Academic services

01/17 - 11/17 Member of the Organizing Committee of Empa PhD Students'
Symposium 2017

Empa, Swiss Federal Laboratories for Materials Science and Technology, Dübendorf (Switzerland).

- 04/17 - today Reviewer for the Optical Society of America and Elsevier Journals
Publications in the fields of THz imaging and phase retrieval techniques. Journals (number of reviewed papers): Optics Express (3); Applied Optics (2); Photonics Research (1); Optics and Lasers in Engineering (1).
- 06/18 - 06/19 Student Member of the International Society for Optics and Photonics (SPIE).

Awards and highlights

- 2018 Best Student Paper Award at the Unconventional Optical Imaging Conference of the 2018 SPIE Photonics Europe Meeting
L. Valzania, E. Hack, P. Zolliker, R. Brönnimann, and T. Feurer, “Resolution limits of terahertz ptychography”, (talk) in Proceedings of SPIE 10677, Unconventional Optical Imaging, 1067720.
- 2018 Publication selected as a Spotlight on Optics of the Optical Society of America
L. Valzania, T. Feurer, P. Zolliker, and E. Hack, “Terahertz ptychography”, Optics Letters 43(3), 543-546.
- 2016 1st prize for Outstanding Oral Presentation at Empa PhD Students’ Symposium 2016
L. Valzania, P. Zolliker, and E. Hack, “Unraveling hidden biomechanical interfaces with terahertz radiation”.

Peer-reviewed publications

- 2019 **L. Valzania**, P. Zolliker, and E. Hack, “Coherent reconstruction of a textile and a hidden object with terahertz radiation”, Optica 6(4), 518-523.
- 2018 **L. Valzania**, T. Feurer, P. Zolliker, and E. Hack, “Terahertz ptychography”, Optics Letters 43(3), 543-546.
- 2017 P. Zolliker, M. Rüggeberg, **L. Valzania**, and E. Hack, “Extracting wood properties from structured THz spectra: birefringence and water content”, IEEE Transactions on Terahertz Science and Technology 7(6), 722-731.

- 2017 **L. Valzania**, P. Zolliker, and E. Hack, “Topography of hidden objects using THz digital holography with multi-beam interferences”, *Optics Express* 25(10), 11038-11047.
- 2016 E. Hack, **L. Valzania**, G. Gäumann, M. Shalaby, C. P. Hauri, and P. Zolliker, “Comparison of thermal detector arrays for off-axis THz holography and real-time THz imaging”, *Sensors* 16(2), 221.
- 2016 N. Vigano, L. Nervo, **L. Valzania**, G. Singh, M. Preuss, K. J. Batenburg, and W. Ludwig, “A feasibility study of full-field X-ray orientation microscopy at the onset of deformation twinning”, *Journal of Applied Crystallography* 49(2), 544-555.

Conference contributions

- 2019 **L. Valzania**, P. Zolliker, and E. Hack, “Coherent terahertz imaging of a textile and a hidden object”, to be presented at next OSA Digital Holography and 3-D Imaging Topical Meeting.
- 2019 B. J. Kang, G. Gäumann, N. Numan, Z. Ollmann, Y. Waeber, S. Bagiante, **L. Valzania**, P. Zolliker, N. Émond, M. Chaker, E. Hack, M. Maaza, and T. Feurer, “THz-induced insulator-to-metal transition in stacked VO₂ nano-slits”, to be presented at next 44th International Conference on Infrared, Millimeter and Terahertz waves IRMMW-THz 2019.
- 2018 **L. Valzania**, E. Hack, P. Zolliker, R. Brönnimann, and T. Feurer, “Resolution limits of terahertz ptychography”, (talk) in Proceedings of SPIE 10677, Unconventional Optical Imaging, 1067720.
- 2018 E. Hack, **L. Valzania**, P. Zolliker, and T. Feurer, “THz ptychography and digital holography: a comparison”, (talk) in PhotoMechanics.
- 2017 E. Hack, **L. Valzania**, and P. Zolliker, “Topography of hidden objects revealed using THz digital holography”, (talk) in BSSM 12th International Conference on Advances in Experimental Mechanics.
- 2017 **L. Valzania**, P. Zolliker, and E. Hack, “Towards the assessment of biomechanical interfaces: Topography of hidden objects obtained with THz holography”, (talk) in 42nd International Conference on Infrared, Millimeter and Terahertz waves IRMMW-THz 2017.

- 2016 P. Zolliker, **L. Valzania**, and E. Hack, “THz Holography with micro-bolometers”, (talk) in EMN Meeting on Terahertz Energy Materials Nanotechnology, pp. 78-79.
- 2016 **L. Valzania**, P. Zolliker, and E. Hack, “Topography of a fingertip through combined THz digital holography and optical fringe projection”, (talk) in International Conference on Processes in Combined Digital Optical and Imaging Methods applied to Mechanical Engineering.

Seminars and contributions to websites and technical newspapers

- 2019 E. Hack, **L. Valzania**, and P. Zolliker, “Durchblick mit Holographie: Bildgebende Verfahren mit Terahertzstrahlen”, Physik in unserer Zeit 49(6), 290-295.
- 2018 **L. Valzania**, P. Zolliker, and E. Hack, “Imaging through textiles with terahertz radiation”, oral presentation at Empa PhD Students’ Symposium 2018.
- 2018 **L. Valzania**, E. Hack, P. Zolliker, R. Brönnimann, and T. Feurer, “Terahertz ptychography”, oral presentation at Empa Topical Day on Imaging and Image Analysis X.
- 2017 E. Hack, **L. Valzania**, and P. Zolliker, “Terahertz topography of hidden objects”, oral presentation at Empa Topical Day on Imaging and Image Analysis IX.
- 2016 E. Hack, **L. Valzania**, and P. Zolliker, “Terahertz imaging of biomechanical interfaces”, SPIE Newsroom.
- 2016 **L. Valzania**, P. Zolliker, and E. Hack, “Unraveling hidden biomechanical interfaces with terahertz radiation”, oral presentation at Empa PhD Students’ Symposium 2016.
- 2015 **L. Valzania**, P. Zolliker, and E. Hack, “THz holography of a fingertip during mechanical contact with THz transparent materials”, oral presentation at Empa PhD Students’ Symposium 2015.